Ultrasonic Detection and Expulsion of Kidney Stones

Wei Lu

A dissertation
submitted in partial fulfillment of the
requirements for the degree of

Doctor of Philosophy

University of Washington

2012

Reading Committee:
Lawrence A. Crum, Co-Chair
Michael R. Bailey, Co-Chair
Oleg A. Sapozhnikov

Program Authorized to Offer Degree:
Department of Bioengineering

University of Washington

Abstract

Ultrasonic Detection and Expulsion of Kidney Stones

Wei Lu

Co-chairs of the Supervisor Committee:
Dr. Lawrence A. Crum
Dr. Michael R. Bailey
Department of Bioengineering

Kidney stone disease afflicts 10% of the U.S. population and severely affects the life quality of patients. There are still many problems with the diagnosis and treatment of renal stones. In diagnosis, X-ray computerized tomography (CT) is the most commonly used technology as it allows urologists/radiologists to locate the stone(s) with high sensitivity. Unfortunately, more and more evidence has been collected that shows that the radiation exposure to patients during CT scans may increase the risk of developing cancer. In kidney stone treatments, extracorporeal shock-wave lithotripsy (ESWL), which breaks the stone with shock waves, is widely used as it is non-invasive and allows the fragments to pass naturally; however, small stone fragments located in the lower pole of the kidney often remain in the kidney, which can cause stones to recur in 50% of ESWL patients within 5 years. Therefore, new technologies that allow for better kidney stone detection and treatment are needed.

The twinkling artifact (TA) has been shown to highlight kidney stones during color Doppler ultrasound imaging with high sensitivity for stone detection; however, the instability of the TA has prevented it from being adopted clinically. In this dissertation, the mechanism of the TA was investigated based on raw radio-frequency (RF) data collected from *in vitro* human kidney stones using the MATLAB^{TM} Programmable Verasonics$^{®}$ ultrasound engine. Algorithms, such as

beamforming, quadrature demodulation, Doppler processing, *etc.*, were developed to minimize ambiguity in the signal processing. Synthesized RF signals were sent directly into the ultrasound machine in order to separate the acoustic effects from the signal processing effects. It was determined the variability that results in the TA arises from acoustical interactions with the stone. Next, the acoustical effects (*i.e.*, crevice microbubbles, stone ringing, etc.) of the TA were investigated by applying high static pressure (up to 8.5 MPa) on old and fresh human stones where it was determined that microbubbles trapped in crevices on the surface of the stone plays an important role in producing the TA. Modeling simulations were applied to eliminate stone ringing as a possible contributor to the TA. These results have led to the development of new imaging algorithms for better stone detection. A quantitative comparison between the new twinkling image algorithms and the classic color Doppler TA shows that the new imaging techniques are more stable and accurate.

Besides improving kidney stone detection, an ultrasound-guided system that is capable of expelling small kidney stones or stone fragments from the kidney has been developed. This device uses acoustic radiation forces and associated acoustic streaming to 'push' stones out of the lower pole of the kidney and has been tested successfully in a stone phantom and in many *in vivo* porcine experiments. Preliminary histological results suggest that the device is safe and that there is no visible thermal or mechanical damage to the kidney.

  The primary result of this dissertation is insight into the mechanism of the TA, which allowed for the development of new ultrasonic stone-specialized imaging algorithms. In addition, a novel ultrasound technology was developed for expelling small stones or stone fragments from the kidney. Besides furthering science, the results from this dissertation should directly influence patients as it provides improved stone detection and treatment technologies with ultrasound, a non-ionizing alternative to traditional diagnosis regimes, that holds great promise to be adopted clinically.

TABLE OF CONTENTS

Page

LIST OF FIGURES

ACKNOWLEDGEMENTS

I wish to thank all those who participated in this work and provided help and support to me during my PhD studies.

I would like to thank my supervisory committee members: Dean Matthew O'Donnell, Dr. Lawrence Crum, Dr. Michael Bailey, Dr. Oleg Sapozhnikov, Dr. Jonathan Harper, and Dr. Randy LeVeque for their time and support. In particular, thanks to Dr. Crum for his unwavering support and always being available for conversation with students; thanks to Dr. Bailey, who is an enthusiastic advisor and wonderful person to work with and who arranged this wonderfulwonderful project for me; thanks to Dr. Sapozhnikov, who is highly knowledgeable, for bringing the twinkling idea to the group and for helping with experiments, modeling, and data analyses. Thanks to Dr. Harper for his suggestions and help with the project from the clinical perspective. Thanks to Dr. Kaczkowski for teaching me the Verasonics system and for his suggestions on the development of processing algorithms. Thanks to the students and staff at the Center for Industrial and Medical Ultrasound (CIMU). Thanks to all the friends that I have met in Seattle. Lastly, thanks to my family and my wife, Jing, for their unconditional support throughout the years that I have been in school. Without you, I could not have made it.

Chapter 1

INTRODUCTION

1.1 Motivation

Kidney stone disease afflicts 10% of the U.S. population and this number is rising. [1-2] The prevalence of kidney stones varies depending on race, sex, age and geographic location; however, stone formers can be of any age, and can develop multiple stones at a time. More than 3 million diagnoses and treatments are made annually and the total cost was calculated to be over $2B in 2000, which was 50% higher than the cost in 1994. [1] Initial success rates range from ~70% to greater than 90% depending on the type of treatment performed. However, stones will recur in half the patients within 5 years.

The most commonly used technology for kidney stone diagnosis is X-ray computerized tomography (CT). CT is expensive and exposes the patient to ionizing radiation that may increase patients' risk of developing cancer later in life. [3] The U.S. Food and Drug Administration (FDA) has even begun to reduce the X-ray exposure. Ultrasound is a non-radiation, non-invasive and low-cost imaging technique that has been used to assist in diagnosing patients with kidney stones. However, compared to the gold standard of CT, ultrasound provides a relatively low sensitivity (as low as 30%) for stone detection. [4-5] Recently, a Doppler ultrasound artifact called the 'Twinkling Artifact (TA)' [6] has been reported to improve the sensitivity of ultrasound for stone detection [7-12]. The TA is described as rapid color alerting on hard objects such as kidney stones; however, due to the inconstancy of the TA, it has not been adopted clinically for the diagnosis of kidney stones. As the underlying mechanism of the TA has not been elucidated, it is difficult to make the TA a consistent effect for clinical use.

Extracorporeal shock-wave lithotripsy (ESWL) is the most common treatment for kidney stones. It uses focused shock waves to break the stones into pieces that

can pass naturally. Small stone fragments in the renal pelvis have a good chance of passing naturally, but fragments located in the lower calyces are more likely to remain. The residual stone fragments act as nuclei for future stones [13], which causes high retreatment and low stone-free rates for lower pole stones. [14-15] Follow-up surgical management of stones is complex and individualized but depends significantly on the resources available at the clinical, causes additional discomfort, and exposes the patient to multiple X-rays. If stones or stone fragments could be moved out ofthe lower pole to the renal pelvis for treatment or to passnaturally, it would dramatically reduce the number of retreatments a patient would receive. Some researchers have approached this residual stone fragments problem by trying to prescreen anatomies where lower pole fragments will not pass. [15-19] Others have tried to move the stone via ureteroscopy [20-21], patient inversion [22-23], percussion [24], or citrate [25-26]. Unfortunately, these approaches have had mixed results and are not commonly used.

Therefore, new technologies that can provide accurate stone detection with non-ionizing-radiation and can reduce the stone recurrence rate are badly needed.

1.2 Background:

1.2.1 Kidney Stone Detection

Current Technologies and Problems

Unenhanced CT is the gold standard in stone diagnosis. [4-5, 27-29] However, more and more evidence shows that the ionizing-radiation that patients are exposed to during a CT scan may increase their risk of developing cancer later in life. The 1st International Consultation on Stone Disease (Paris 2003) [30] states the area for greatest gain in stone localization is "reduction of the radiation exposure associated with spiral CT". The U.S. Food and Drug Administration (FDA) has also pointed out the need for reducing the X-ray exposure. [3] Plain X-ray is the most common imaging technique used to detect stones as it is simple to perform

and exposes the patient to less ionizing-radiation than CT. However, it has limited value for detecting radiolucent stones (as shown in figure 1.1) and limited ability to detectsmall stones. [18] Furthermore, due to the poor stone contrast, there may be intra- and inter-observer variation in the interpretation of images. [32] An alternative technology that provides accurate stone detection and reduces the exposure toionizing-radiation is needed.

Ultrasound, as a non-ionizing-radiation, non-invasive, and low-cost technology, fits the need for kidney stone detection. Kidney stones are identified with a bright region followed by distal acoustic shadowing on the image. Although the distal acoustic shadowing has long been used as an assistant to identify kidney stones [33-34], the sensitivity of using ultrasound for stone detection is as low as 30% when compared to CT [4-5].
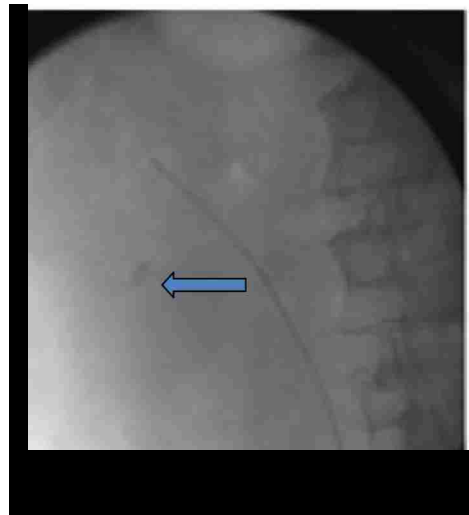
The Twinkling Artifact (TA)

In 1996, a color Doppler artifact, called the "twinkling artifact", which alights on parenchymal calcifications, was described by Rahmouni *et al.* in detail [6]. The effect was described as a rapid changing mixture of red and blue behind presumed calcification, as shown in figure 1.2. Recent clinical studies [7-12] have shown that the TA can dramatically enhance the sensitivity (to over 80%) for stone detection, which indicates that the TA has a huge potential for improving kidney stone detection with ultrasound.
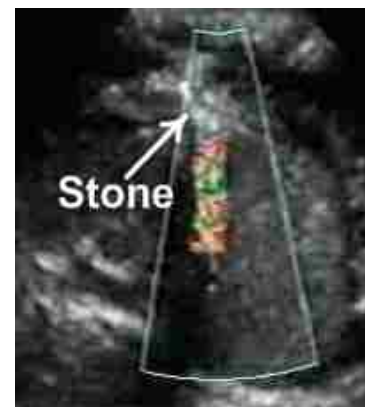
However, the mechanism of the TA is still unknown. Some studies have shed some light towards developing an understanding of the mechanism of the TA on

3

kidney stones. So far, there are two main hypotheses on the origin of the TA. The variability that is responsible for the appearance of the TA comes from 1) the acoustic field or 2) the imperfection of the machine.

Some investigators believe that the variability responding to the presence of the TA comes from the acoustic field. Rahmouni et al. [6] explained that the TA is a result of random scattering of the ultrasound beam at multiple reflectors associated with the rough interface typical for the stones. On the other hand, in an in vitro experiment using turkey breast and gelatin embedded with small inclusions of calcium carbonate, Weinstein et al. [35] concluded that twinkling was due to acoustic resonances. Chelfouh et al. [36] considered the intensity/character of the TA might depend on the morphologic and biochemical content of stones. They found that the artifact is always present for calcium phosphate and dehydrated calcium oxalate stones, but absent for urate stones and calcifications that contain more than 93% monohydrate calcium oxalate.

Other investigators support the idea that the appearance of the TA is determined by the ultrasound machine or machine settings. For example, Aytac et al. [7] published results comparing two ultrasound scanners (analog and digital) that were used to image kidney stones. They discovered that the presence and intensity of the TA depends on the scanner type; the digital scanner showed twinkling on 96% of stones while the analog scanner only showed twinkling on 39% of stones. On the contrary, Lelyuk et al. [37] concluded that the effect does not depend on the scanner type; rather it depends on the signal processing method and the type of scan-head. In the study by Lelyuk et al., researchers found that for various objects (urinary concrement of composed structures, metal bolts, pieces of chalk, and quail eggs) all of the scanners and all of the scan-heads demonstrated more or less a pronounced twinkling effect. They doubted that the artifact depended on the Doppler imaging window, frequency filtration, time-averaging or scanning depth. In addition, Lelyuk et al. concluded that the twinkling intensity most strongly depends on transmitted powers, the diapason of

the Doppler scale and receiving gain, but that the presence of the TA does not depend on those parameters. Rubaltelli L. *et al.* [38] did not agree with those conclusions; they thought the appearance of the TA is due to incorrect scanner settings. Recently, Kamaya *et al.* [39] hypothesized that the cause for the artifact is narrow-band internal noise due to "phase jitter" and the irregular stone surface is only secondary and serves for broadening the spectrum. However, they also concluded "our experiments were limited by the inability to control all machine settings separately", which leaves many steps in their outline unexplained. The underlying mechanism of the TA is still under debate, although the TA has been known for over 15 years.

A better understanding into the origin of the TA is badly needed, not only to explain this unique phenomenon, but also to allow us to improve the TA for better kidney stone detection. The current imaging method for creating the TA is the color flow Doppler imaging algorithm, which is generally used to image blood flow rather than kidney stones. The TA can be easily confused with color pixels resulting from blood flow or over-gained noise. In addition, most current studies on the TA are focused on the images and the Doppler spectrum that are provided by ultrasound machines, which may vary between machines depending on the imaging processing methods employed. Furthermore, most machines only provide investigators limited control of the machine settings, which makes it arduous to distinguish the function of each imaging parameter or setting. The knowledge gained through a better understanding of the mechanism and signal properties of the TA can improve the technology and make it stone-specialized. Meanwhile,a general protocol for stone imaging using the TA can be established to make it easier for clinical adoption.

1.2.2 Kidney Stone Treatment

Current Technologies and Problems

Currently, extracorporeal shock wave lithotripsy (ESWL) is the most common treatment used for kidney stones. Shock waves generated outside the body are focused to a fixed location. The patient, usually under anesthesia or conscious sedation, is positioned with the stone in the focal zone. The stone free rate for lithotripsy is 40-90%, meaning residual fragments remain in around 50% of patients. Residual fragments act as nuclei for future stones, [13] and the recurrence rate following lithotripsy is 50% within 5 years. [40] Additional treatments will then be applied for recurrent stones or problematic residual stones. Figure 1.3 shows the structure of the collecting system for a human kidney. Residual fragments have particular difficulties in passing from the lower pole, making retreatment rates for lower pole stones high and stone free-rates low. [14] As a result, prominent urologists recommend against SWL as a treatment option for lower pole stones larger than 1 cm. [14, 41], Despite the evolution of technology-driven surgical approaches, the success in surgical management of lower pole stones is principally dependent on two processes: stone fragmentation and residual fragment clearance. [42] The clinical need for residual fragment clearance is highlighted. [43]
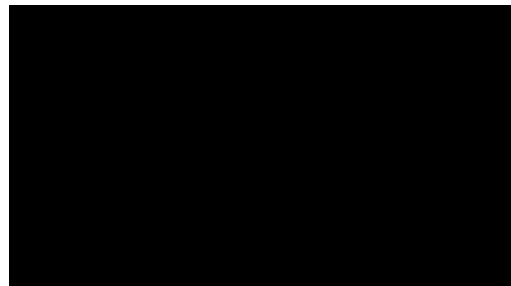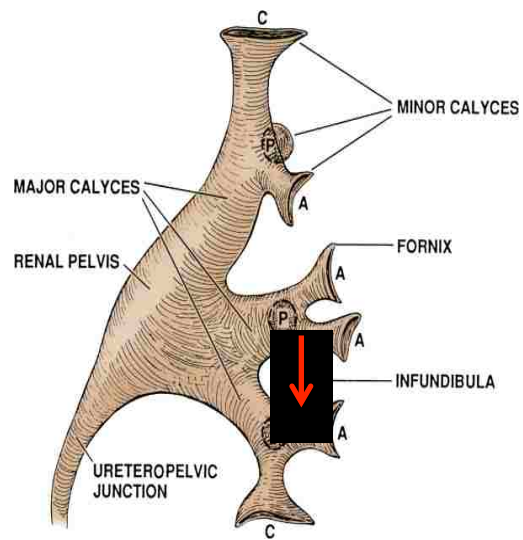
Stone or Stone Fragment Clearance

Several researchers have approached this residual stone fragments problem by trying to prescreen anatomies where lower pole fragments cannot pass. [15-19]

Although some approaches have been tried to move the stone, such as using ureteroscopy [20-21], inversion of the patient [22-23], percussion [24], or citrate [25-26], these approaches have had mixed results and are not commonly used.

Another method that has been tried is to use repeated lithotripsies to "stir up" the residual fragments following lower pole lithotripsy. [44-45] Results indicated that stones are readily seen to jump in a suspending medium when impacted by shock waves. However, the mechanism of 'stirring' is not explained. The apparent reason for the motion of stone/stone fragments is due to the radiation force and the associated streaming that is generated by ultrasound. Acoustic radiation force is commonly used to move objects such as bubbles [46], drops [47] and cells [48]. Streaming associated with radiation force has been used to diagnose fluid-filled cysts [49] and bleeding from blood clots [50]. If stones or stone fragments could be moved using acoustic radiation force and associated streaming from the lower pole to the renal pelvis for treatment, the post-surgical stone-free rates will be improved and the number of patients having to undergo a second lithotripsy – a second exposure to the maximum dose – would be reduced.

1.3 Scope:

The principal objectives of this work are to understand the mechanism of the TA, study the signal properties of the TA, and develop ultrasound-based algorithms for better kidney stone detection. Specifically, the mechanism of the TA was investigated and several new stone-specialized imaging algorithms were developed based on the TA signal properties (Chapters 2 and 3). Also, a new stone expulsion technology that can reposition kidney stones or stone fragments by using ultrasound is developed and tested successfully in a porcine model (Chapter 4).

In Chapter 2, the mechanism of the TA was investigated from the raw radio-frequency (RF) per-channel data collected from *in vitro* human kidney stones

using the MATLAB^{TM} Programmable Verasonics$^{®}$ ultrasound engine (VUE). The algorithms, including beamforming, quadrature demodulation, Doppler processing *etc*., were developed to minimize the processing ambiguity. Synthesized RF signals were sent directly into the ultrasound system in order to separate acoustic and signal processing effects. Several hypotheses were tested under high static pressure conditions (up to 8.5 MPa) or simulated by modeling. At the end of the study, fresh human kidney stones that had limited air contact were tested to validate the conclusion driven from the old stone experiments. These results suggest that microbubbles in the crevices on the stone are the mechanism of the TA.

In Chapter 3, the twinkling signals were analyzed from raw RF per-channel data collected from human kidney stones in *in vitro* stone phantoms and *in vivo* porcine experiments. The effects of the acoustic and machine parameters, (including the pulse length, the Doppler ensemble length, the pulse repetition frequency (PRF), Doppler transmitting power, time gain compensation (TGC), etc.), on the twinkling signals were compared and discussed. Based on the twinkling signal studies and the basic signal path of the Color Flow Doppler ultrasound imaging system, several new imaging technologies for better kidney stone detection were developed by exploiting new imaging processing algorithms, changing the electronics and recognizing the physical differences between stones and the surrounding tissues. The new imaging methods showed higher stability and sensitivity, as compared to the classic TA algorithm.

In Chapter 4, an ultrasound-guided system which moves the stone and stone fragments within the collecting system of the kidney by acoustic radiation forces and associated acoustic streaming was introduced. A prototype device has been engineered from the VUE. Preliminary results on animal models show that we can reposition stones from the lower calyx to the ureteropelvic juncture (UPJ) in less than 5 minutes. In other words, the treatment procedure in humans could be easily completed during an office visit.

In Chapter 5, the results are summarized and future directions for this work are presented.

Investigation into the Mechanism of the Twinkling Artifact

In this chapter, the mechanism of the twinkling artifact (TA) will be described based on raw radio-frequency (RF) data collected from *in vitro* human kidney stones using the Verasonics® ultrasound engine (VUE). In summary, the analysis began by minimizing the signal processing ambiguity of the TA by using self-developed algorithms. The main hypotheses are that the TA is due to either machine effects (*i.e.*, phase jitter) or acoustical effects (*i.e.*, microbubbles, cracks or strong ringing). The machine effects of the TA were separated from the acoustical effects by sending synthesized RF signals directly into the VUE where it was determined that the machine did not cause the TA. The acoustical effects of the TA was investigated by applying high static pressure (up to 8.5 MPa) to the human stones and acrylic spheres with rough surfaces where it suggested that the microbubbles trapped in the crevices play an important role in causing the TA. Stone ringing was excluded from the hypothesis by applying a modeling simulation. Fresh human kidney stones that had limited air contact were tested under overpressure where the crevice bubble hypothesis was confirmed on *ex vivo* stones. The results suggested that the crevice bubbles play an important role in causing the TA.

2.1 Introduction

Due to the rising concerns over the amount of ionizing radiation received by patients from X-rays, particularly CT, and the inherent risk of cancer from exposure to ionizing radiation, an alternative diagnostic is needed for stone detection. Unfortunately, ultrasound, a non-ionizing radiation alternative to detect stones has low sensitivity in stone detection. An alternative diagnostic criterion

with high sensitivity in stone detection is needed to reduce the number of CT scans and x-rays.

It has been known for over 15 years that the TA, which appears as color altering on hard objects in color Doppler ultrasound can detect kidney stones. Recent studies [6-10, 51-52] have reported that the TA, as a Doppler ultrasound technique with high-accuracy and non-ionizing-radiation, has great potential for improving stone detection; however, the mechanism of the TA is still under debate as the artifact is inconsistent. Thus, the technique has never been adopted clinically.

Figure 2.1 shows the standard signal path of color flow Doppler ultrasound imaging (more details are in Chapter 3). Basically, the machine stimulates the transducer to send out Doppler ensembles. Each Doppler ensemble contains multiple pulses, the number of which ranges from 3 to 32 [53]. After interaction with the object, the echo Doppler ensemble is received by the transducer and goes through the electronics where the signals are amplified and digitized. The digitized Doppler ensemble then goes through the beam-former (realized in software in VUE) and the beamformed Doppler ensemble gets signal- and Doppler-processed by quadrature demodulation, wall-filtration, Doppler power and mean frequency estimation, and so on.

Construction of the color image depends on a variety of information, mostly notably the Doppler power (Appendix B) returning from the corresponding sample volume. The strength of the Doppler power will determine whether the Doppler color information is displayed, with the peak value determining where the color is most likely to be shown. In other words, Doppler power is a good indicator of variability within the Doppler ensemble.

Some investigators believe that variability in the acoustic field (*i.e.*, acoustic scattering from an irregular surface [7], acoustic resonance [35] and morphologic and biochemical content of stones [36]) causes the TA while others believe that the machine or machine settings (i.e. the scanner types [7], parameters used in imaging processing [38], or incorrect machine settings [37]) causes the TA. More recently, Kamaya *et al.* [39] claimed that the internal noise due to "phase jitter" is the dominant reason for the TA, and that the irregular surface of the target is secondary and simply serves to broaden the spectrum. For most of these studies, the conclusions were drawn based on the color Doppler images or the Doppler spectrum provided by commercial ultrasound machines. The commercial ultrasound machines are black boxes in that it is very difficult to separate the acoustical effects from the effects of the machine. In addition, clinical ultrasound machines rarely provide costumers access to the raw RF data that may provide more insight into the TA.

The Verasonics Ultrasound Engine (VUE) gives us full access to the raw per-channel RF data immediately following the Analog-to-Digital converter (ADC). The advantage of investigating the TA from the RF data is that the per-channel RF data is the most original data after digitizing, which allows us to separate signal processing effects from other possible effects. This advantage could enable us to study the mechanism of the TA without interference from other machine settings such as: various thresholds, color written priority, gains, etc. Since the Doppler processing and image processing algorithms differ between machines, being able to access raw RF data will allow us to eliminate the influence of processing algorithms such as beamforming, demodulation, averaging, *etc.*, by applying self-developed Doppler processing algorithms. Last but not least, raw RF data could provide fundamental information on the TA as compared to other Doppler images.

In this project, we mainly focus on the raw RF data that corresponds to the TA. The main goal of this study is to better understand the mechanism of the TA. The

dominant reason for the occurrence of the TA was investigated by estimating whether the variability within the Doppler ensemble is introduced from the acoustic field or the machine; in addition, a high static pressure study was performed for further insight into the possible mechanisms, *i.e.*, microbubbles. Several signal and Doppler processing algorithms, which are described in detail in Appendix B and C, have been developed based on existing literature [54-64] to reduce the ambiguity that arises when using pre-existing processing algorithms.

2.2 Materials and Methods

2.2.1 Tools

The main tool used in this study was a new, commercial-off-the-shelf (COTS) ultrasound machine – Verasonics Ultrasound Engine (VUE, Verasonics, Redmond, WA.), which is shown in figure 2.2. VUE is an FDA-approved ultrasound imager. As mentioned before, VUE provides researchers access to the raw per-channel RF data immediately following the analog-to-digital converter (ADC). A clinical probe (ATL/Philips HDI L7-4, f_c = 5MHz) was used for all experiments.

2.2.2 Materials and Phantoms

Human kidney stones (5-10mm in length ; 3-5mm in width) that consist of more than 90% calcium oxalate monohydrate (COM) were used for all experiments. Stones were immersed in the degassed water for over 48 hours prior to all experiments.

Several *in vitro* phantoms were made for experiments.

1) The Gel Phantom

The gel phantom is long-lasting and allows us to repeat the experiment with many different settings. The tissue-mimicking phantom used for these experiments was a polyacrylamide hydrogel. To prepare the tissue phantoms, the liquid mixture was first degassed for at least one hour in a desiccant chamber and then poured into a plastic container, where a polymerization agent was added. When it was set, human kidney stones were placed on the concretionary gel, and another degassed liquid mixture was poured in with a polymerization agent. The end result was a gel with stones suspended in the middle of the container. The attenuation coefficient, sound speed and impedance were 0.08 dB/cm at 1 MHz, 1546 m/s and 1.58 Mrayl, respectively. [65] The gel phantom is shown in figure 2.3.

2) *Ex vivo* porcine kidney phantom

Porcine kidneys were purchased from the slaughterhouse. To prepare the phantom, the kidney first was submerged into water and degassed for over an hour in a desiccant chamber. Then, the kidney was sliced lengthwise using a scalpel to expose the collecting system. Human kidney stones were placed in the collecting system of the kidney and the kidney was suspended in a plastic container using polyacrylamide gel.

2.3 Experimental Setup and Results:

All experimental setups were designed with the idea of being able to: 1) determine whether the acoustic or machine variability affects the TA and 2) test the sub-hypotheses of the TA to better understand the mechanism;

2.3.1 Acoustics or Machine?

The difficulty of separating the influence of the acoustics and the machine arises because the effect has always been combined in clinical ultrasound machines since there was no access to the raw data; both the acoustics and the machine could introduce variability into the Doppler ensemble. So, if one of the parts (the acoustics or the machine) could be held stable, the two sources of variability could be isolated. With the VUE, we are capable of accessing raw RF data immediately following the digitizer, narrowing the machine uncertainty to the electronics. If there is no variability within the Doppler ensemble after modifying the acoustics, the conclusion could be that the imperfection of the machine is not the dominant reason for the TA or vice versa. A sketch of the experimental design is shown in figure 2.4. One possible reason for the variability introduced by machine is its internal 'phase jitter', which is caused by an instability in the internal clock of the machine. This effect is hard to eliminate. Therefore, when we did the experiment, we kept the machine settings the same but replaced the acoustic field by a stable simulated source.
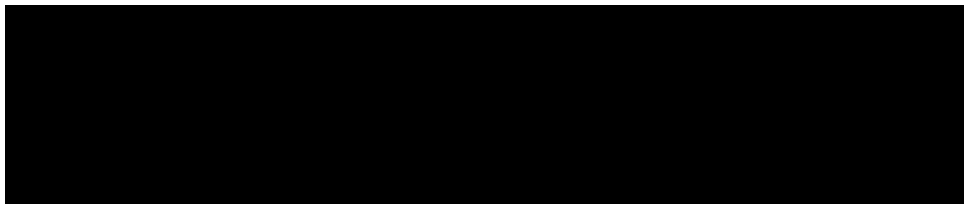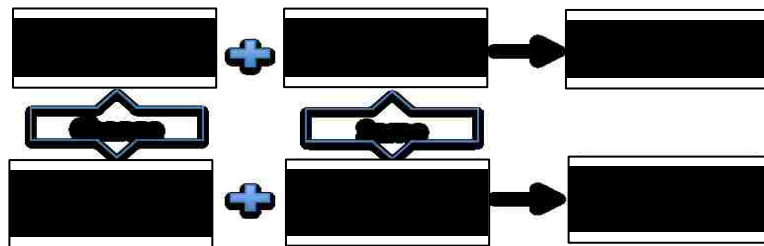
The experimental setup and procedure are shown in figure 2.5. The RF data were acquired from the *in vitro* stone phantoms for cases that showed the TA. The unbeamformed Doppler ensemble after the digitizer, which corresponds to the TA, was selected (light blue arrow in figure 2.5). Self-developed signals and Doppler processing algorithms were applied to the beamforming and Doppler power estimation. One pulse among 12 pulses (the default setting is 14 pulses - we usually withdraw the first two pulses because of a stability issue) within the Doppler ensemble was picked randomly (i.e. the 5th pulse in the sequence). The chosen pulse was interpolated in the frequency domain and programmed into a function generator (AFG 3022B, Tektronix, OR). The function generator was connected to the VUE directly and triggered by the machine. The simulated Doppler ensemble that contains 14 identical pulses was sent back to the machine by the function generator that was triggered by the VUE (the same trigger as the VUE sending transmitting pulses). The magnitude of the pulse was adjusted in the manner similar to what was done in the phantom experiment. The machine settings were also kept the same as those used in the phantom experiment.

The Doppler ensemble was captured from the machine and the corresponding Doppler power was calculated by employing the same signal and Doppler processing algorithms. Imaging parameters were set as follows: the sampling frequency of the machine was 20 MHz; the incident angle of Doppler pulses was zero degrees; the pulse repetition frequency (PRF) was 3 kHz; flash transmitting mode (plane wave) was used; the time-gain-compensation (TGC) was set to the minimum level for RF data acquisition to avoid signal saturation; the Doppler threshold was set to the level that background noise was just eliminated; and the color-written priority was set to the highest level. The peak voltage supplied to the transmitter was 35 V.

Figure 2.6 A shows the Doppler pulses of the Doppler ensemble recorded from the stone phantom imaging experiment. Although there are 14 pulses within the Doppler ensemble, the first two pulses are usually withdrawn because of the stability issue leaving twelve pulses on top of each other. Figure 2.6 B shows the corresponding Doppler power. There is a huge peak in the Doppler power curve, which indicates that there is variability within the chosen Doppler ensemble. Figure 2.6 C shows the Doppler ensemble acquired from the stable source (function generator) experiment. There are also twelve pulses on top of each other. Figure 2.6 D shows the corresponding Doppler power of the Doppler ensemble shown in 2.6 C. There is no obvious peak in the Doppler power curve comparing to figure 2.6 B. For convenient comparisons, Figure 2.6 A-D are all on the same scale.
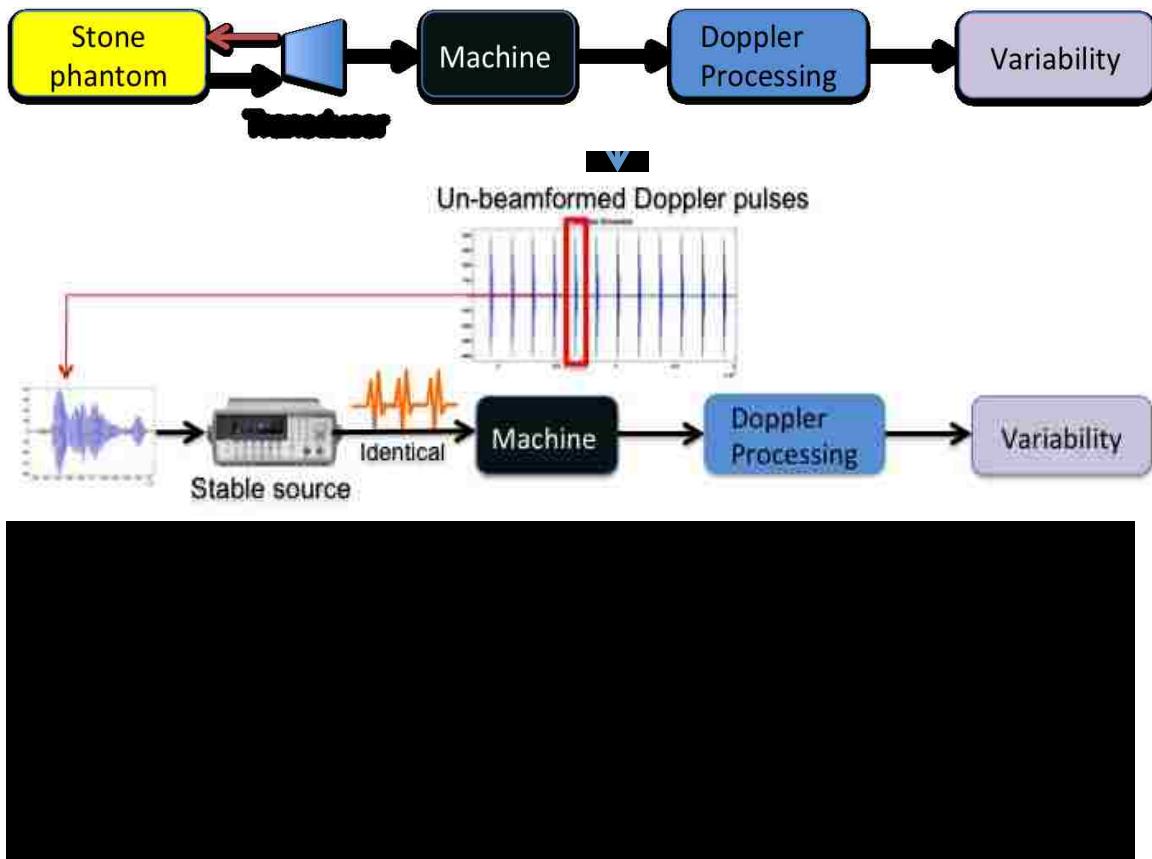
In figure 2.6, the waveforms of the pulses in 2.6 A are similar to those in 2.6 C. In figure 2.6 B, the large peak of corresponding Doppler power indicates that there is variability within the Doppler ensemble obtained from the stone phantom experiment. However, in figure 2.6 D, there is no obvious peak. This result shows that identical pulses sent out from the simulated source are still identical even after going through the machine. The repeatable results were observed in 6 human kidney stones. As the machine settings were the same in both phantom and stable source experiments, this result demonstrates that the machine is not the critical reason for the appearance of the TA.
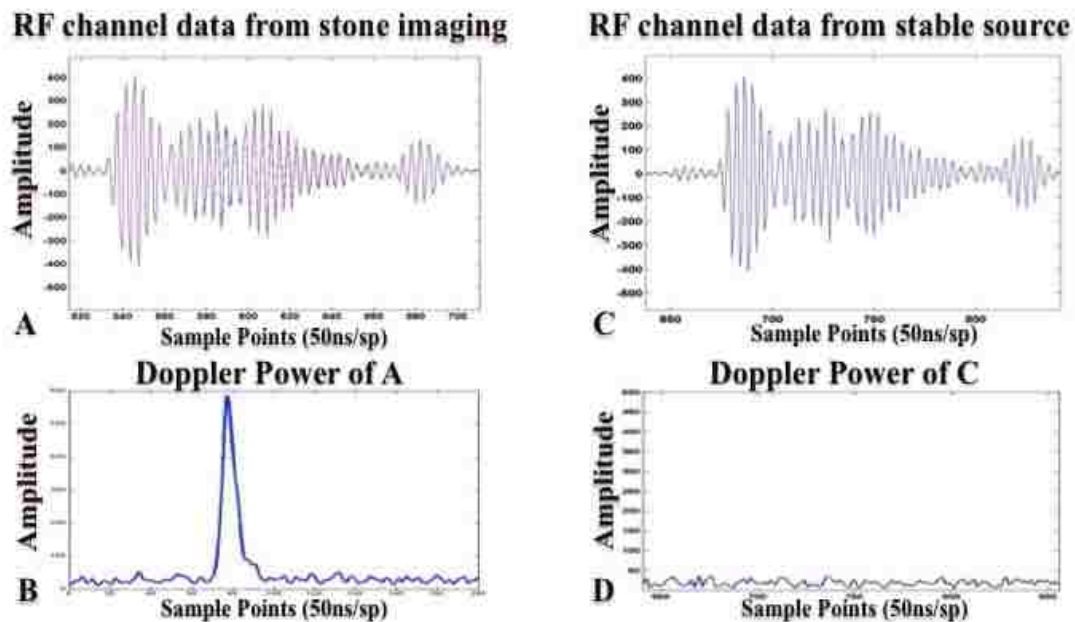
Meanwhile, the stability of the machine was also examined by a stable glass plate experiment. A glass plate (15 cm X 7.5 cm X 1.68 cm) was placed in a tank

that was filled with degassed water. The transducer (L7-4), held by a ring clamp, was set vertically to the glass plate and in parallel with the bottom of the water tank. The distance between the transducer and the glass plate was 3 cm. According to the corresponding Doppler power, there was no visible peak in the Doppler power curve.

Therefore, the variability within the Doppler ensemble, which is responsible for the TA, arises from the acoustical field rather than the circuits (imperfections) of the machine. From the acoustical side, any physical phenomenon that could introduce variability into the Doppler ensemble would be responsible for the origin of the TA; for example, the interaction between the acoustic wave and the cracks inside the stone, microbubbles on the stone surface, reverberations of the pulse within the stone, or strong reflection signals that saturate the digitizer. In order to better understand the origin of the TA, the investigation into the properties of the TA signals and carefully designed experiments that could separate effects from those hypotheses is critical.

2.3.2 Properties of the TA Signals

The origin of the TA

In order to investigate the origin of the TA due to the acoustical field, the position of color spots that represent twinkling on color images were studied, which is the easiest way. However, the locations with color may not reflect the original location of the variability because of the Doppler image processing effects, such as: post-processing of the image [54, 62, 66], color encoding priority [66], aliasing [66] and so on. In order to know more precisely where the TA happens, the raw per-channel RF data were used in the investigation.

In this study, human kidney stones (gel phantom and porcine kidney phantom) were scanned using the normal color flow Doppler imaging mode. Raw per-channel RF data of the Doppler ensemble were acquired for twinkling cases.

Then, the beamforming and Doppler processing algorithms were employed for RF data analysis. The beamformed Doppler ensemble was obtained and the corresponding Doppler power was estimated. Some machine parameters were set as follows: the sampling frequency of the machine was 20 MHz (4 sample points per wavelength); the incident angle of Doppler pulses was zero degrees; the pulse repetition frequency (PRF) was 3 kHz;the time-gain-compensation (TGC) was set to the minimum level as in RF data acquisition to avoid signal saturation; the Doppler threshold was set to the level that background noise was just eliminated; the color-written priority was set to the highest level; and the peak voltage applied to the transmitters was 35 V.
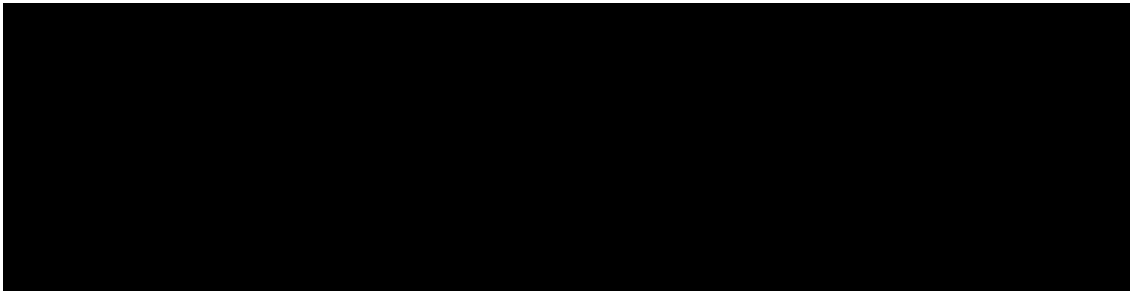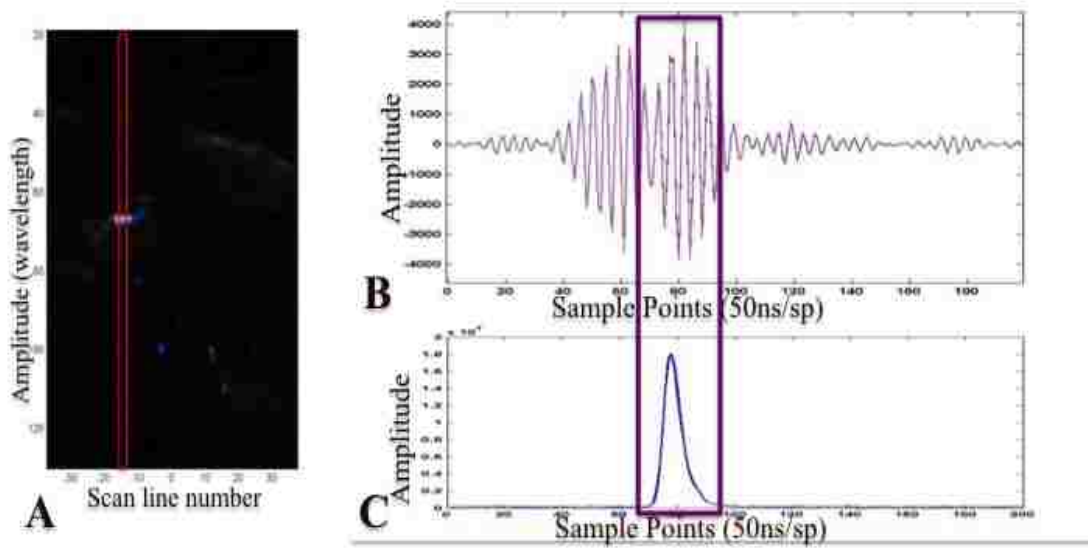
Figure 2.7 A shows the color Doppler image for the stone phantom experiment. The color spots represent the TA and the bright grey spots around represent the stone. Figure 2.7 B shows the beamformed Doppler ensemble (12 pulses on top of each other) for the red rectangular area (zoomed-in stone area) shown in figure 2.7 A. Figure 2.7 C shows the corresponding Doppler power of the Doppler ensemble shown in figure 2.7 B. Figure 2.7 B and 2.7 C are on the same scale. The purple box emphasizes the location of the variability within the Doppler ensemble. It is clear that the TA happened following the first reflection from the stone surface. For each stone in each scan, the location of the TA is similar; it does not change along with the change in scan time. This result is consistent for over 20 human kidney stones.

Twinkling and the strong (specular) reflection
In the last section, the observation that twinkling is mostly likely to appear distal to the echogenic reflection from the stone surface in cases with no signal saturation was discussed. In this section, we focus on whether there is a proportional relationship between the specular reflection from the stone surface and the TA. The variability within the beamformed Doppler ensemble, which is responsible for twinkling, was traced back to the per-channel RF data to identify whether the variability arose disproportionately on channels receiving the specular reflection. The details of the beamforming procedure are described in appendix B.

The flow chart on how the general beamforming algorithm works is shown in figure 2.8. Briefly, when scanning an object using ultrasound, the scattered acoustic echo will go many directions and hit multiple receiving elements. Because of the geometry of the transducer, ultrasound echoes propagate to the receiving element at different times. Suitable time delay compensation should be applied to align the signal from the same spot on the object in all receiving channels. After the alignment, those signals will be arranged into the same line.

Then the aligned information could be summed together to the amplitude of a coherent wavefront, which can be enhanced relative to background noise and directional interference.

After the summation, the beamformed Doppler pulses can be obtained. The variability within the beamformed Doppler ensemble can be located by the peak position of corresponding Doppler power. From figure 2.8, the aligned signals before the summation can be analyzed and the Doppler power can be calculated for each channel. The variability within each channel can then be estimated. The contribution from different channels to the variability within the beamformed Doppler ensemble can be evaluated.

In this study, human kidney stones (5-9 mm in length and 3-6 mm in width) were embedded in a polyacrylamide gel phantom (or porcine kidney phantom). All parameters used in the experiments are the same as those in the last section. RF data were recorded from pulse-echo ensembles using VUE. The variability within the beamformed Doppler ensemble was located and traced back to the per-channel RF data to identify whether variability arose disproportionately on channels receiving the specular reflection.

Doppler ensemble (12 pulses)

Doppler power of beamformed Doppler ensemble

Doppler power of aligned Doppler pulses (channel 33-40)

23
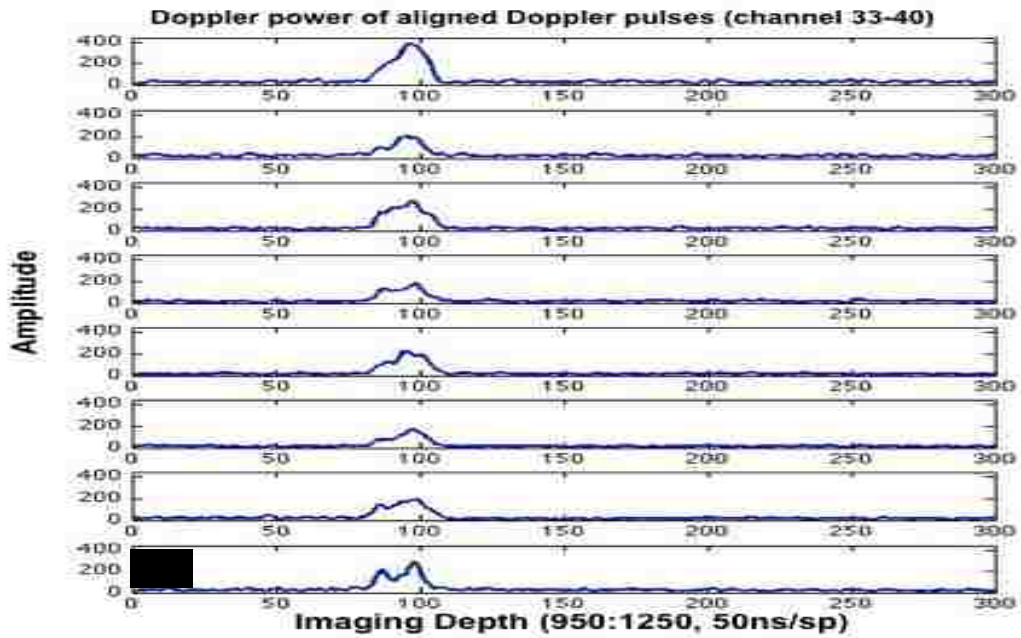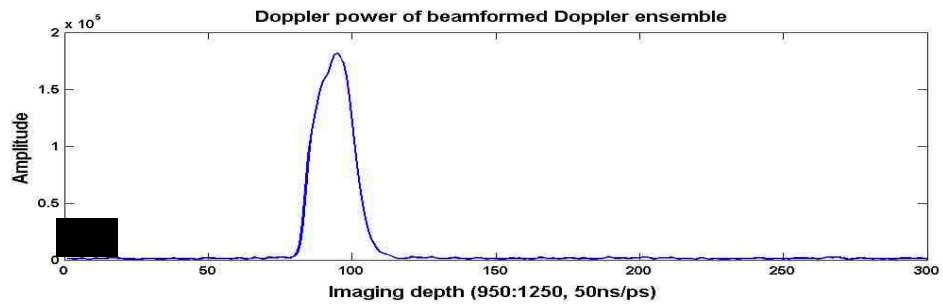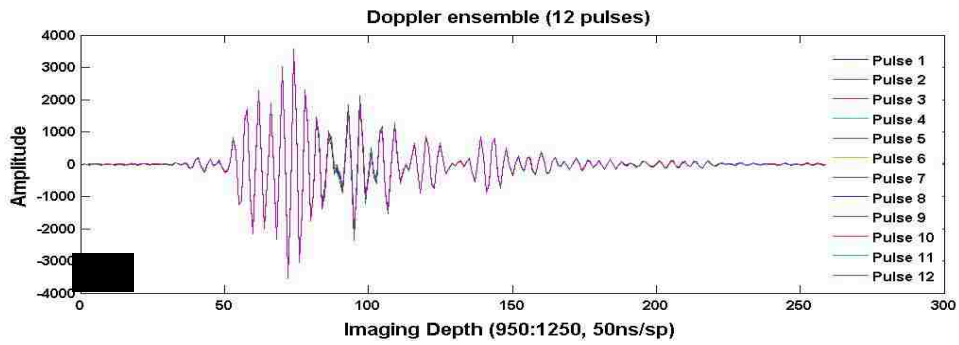
In figure 2.9A, one beamformed Doppler ensemble is shown. From the peak position of the corresponding Doppler power, the location of the variability within the Doppler ensemble can be easily identified. From figure 2.9B, the variability arises from the signal following the surface reflection from stone. Figure 2.9C shows an example of the corresponding Doppler power of the aligned unbeamformed Doppler signals, These results indicate that the peaks in the Doppler power curves arise from all channels rather than just from channels that receive specular reflection. In order to further investigate whether the variability arises disproportionately on channels receiving the specular reflection, figure 2.10 shows the peak amplitude of the specular reflection of aligned signals from all channels (circle marks with a blue curve) and the peak value of the corresponding Doppler powers (histogram).
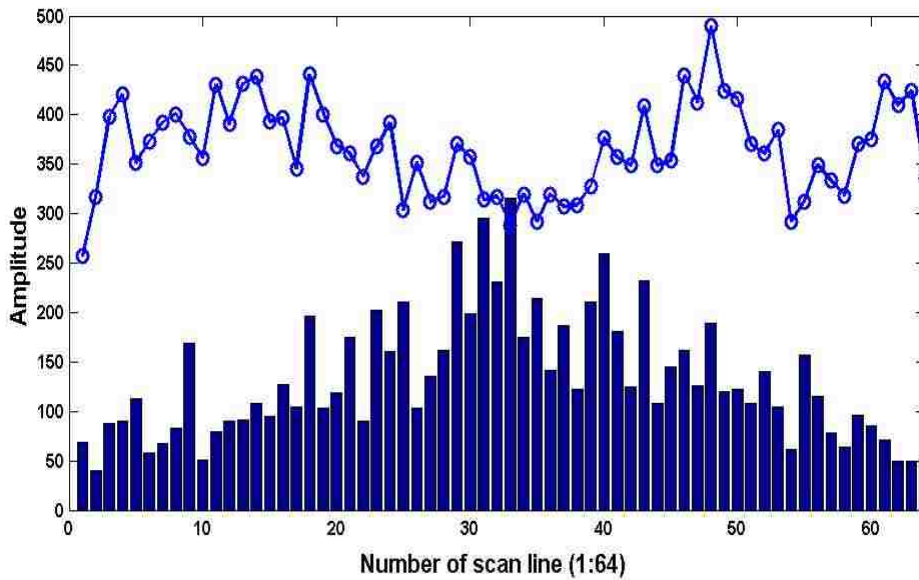
In order to clearly show the maximum amplitude of the specular reflection curve, the curve was shifted up by 150 in the y-axis. From this figure, the strong specular reflections were received on channels 3 to 20, 45 to 49 and 60 to 64. However, the strongest Doppler power of the aligned Doppler signal was observed around channel 30. This result demonstrates that neither the amplitude of the Doppler power nor the appearance of the Doppler power depends on the specular reflection. Every channel, more or less, contributes to the total Doppler power of the beamformed Doppler ensemble. The varying signals that correspond to the twinkling artifact have the appearance of arising from a point source within the stone rather than simply following the strong reflection.

Random Amplitude Effects

During the investigation into the mechanism of the TA, we observed that for most of the twinkling cases, there is/are usually one or multiple pulses abnormal from others within the wall-filtered Doppler pulses. This phenomenon is referred to as an 'abnormal event'. The 'abnormal' here means that the pulse(s) has an amplitude that is much higher than any other pulse, as shown in figure 2.11. The peak of the yellow curve has much larger amplitude than that of any other pulse, and this high amplitude leads to a big Doppler power for a relative sample volume. Since there always are 12 pulses within the processed Doppler ensemble, does this 'abnormal' happen randomly within the Doppler ensemble or is there a certain sequence of pulses that is more likely to show the abnormal event than other pulses? To answer these questions, the following investigations were performed.

Human kidney stone phantoms were scanned using color Doppler ultrasound with multiple Doppler transmitting powers. RF data from the twinkling cases were collected and analyzed. The number of abnormal pulses within the wall-filtered Doppler pulses was counted in the following way. The wall-filtered Doppler signals were also called Doppler residuals. Within one Doppler ensemble (or one

frame), the maximum amplitude of the Doppler residuals was found. If the peak amplitude of the absolute value of the Doppler residuals was stronger than 3 dB of the mean peak amplitude within the channel and it was also 3 dB stronger than the noise level, the abnormal event was counted. Otherwise, the pulse was treated as a normal pulse and 0 was counted for this channel. When the counting was finished, the total abnormal events were summed. Figure 2.12 shows the relationship between the sequence of pulses (range from 1 to 12) and the number of abnormal events that happened on each sequence pulse. There were three kidney stones scanned and 440 frames taken into the analysis.
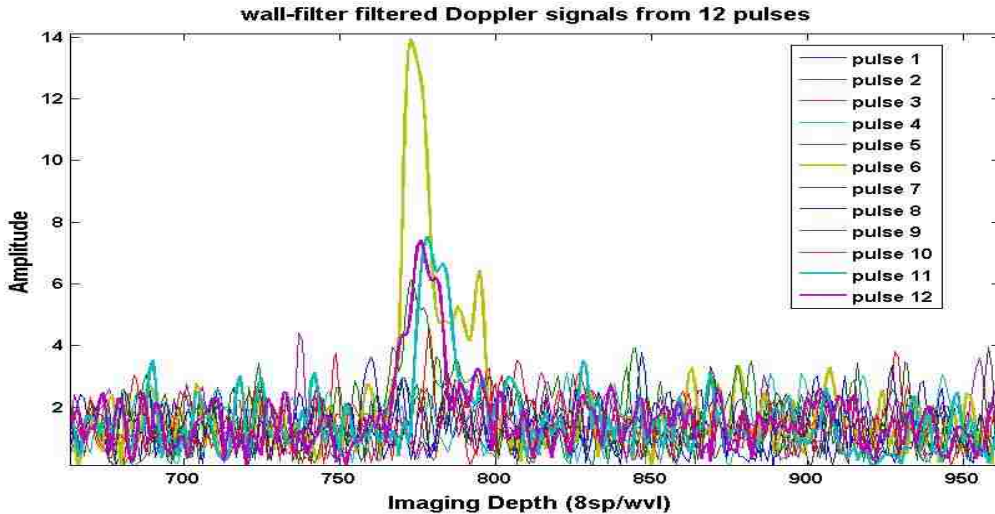
From figure 2.12, every pulse has a big chance to appear abnormal except the 1st and the last pulse. There are 1660 abnormal events that happened within 440 frames, with 4 abnormal events happening on average in the channel when the TA appears. This abnormal property was observed on many TAs from kidney stones.
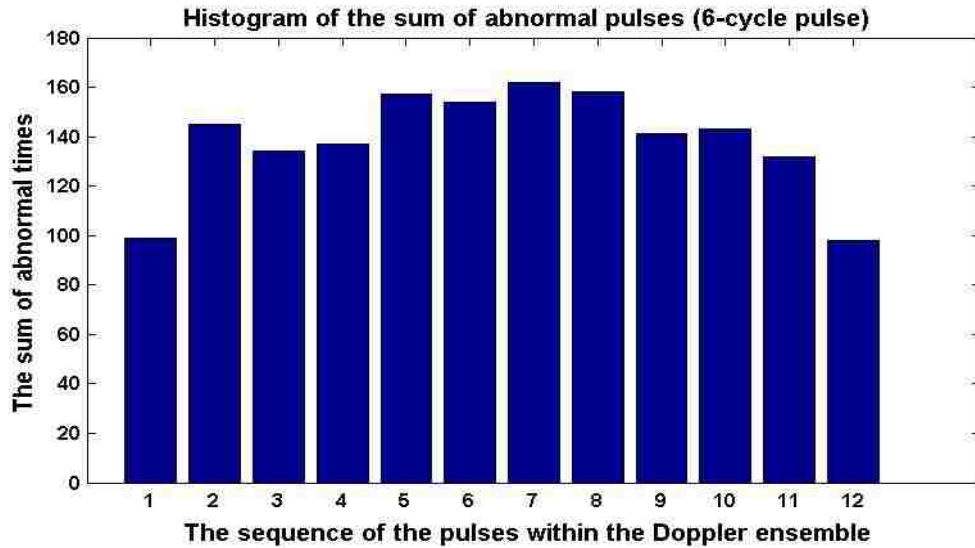
Therefore, the TA or TA signals should have the following properties:

1) The location of the TA is fixed. Once it happens, the location of the TA does not change with the change in the scan time.

2) The twinkling signal arrived later than the surface reflection, but there is no relationship between specular reflection and the twinkling. The source of the twinkling performs omni-directionally.

3) The abnormal event happens randomly within Doppler pulses. The possibility of an abnormal occurring for each pulse seems similar except for the first and last pulse within the Doppler ensemble. This observation means that the source of the twinkling artifact behaves stochastically during the interaction with the acoustic waves.

2.3.3 Sub-hypotheses tests

Based on the investigation into the properties of the TA and twinkling signals, several sub-hypotheses on the mechanism of the TA, such as the inhomogeneity of the stone (cracks), microbubbles and stone ringing were proposed. The work

in this section is mainly on testing and proving the microbubbles hypothesis. The modeling work on the stone ringing is also briefly introduced.

Micro-bubbles

a) Stone overpressure experiments

Bubbles respond to pressure forces and oscillate nonlinearly when periodically driven by acoustic waves. [67] When interacting with the Doppler pulses, this nonlinear oscillation could affect the sequence pulses and introduce variability into the Doppler ensemble. The nonlinear effects could cause random amplitude altering that is similar to the signal properties of the TA discussed previously. In this study, tests were performed to understand whether microbubbles relate to the origin of the TA. A well-known technique – an overpressure [68-69] test that can suppress bubbles and cavitation is involved in this investigation. Since the bubble is very sensitive to the acoustical pressure field, the TA could behave differently under different pressure conditions if bubbles are related.
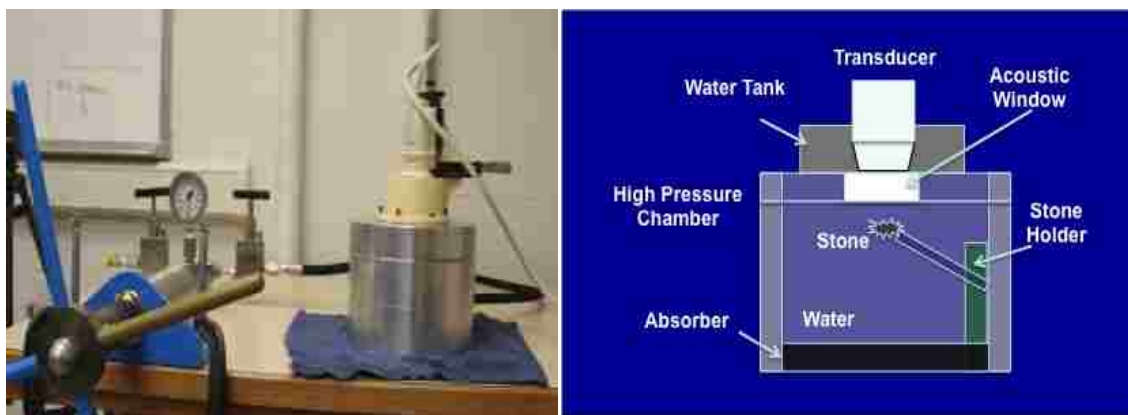
The overpressure system and experimental design are shown in figure 2.13. Briefly, the whole chamber was made of aluminum (inside diameter of 11.2 cm and depth of 7 cm). A rubber absorber (1 cm thick) was on the bottom of the

chamber. The stones were fixed on a stone holder that was screwed into the bottom of the chamber. A polystyrene acoustical window was placed in the middle of the lid for acoustic transmission. The acoustical window was a 0.85 inch cylinder (5.3 cm in diameter, longitudinal sound speed 2.4 mm/us; shear sound speed 1.15 mm/us; Density 1.05 g/cm^3; Z = 2.52 MRayls; loss of 1.8 dB/cm at 5 MHz). The transducer fixed on the positioning system was placed perpendicularly to the chamber lid. The surface of the transducer did not attach to the acoustical window during the experiment to avoid transducer displacement that could be caused by the acoustic window bending under high-pressure. The transducer and the chamber were coupled with degassed water and the gap between the transducer and the acoustic window was 1 mm in the experiment. The position of the transducer was adjusted by the positioning system to find the best twinkling spot on the stone.

The experiment procedure was as follows:

1. Kidney stones were soaked in water for over 48 hours. In order to keep the stone stabilized during the experiment, the stone was glued to a bronze needle using 5-minute epoxy (McMaster, CA). The two components of the epoxy were mixed in a weight tray for 2-3 minutes and the stone was glued to the tip of a bronze needle. The stone was held against the needle for around 5 minutes to make sure the stone was well-connected to the needle. The size of the glue spot varied (1 – 3 mm), but the sizes of the glue spots were small enough to avoid

affecting the TA. After the glue dried, the needle-mounted stones were soaked in water for over 48 hours.

2. A tank of water was degassed for as least 1 hour until the oxygen saturation was below 15%. The chamber was filled with degassed water. The stone was fixed on a stone holder that was screwed to the bottom of the chamber. The stone was positioned close to the acoustic window and there was no contact between the stone and the acoustic window. The lid was closed and fixed (screwed to the chamber body) in the water. Additional attention was made to look for bubbles trapped under the acoustic window since there was a small slope surrounding the acoustic window due to a difference in thickness between the acoustic window and the rest of the lid. Then, the chamber was gently moved to a bench. Since the bench, or the pressure adjusting system, and the VUE system were separated (VUE was on a cart and the pressure adjusting system was on a bench), there was no touching or knocking on the chamber bench during the experiment. A small water tank was fixed on top of the chamber lid. When the system was set up, the distance between the transducer and the stone was around 3 cm. Twinkling was carefully found by adjusting the positioning system (2-D, up and down &back and forth; if it was necessary to adjust the other dimension, the small tank on top was rotated).

3. After the system was set up under normal pressure, twinkling was filmed for about 1 hour to obtain the whole twinkling pattern for certain conditions. RF data were collected for the normal pressure condition.

4. The pressure was slowly increased by winding the wheel to inject water into the pressure chamber. It was about 11 ml of water per syringe. The whole process involved to increase the pressure from 0 psi to 1300 psi took 5 minutes. The raw RF data were captured under high-pressure and twinkling was filmed for around 1 hour. Then the stone was left under static high-pressure for several hours to let the bubbles fully dissolve. These time periods ranged from 4 to 8 hours depending on the experiment conditions.

5. Before decreasing the pressure, the screen was filmed for 5 – 10 minutes. Then the pressure was slowly decreased to the normal level in 5 minutes, before twinkling was again filmed for 1 hour. Then, the RF data were captured for the pressure-released condition.

6. All videos were compared for different pressure conditions and the corresponding RF data were analyzed to quantify the TA.

Nine human COM kidney stones that 6-12 mm in length and 4-8 mm in width were employed in the overpressure experiments. Some of them are shown in figure 2.14. As for the color Doppler mode used for the experiment, the peak voltage applied to the transmitters was 35 V; the transducer was driven at its central frequency of 5 MHz; a 3 cycles pulse was used as a Doppler pulse; there were 14 Doppler pulses within the Doppler ensemble; the Doppler pulses were transmitted at 0 degrees and in flashing mode; the sampling frequency was 4 sample points per wavelength (20 MHz); the PRF was 3 kHz; and the TGC was set to 80%~85% of the maximum and the gain for different depths were aligned since there was no loss that depended on depth.

Figure 2.15 shows twinkling on the screen captured under different pressure conditions. From figure 2.15, there was an obvious TA shown on the stone before increasing the pressure, as shown in the left image. The middle image shows how twinkling behaves when high-pressure was applied. There was no color shown during the overpressure phase of the experiment. Then, the pressure was released and the twinkling returned immediately to the screen. The results were repeatable on all kidney stones.

In order to describe the twinkling artifact more precisely, a new parameter, N%, that was estimated based on the RF data analysis was introduced. This new parameter N% was used to describe how well the stone was lighted by color. The N% is defined as:

$$N\% = \frac{N_{pcolor}}{N_{pstone}} \times 100\% \qquad\qquad (2.1)$$

Where N_{pstone} is the number of pixels occupied by stone, which was circled and calculated based on the B-mode image, and N_{pcolor} was the number of colored pixels counted when the corresponding Doppler power was 3 dB stronger than the noise level. The noise level was estimated based on an average of the Doppler power within the total Doppler image area.
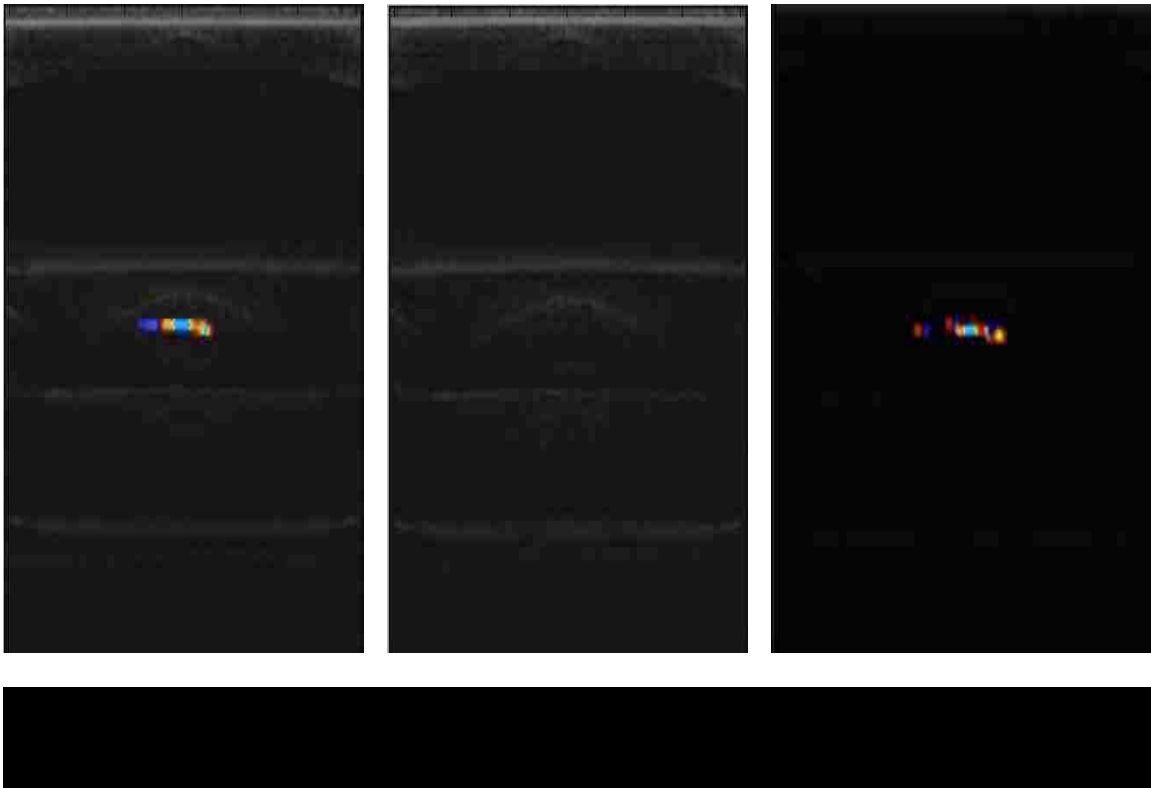
Figure 2.16 shows the N% of three different pressure conditions. From left to right, the N% before adding pressure, during overpressure and after pressure was released, was 17.3%, 3.9% and 14.5%, respectively. The N% was calculated from 80-100 frames per stone, 9 stones in total. A student's t-test was applied for paired conditions using Matlab and the hypothesis was rejected at the 0.05 level. The results showed that the p-value of N% before adding high-pressure and after high-pressure released was >> 0.05, which means there is no statistical significance between those two pressure conditions. But the p-value of

N% between before adding pressure and during high-pressure or after high-pressure was released and during high-pressure was both << 0.05, which shows that there was statistical significance between both of those two pairs. These N% results confirmed what we observed from the videos in a more quantitative way. There is no difference on the TA before adding pressure and after pressure was released.

Back to the mechanism part, these results suggest that microbubbles are involved. Again, we should emphasize that the bubbles mentioned here are on a very small scale (should be less than 10 μm) and are not visible. Under normal pressure, the microbubbles were driven by periodic Doppler pulses to oscillate randomly. This oscillation introduced variability into the Doppler ensemble and caused the TA. As the pressure increased, the microbubbles were suppressed and there was limited oscillation, which resulted in the restricted variability within the Doppler ensemble. Interestingly, when the pressure was released the TA returned immediately, which may give us a clue to differentiate what kind of microbubbles is responsible for the mechanism of the TA. Usually, free bubbles would be totally compressed during overpressure. However, Apfel and Crum among others [70-71] have developed a "crack and crevice model" for how bubbles trapped within solid particles are stabilized against overpressure. Therefore, since the twinkling recovered from the pressure release, the TA is most likely explained by crevice-bubbles on the stone rather than free microbubbles.

However, there is another possible explanation for the results of the overpressure experiment – cracks. [72-73,100] When an acoustic wave interacts with cracks, there will be a nonlinear acoustic phenomenon that results in the generation of chaotic noise-like acoustic excitations. [72] The process could also introduce variability into the Doppler ensemble and hence induce the TA. For human kidney stones, there could be both microbubbles and cracks, and the combined effects are difficult to separate.
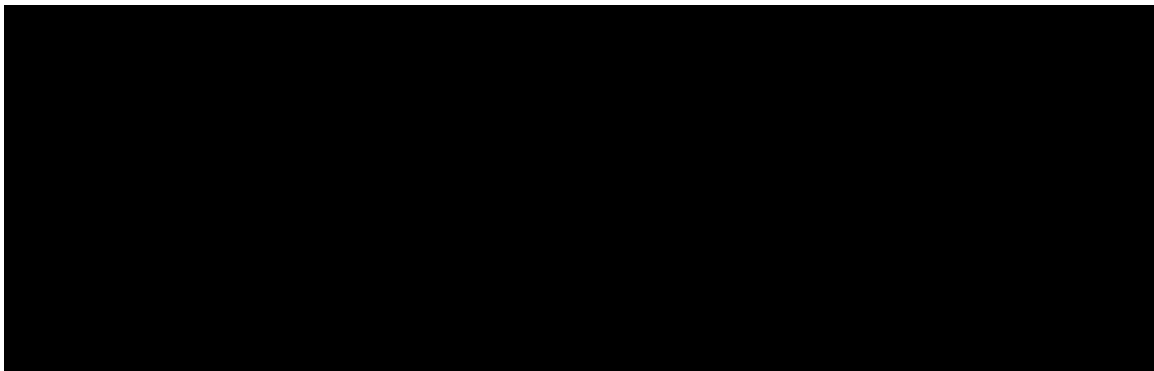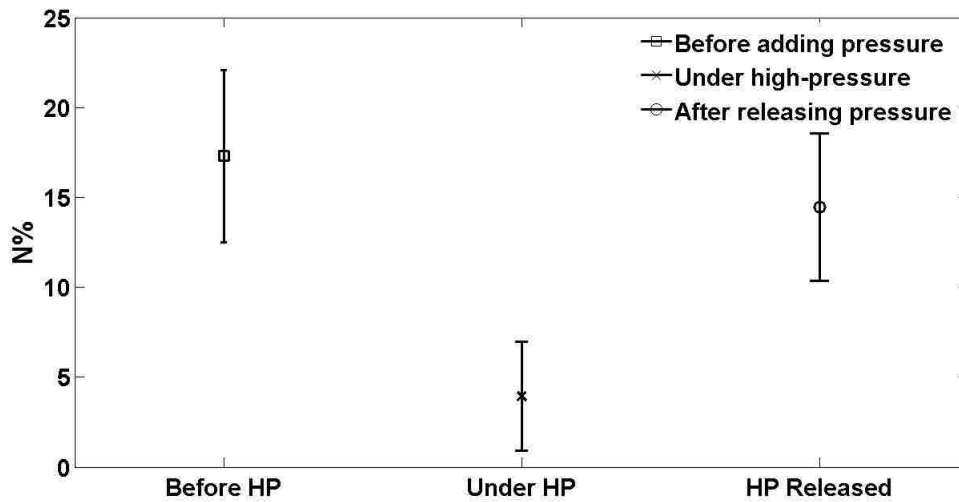
b) Acrylic sphere overpressure experiment

In order to see whether microbubbles, themselves, could cause the TA, a new experimental object that contains only microbubbles or cracks would be a benefit. Acrylic spheres (Small Parts, Inc. Logansport, IN, USA) with varying diameters are shown in figure 2.16.   The advantages of the acrylic spheres are: 1) they are very uniform such that there are no cracks; 2) the surface is smooth such that there is no crevice; 3) the shape is symmetric and regular for ease of modeling; and 4) the material is very soft such that it is easy to cut crevices on using a knife. When the sphere is put in the water, the gas should be trapped in the crevices and create crevice bubbles.
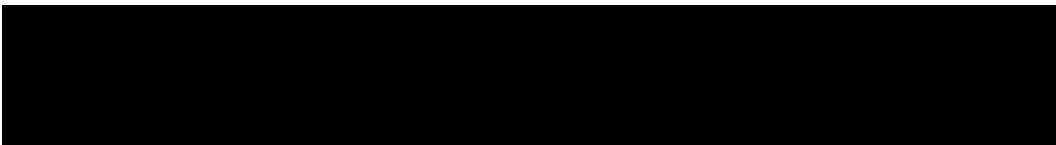
First of all, the twinkling was tested between same size spheres with smooth surfaces and rough surfaces (crevice, created by using a knife with a 0.3 mm thick blade). In our hypothesis, the smooth surface should not cause any twinkling while the rough sphere with the created crevice bubbles should show the TA. The imaging and Doppler parameters were the same as those we used in the stone overpressure experiment. The test results are shown in figure 2.18. From the test results, the sphere with the created crevices twinkled well while

there was no twinkling shown on the sphere with a smooth surface. This suggests that crevice bubbles are enough to induce the TA.

Next we compared the twinkling shown on the rough surface sphere with the twinkling shown on the stone by using an overpressure test. The experimental procedure was similar to what we used before except the object glued to the needle was an acrylic sphere with a rough surface rather than a human kidney stone. Spheres of different size (1/2", 3/8" and 1/4" in diameter) with rough surfaces were tested in the experiment.
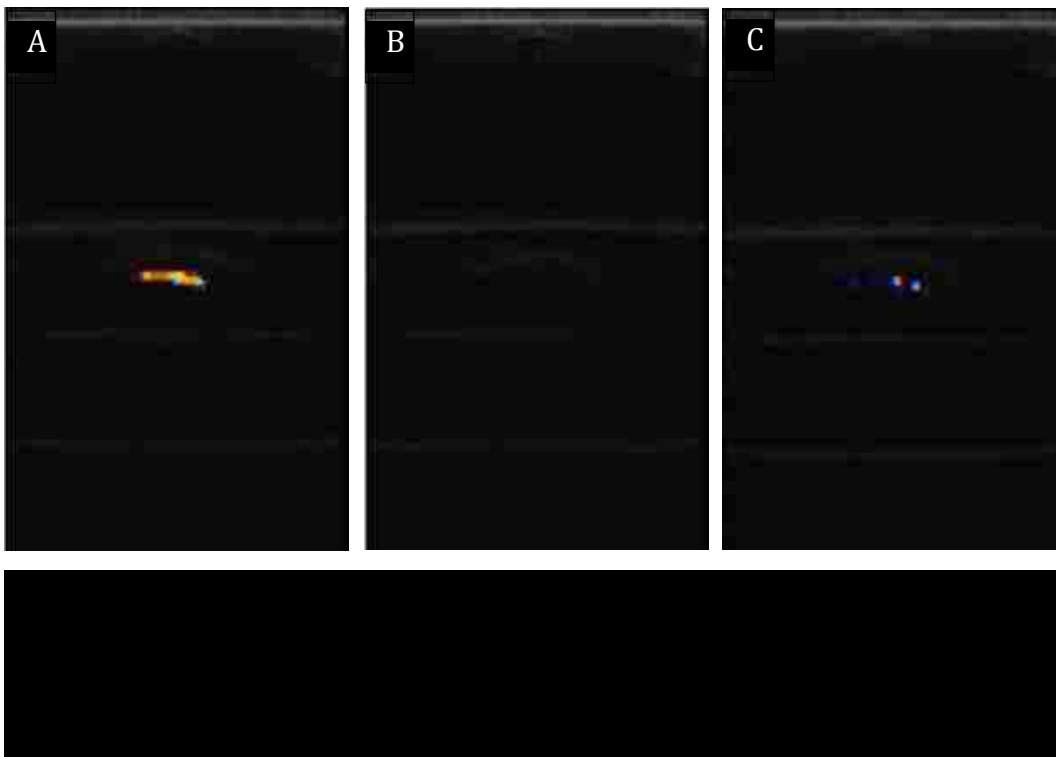
The results are shown in figure 2.19, and were similar to what we observed in the stone overpressure experiment. Before adding any pressure, the twinkling was shown on the screen; during overpressure, the twinkling disappeared and after releasing the pressure twinkling recovered immediately. In this case, twinkling was not as strong as was observed before the overpressure procedure. This may

be due to free bubbles that existed before adding pressure were suppressed during the overpressure and did not recover. The other explanation is that the crevice bubbles did not fully recover. Therefore, we have finally separated the effects from the crevice bubbles and the cracks. These results demonstrated that crevice bubbles are enough to cause the same TA as we observed on stones.
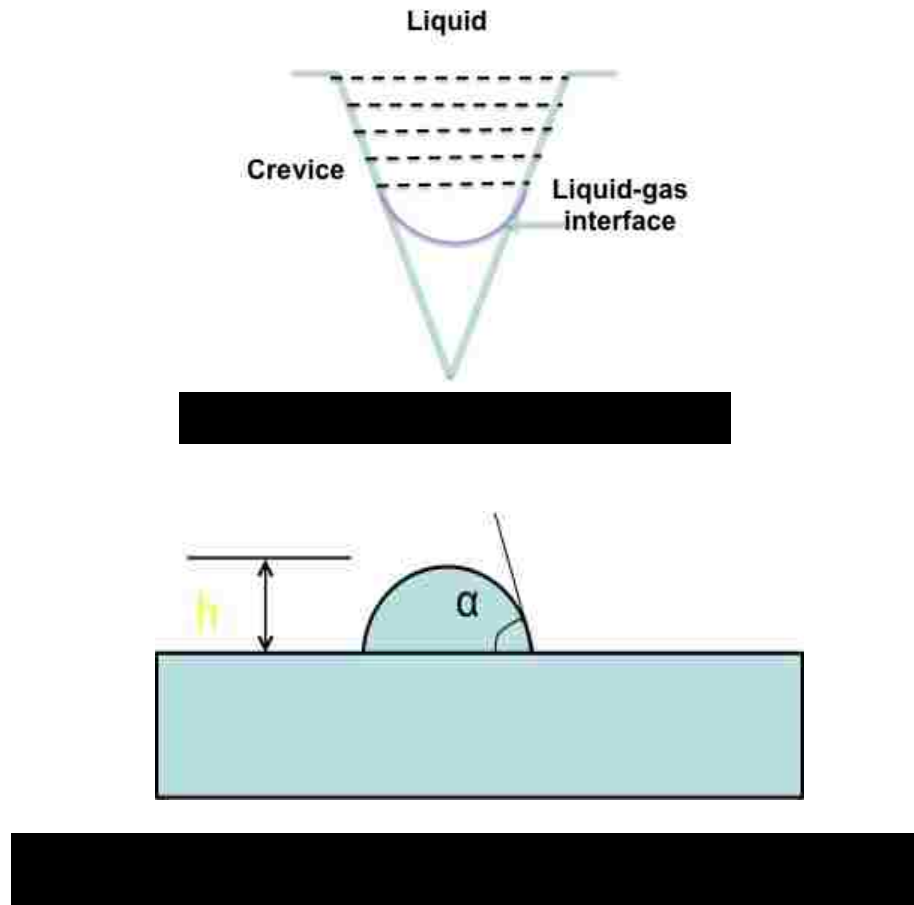
c) Wetting test

So far, the microbubbles hypothesis has been tested and proved by using an overpressure procedure. Are there any other ways to confirm our results from the overpressure experiment? From the definition of crevice bubbles, the bubbles are

caused by imperfect wetting of the crevice in the mote (as shown in figure 2.20). When a drop of liquid is dropped on a solid surface, how well it can wet the surface is decided by the surface tension between the liquid and the material of the solid. Figure 2.21 shows a drop on a flat plate. The height of the drop can be calculated by the equation [74]:

$$h = \sqrt{\frac{2\gamma(1-cos\alpha)}{g\rho}} \qquad (2.2)$$

Where γ is the surface tension of the liquid; ρ is the density of the liquid, and g is the acceleration due to gravity. In other words, the better the liquid wets the surface, the lower the height of the drop, and the larger the area of the drop. Therefore, a liquid that is capable of better wetting the acrylic sphere would help reduce the crevice bubbles, which would affect the TA if crevice bubbles causes twinkling.
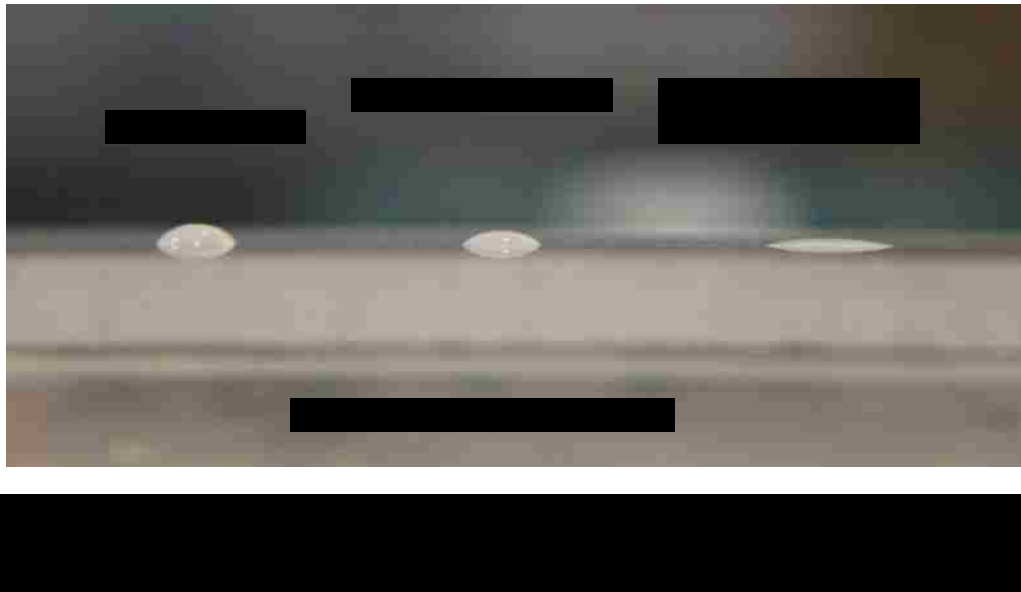
Initially, two liquids, Sodium Dodecyl Sulfate (SDS) [75-76] and 70% (V: V) ethanol, which are widely used to suppress cavitation were compared with water. Figure 2.22 shows the results of the comparison. Briefly, the same volume of each liquid was dropped on an acrylic plate that was composed of the same material as the

sphere. The heights of the puddles were compared under a magnifying glass. The SDS was 0.5 critical micelle concentration (CMC) and the ethanol was 70% V:V. Among those three puddles, it was apparent that ethanol wets the acrylic plate the best. Therefore, ethanol was chosen for the wetting tests.
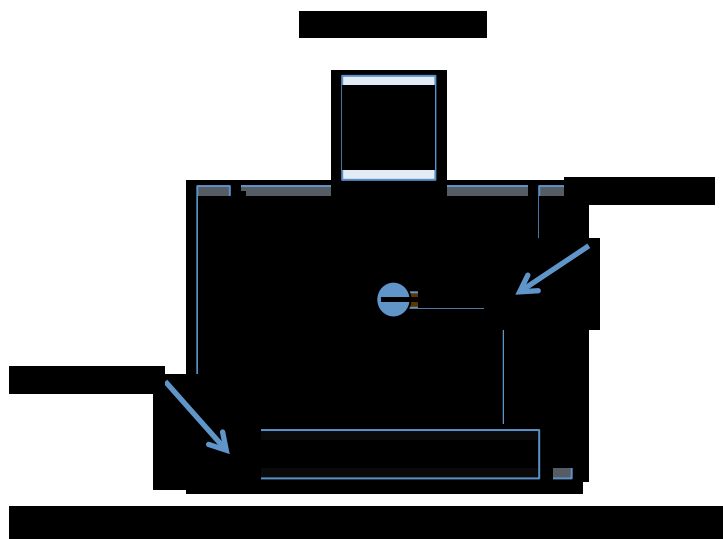
The experimental setup is shown in figure 2.23. The sphere was glued to a bronze needle using 5-min epoxy and placed on the holder parallel with the bottom of the water tank. A rubber absorber was placed at the bottom of the tank in order to eliminate reflection. The transducer was fixed on the positioning system perpendicular to the sphere. The rough surface of the stone was rotated to face the transducer. For the experiment, the stone was scanned in degassed water, and twinkling was filmed. Next, the water was sucked our and 70% V:V ethanol was added to fill the tank. A plastic pipette was used to create streams around the sphere for better contact between the sphere surface and ethanol. The scan was performed until the liquid calmed down and twinkling was captured. Then, ethanol was sucked out and the degassed water was added in and sucked out twice to clean any ethanol that remained in the tank. Plastic pipettes were used for cleaning the sphere. Degassed water was added again after the two rinses, and the sphere was scanned under water to see whether there was any

change in twinkling. Twinkling was again recorded from the screen. All the imaging and Doppler parameters of the VUE were the same as those used in the overpressure tests.

As shown in figure 2.24, there was obvious twinkling when the sphere was under water, while there was restricted TA on the screen when the liquid changed to ethanol. When the liquid returned to degassed water, twinkling came back. These results confirm that when the sphere was wetted well, the TA was limited. In other words, crevice bubbles play a very important role in inducing the TA.
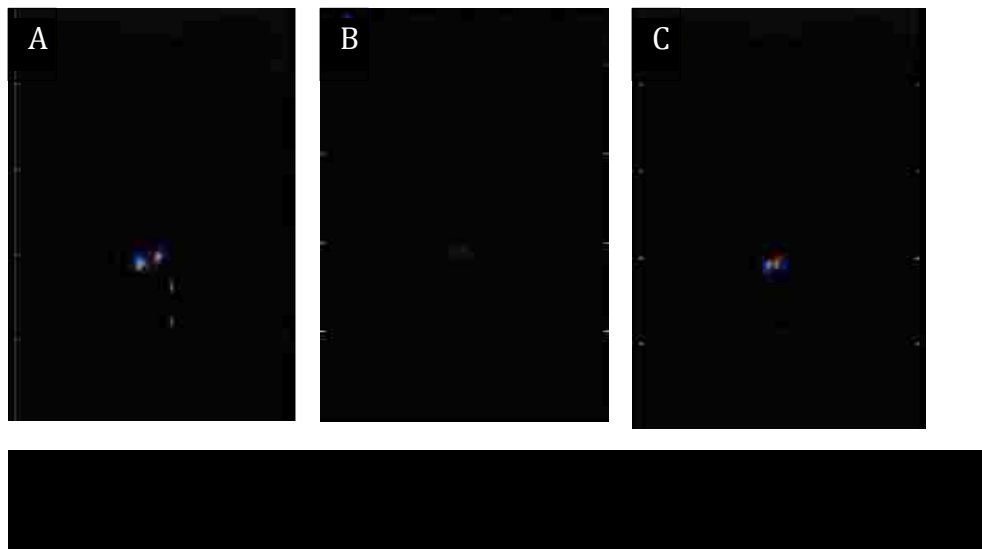
The sound velocity in ethanol (1144m/s) is different from that in water (1450m/s). If the sound speed changes, the beamforming algorithm will not accurately estimate the time delay between receiving channels (appendix C). Is the disappearance of the TA related to the imperfection of the beamforming? Fortunately, the VUE provides a feature that we can change the sound speed for imaging reconstruction on the control panel *in vivo*. In the wetting test, the sound speed was changed from 1100m/s to 1500m/s. Comparing to the TA shown under water, there was limited TA shown in the ethanol during the adjustment of the sound speed. This result shows that the sound speed change is not the critical reason why there was no twinkling in the ethanol.

d) Fresh stone tests

So far, both overpressure and wetting experiments on the old stones suggest that crevice bubbles should be the mechanism of the TA. However, there is one more question that needs to be answered: whether the mechanism of the TA on old stones is the same as that *in vivo*? The difference between old stones and kidney stones *in vivo* is that for the old stones were dried out for storage. It is hard to exclude bubbles in the *in vitro* cases even when they were soaked in water for a very long time or when placed in a vacuum because of the imperfection in wetting. On the other hand, *in vivo* stones are never dried out and have limited direct contact with air - there are no introduced crevice bubbles. If the *in vivo* stones also behave in a similar way as what we observed with the old stones, we can conclude that the mechanism of the TA is the same for both *in vivo* and old stones. In order to determine whether there are crevice bubbles on the *in vivo* stones, fresh kidney stones that were just removed from patients were tested.

A thank you goes out to Dr. Harper and Dr. Hsi for performing the medical procedure. Two kidney stones (6-7 mm in length and 4-5 mm in width, as shown in figure 2.25) were taken directly from the patients. Briefly, after induction of general anesthesia, the patients were placed in a prone position. Through an existing nephrostomy tube, the nephrostomy tube tract was dilated to 30Fr. A percutaneous access sheath was placed. A grasper was used to remove small remaining fragments directly from the kidney into a plastic container that was full of the degassed saline. The stones were transported to the lab within the sealed container. In order to keep contact with the air minimal, the whole experimental preparation and the experimental procedures were performed in degassed water. Briefly, the container was opened and the stone was grasped by tweezers and glued to a tip of bronze needle using 5-minute epoxy (McMaster, CA). Until the glue became solid, the stone was transported in degassed water to the high-

pressure chamber that was submerged in a big acrylic water tank, fixed on the stone holder that screwed to the bottom of the pressure chamber. The stone was positioned close to the acoustic window and there was no contact between the stone and the acoustic window. The lid was closed and fixed (screwed to the chamber body). A small water tank was fixed on top of the chamber lid. When the system was set up, the distance between the transducer and the stone was around 3 cm. The twinkling was carefully found by adjusting the positioning system (2-D, up and down &back and forth; if it was necessary to adjust the other dimension, the small tank on top was rotated). The following experimental procedure was the same as was described previously in the overpressure experiment with the same imaging and Doppler parameters.

The results showed similar phenomena as we observed on old stones. Figure 2.26 A, B and C shows how twinkling behaved before adding pressure, during high-pressure and after high-pressure was released, respectively. Before adding pressure, there was an obvious TA on the screen; following the increase in pressure, the twinkling became weaker and weaker until it disappeared totally from the screen (the threshold for two stones were under 50 psi and 250 psi); when pressure decreased to the normal pressure level, the twinkling recovered and was shown on the screen again. Figure 2.27 shows the N% change following the change in pressure. The N% before adding high pressure, during high-pressure, and after high-pressure was released was 9.1%, 1.5% and 7.4%, respectively. The results showed that the p-value of N% before adding high-

pressure and after high-pressure released was >> 0.05, which means there was no statistical significance between those two pressure conditions. But the p-value of N% between before adding pressure and during high-pressure or after high-pressure was released and during high-pressure was both << 0.05, which shows that there was statistical significance between both of those two pairs. The result confirmed those obtained from the old stones. The crevice bubbles are also present on fresh stones that had limited air contact.
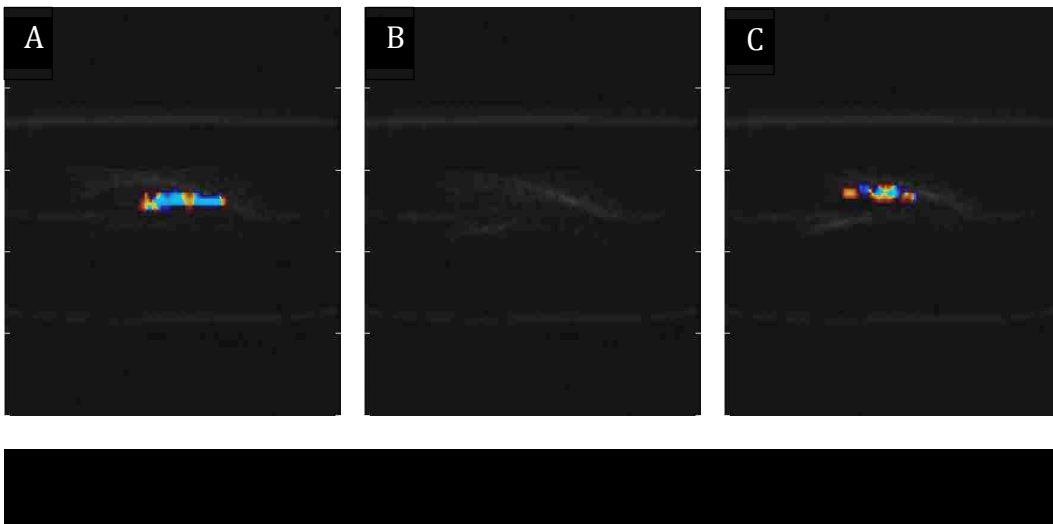
e) Stone ringing - modeling

Until now, the microbubbles hypothesis was tested and discussed. In this section, the stone-ringing hypothesis is evaluated.

Impuse Response of Backscattering from a COM Shere
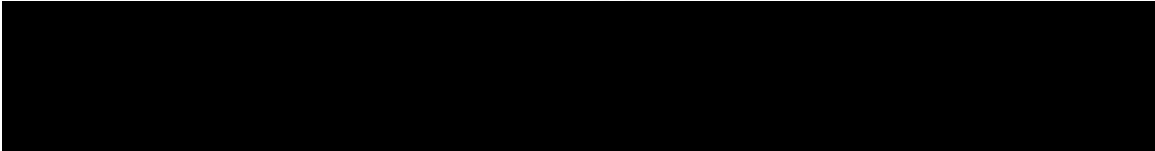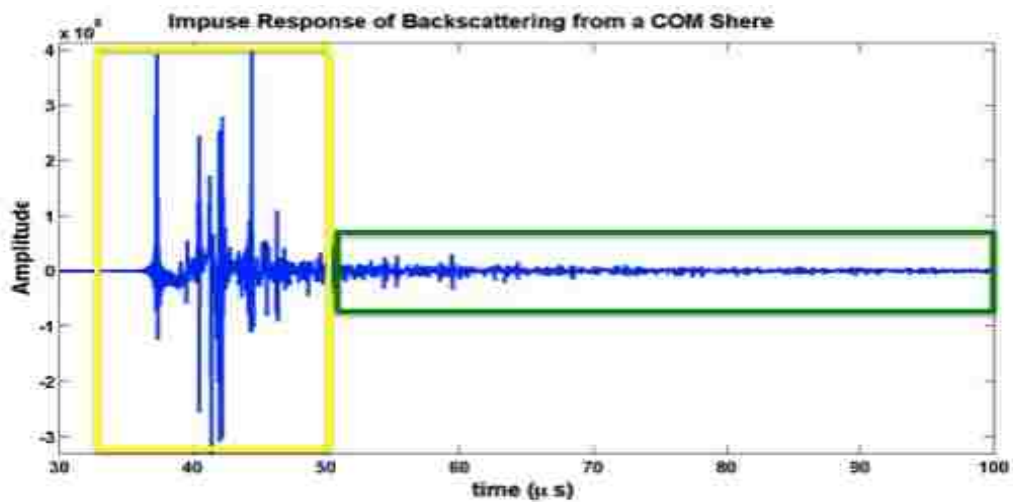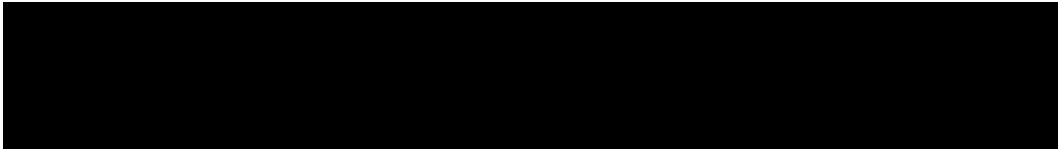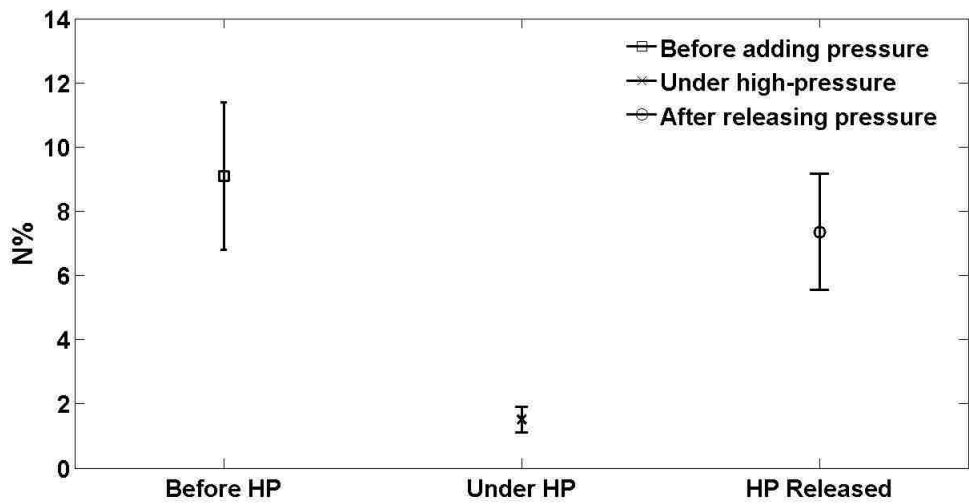
When we hit a bell, the bell will vibrate and produce sound. The stone behaves similarly when it is hit by an acoustic wave. Figure 2.28 shows an impulse response of backscattering of a pulsed plane wave from a 4 mm diameter

spherical Calcium Oxalate Monohydrate (COM) stone that was placed 3 cm away from the transducer. The stone and the transducer were both in the water. The first reflection from the stone surface came at t = 37.33 µs, since its travelled distance should be 56 mm (forward and back). The yellow rectangular part shows the first reflection as well as the following bottom reflection, shear and surface waves; the green rectangular part shows the ringing signals that will become weaker and weaker following the increase in travelled distance. The signals vary with time. So, when one Doppler pulse within the Doppler ensemble hits the stone, the ringing signal could affect the following Doppler pulses. Different parts of the ringing signals could be captured by the sequence of pulses and result in variability within the Doppler ensemble.
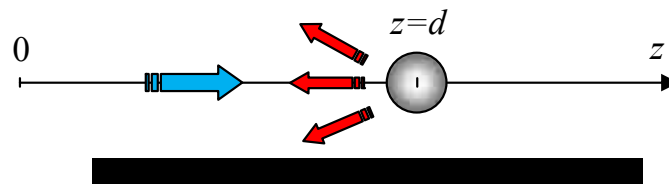
When an acoustic wave interacts with the stone, there are multiple modes included, such as shear and longitudinal waves bouncing inside the stone and surface waves going around the stone surface. In order to study the origin of twinkling signals, a model that was developed by Dr. Sapozhnikov to describe the backscattering of a pulsed plane wave from an elastic sphere is introduced.

The detailed description of the model is in Appendix D. Briefly, we consider an elastic sphere of radius a, with its center having a coordinate z=d. A plane wave propagating along the z-axis is scattered at this sphere, as shown in figure 2.29. The incident wave at the origin z=0 has the waveform $p_0(t)$. The scattered wave at the same point z=0 (i.e. the backscattered signal) has some waveform $p(t)$. Because the scattering is a linear process, the backscattered signal can be written as a convolution integral:

$$p(t) = \int_0^\infty H(t')p_0(t - t')dt' \qquad (2.3)$$

Where H(t) describes the scattered signal when the incident pulse $p_0(t)$ is so short that it can be described by the delta-function $\delta(t)$. H(t) can be determined by the acoustic properties of the elastic sphere and the distance between the acoustic source and the sphere so that the impulse response can be estimated.

In our simulation, the backscattering of a pulsed plane wave from an elastic sphere was modeled. Briefly, a plane wave was sent from 64 channels (delta-functions $\delta(t)$ sent from each channel simultaneously). A 2-mm radius COM stone was placed in water along the central axis of the transducer. The distance between the surface of the transducer and the center of the stone was 3 cm. To create a simple comparison to the experimental data, the time-step of the impulse response sampling was 50 ns, as it was the same as the sampling frequency used in the VUE. Since most of the kidney stones we dealt with are Calcium Oxalate Monohydrate (COM) stones, the acoustical parameters of COM stones were used in the simulations. After the simulation, simulated per-channel RF data was acquired and the beamformed channel data was obtained by employing the self-developed beamforming algorithms. The results of the simulation were compared to the results of experiments. The following parameters were used in the modeling:

a =2 mm (radius of the elastic sphere)

d =30 mm (distance from the probe to the sphere center)

h_t =50 ns (time-step for the impulse response sampling)

T =3.27675 ms (time window to define the impulse response, number of sampling points is T/ h_t =65536=2^{16})

ρ_{water}=1000 kg/m^3 (density of water)

c_{water} =1500 m/s (sound velocity of water)

ρ_{COM} = 2038 kg/m^3 (density of COM stone)

c_l = 4535 m/s (longitudinal velocity)

c_t = 2132 m/s (shear velocity)

d_{pitch}=0.3mm (the distance within two elements next to each other)
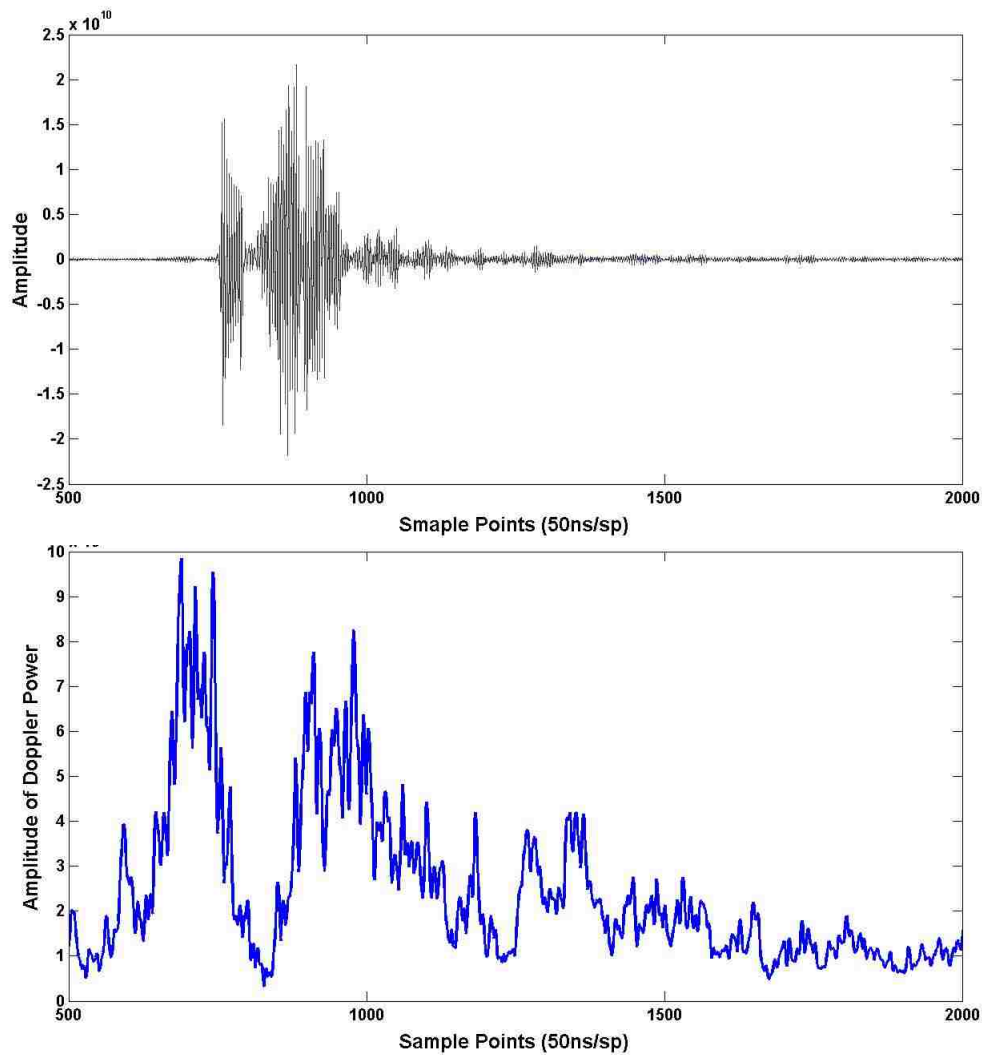
The convolution of the impulse response and incident Doppler ensemble (14 pulses within the ensemble) was calculated using Matlab. The incident Doppler ensemble was derived from experimental data obtained from the glass plate experiment. One pulse was chosen from the 14 pulses and duplicated several times to build a Doppler ensemble with identical pulses. Definitely, there is no

Doppler power peak shown within the Doppler ensemble. After this step, we obtained the unbeamformed RF channel data for 64 channels. Then the self-developed beamforming and Doppler processing algorithms were applied for the Doppler power estimation. Figure 2.30 shows from the simulation results that there is a peak in Doppler power curve after the surface reflection. However, there is also a peak shown ahead of the surface reflection. This finding shows that the TA should be observed before and underneath the surface of the stone, which is not the usual case. Therefore, stone ringing is not the main cause of the TA.

2.4 Discussions and Conclusion

In this chapter, the mechanism of the TA was investigated. Figure 2.31 shows the roadmap of this chapter.
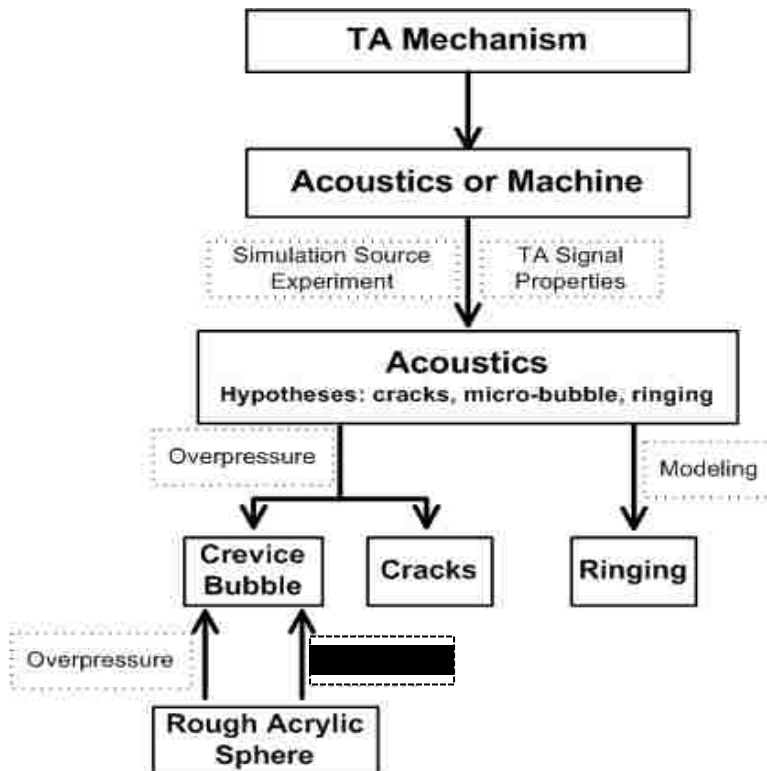
The TA has been known for over 15 years [6, 77]. It is an artifact since there is no stone motion observed during the TA. It is an unexplained artifact in Doppler ultrasound that appears distal to the echogenic surface and is especially apparent on stones in the kidney and ureter [7-10, 38, 52, 78]. Many clinical studies have proved that the TA could help enhance the sensitivity of stone detection by using ultrasound and suggest that this technique could be a potential sonographic feature for finding stones [7-10]; however, the underlining mechanism of the TA is still under debate, which prevents the adoption of the TA in clinical practice. There are many existing thoughts on the mechanism of the TA. Rahmouni et al. [5] thought that the TA resulted from the strong acoustic reflection from strongly reflecting media composed of individual reflectors. The strong reflections contain variability, which saturate the amplifier, thus the variability within the acoustic pulses were amplified nonlinearly and the broadband RF signals were created. On the other hand, Kamaya et al. [39] suggested that the fundamental reason for the presence of the TA is the 'phase jitter' from the internal machine clock, which could create fluctuations in the transmitting pulses and sampling signals; The irregular surface of strong reflectors play a secondary role to the broadening of the bandwidth of the variability resulting from the 'phase jitter'. However, both of the investigators did not really separate the effects of the acoustics from the machine.

In our investigations, the effects of the acoustics and the machine were separated by the simulated acoustic source experiment. The results showed that the receiving part of the machine was very stable since there was no twinkling artifact when using a stable simulated acoustical source. The stability of transmitting Doppler pulses was also examined by analyzing the Doppler ensemble RF data from the glass plate experiment. There was no variability introduced. The results showed that the influence of the machine was not the critical reason for the TA. At the same time, Sapozhnikov et al. [79-81] showed that

49

the acoustic radiation force may not be strong enough to create this artifact. The TA was described as rapid color alerting behind the strong reflective interface [7-10, 38, 52, 77-78] based on investigations on the color Doppler images provided by ultrasound machines. Our study has proved the phenomenon on a signal level. In the results, it showed clearly that the variability that is responsible for the TA comes slower than the reflection signal from the stone surface, while there is no comparable variability present within the reflection from the stone surface. Furthermore, the results proved that the appearance and magnitude of the variability do not depend on specular reflection. This varying signal works omni-directionally and arises from the inside of the stone. This finding suggests that the twinkling artifact is not simply due to the irregularity of the strong reflection surface as there would be a randomly changing source that introduces the noise-like variability into the Doppler ensemble. Several hypotheses about the mechanism of the twinkling artifact from the acoustic side, such as the micro-bubbles, the inhomogeneity of the stone (cracks), and the stone ringing were proposed.

The stone ringing was tested using modeling. The results showed that for an identical incident Doppler ensemble, stone ringing itself could introduce the variability. The estimated Doppler power demonstrated that if ringing was the main reason behind the twinkling artifact, the color should appear ahead of the stone surface and somewhere afterwards (as shown in figure 2.30), which was in part true based on our observations. While ringing could contribute to the TA, it may not the be the main reason for twinkling on kidney stones since the twinkling was shown only underneath the surface of the stone rather than ahead of it.

In order to test the microbubble hypothesis, the overpressure experiment was used since bubbles are very sensitive to pressure field changes. Following the pressure changes from the normal pressure to the high-pressure (up to 8.5 MPa) and then back to normal pressure, the twinkling disappeared under high-pressure and recovered after pressure was released. This result agrees with the potential

behavior of both the crevice bubbles (figure 2.20) and cracks. The internal structure of the stone is complicated, as shown in figure 2.32 and it is difficult to separate the effects of the crevice bubbles from the cracks on the human kidney stones. In order to separate the effects, the acrylic sphere was introduced as an experimental object because it was a uniform object without any cracks, and at the same time, we could introduce crevice bubbles easily. For the sake of testing whether the twinkling we introduced on the acrylic sphere was similar to the TA observed on the stone, the overpressure experiment was performed. The results showed that twinkling behaved in a similar way as was shown on the kidney stones.

For the acrylic sphere, there was nothing changed under overpressure except the crevice bubbles. This result shows that the crevice bubbles itself was enough to cause the TA. Another method other than overpressure was used to confirm whether the crevice bubbles were the mechanism of the TA. The crevice bubbles generally is caused by the imperfection of the wetting, so ethanol, a better wetting liquid than water, was introduced into the experiment. It showed that the TA was suppressed to some extent when ethanol was employed. This result confirms that the crevice bubble plays an important role in causing the twinkling artifact. The fresh stones experiment showed that the TA on stones with limited air contact was similar to that observed on old stones. Comparing the N% in figure 2.16 and 2.27, the N% on old stones was bigger than that on the fresh stones no matter under which pressure condition, i.e. before adding pressure, 17.3% vs. 9.1%; under high-pressure, 3.9% vs. 1.5%; After pressure was released, 14.5% vs. 7.4%. This result may confirm that the fresh stones have fewer bubbles than the old stones have. For the big picture, the fresh stone experiment confirmed what we found on the old stones. The knowledge obtained from the investigation of the TA mechanism on old stones can be applied to the *in vivo* kidney stone detection. Last but not least, the TA always showed behind the surface of the stone, which is confirmed by the TA RF signal analysis (figure

51

2.7). The explanation to this phenomenon could be that, the number of crevice bubbles within the interaction area was not enough to cause the TA. The surface waves, which transmit slower than the reflection and travels as part of the stone surface, could collect variability from more crevice bubbles and cause the TA.

Is there any explanation of why bubbles are trapped in the crevices of the kidney stone? The stone consists of proteins and crystals. One hypothesis is that some hydrophobic spots (proteins or something else) on the stone may trap gas and form the crevice bubbles. On this, we need to be clear that crevice bubbles are extremely small (maybe <10 µm) such that they cannot be seen under CT. Further tests need to be done to identify crevice bubbles and how they are formed. Better understanding of the mechanism of crevice bubble formation is significantly important for improvements to, and future clinical applications of, the TA.

In this chapter, the conclusion that crevice bubbles are the main mechanism of the TA was drawn based on the *in vitro* and *ex vivo* stones tested. For clinical practice, it will be more complicated, i.e. we still cannot exclude cracks as a mechanism since they behave similarly to crevice bubbles. Crevice bubbles would not be the only reason for the TA.

Chapter 3

Improved ultrasound technologies for kidney stone detection

3.1 Introduction

The 1st international Consultation on Stone Disease in Paris (2003) states that reduction of the radiation exposure related with spiral CT and the development of office-based diagnostic techniques would be the areas of greatest gain in stone localization [30]. Current ultrasound imaging technologies meet these goals; however, there is room for improvement as it is difficult to localize kidney stones with ultrasound due to the low sensitivity.

The TA is a color Doppler ultrasound imaging technique that is non-ionizing, inexpensive, and non-invasive that can image in real-time with high accuracy for stone detection. Many studies have reported that the TA has great potential for kidney stone detection and localization; [6-10, 51-52] however, the artifact is unstable. With the unknown mechanism of the TA, it is difficult to optimize the TA for stone detection. So, the acceptance of the TA for clinical use is impeded.

Color flow imaging, which shows the TA, has been steadily developed for clinical blood flow imaging. Some investigators have tried to test all of the imaging parameters and settings within the color Doppler imaging system to provide an optimal technique for stone detection with twinkling; however, the vast difference in the acoustic properties between kidney stones and blood flow in addition to the limited access to the image processing algorithms of the ultrasound machines makes it difficult to optimize the TA for kidney stone detection.

In this chapter, a modified ultrasound color Doppler imaging algorithm for specialized kidney stone detection is proposed based on the difference in acoustic properties between kidney stones and blood flow. Two new image processing algorithms have been developed based on our understanding of the mechanism and signal properties of the TA. Simulations of the new imaging

algorithms have been completed using the RF data obtained from *in vitro* phantoms and *in vivo* porcine experiments. Comparisons were made between the results from the classic TA and the new imaging algorithms.

3.2 Methods

In this section, the signal path of color flow Doppler ultrasound imaging is described. Then, the effects of different transmitting and imaging parameters (*i.e.*, pulse lengths, Doppler ensemble lengths, pulse repetition frequencies (PRF), Doppler transmitting powers, and time gain compensation (TGC)) on the TA were tested and compared. Based on the results, several new imaging methods (new TA, AMP and variance modes), were developed for kidney stone detection. Stone highlighting by the classic TA, the new TA, the variance, and the AMP modes was compared by a calculation of N%. One-way analysis of variance (ANOVA) was applied to determine whether there is statistical significance in the stone detection ability among these imaging algorithms. The hypothesis was rejected on a 0.05 level.

3.2.1 Color Doppler image – general layout

The general layout of a color Doppler imaging system on the VUE is shown in figure 3.1(the details may be different depending on the machine). After the digitizer, the RF data are sent to the beam-former. Then, quadrature demodulation is performed by multiplying the beamformed RF signals with quadrature signals of the same central frequency to generate the complex I/Q data containing both the amplitude and phase information of the original signal. Next, the I/Q data are sent to the wall-filter to remove the low frequency, high-amplitude components and then processed to estimate the Doppler power, mean frequency, velocity, and bandwidth of the Doppler signal. All estimations are stored in the memory as a frame, which can be spatially and temporally averaged before it is sent out for color encoding. Besides Doppler RF data, the VUE also

provides the B-mode RF data at the same time, which are processed to build a grey-scale image. Then, the grey-scale information and the color Doppler information are combined to judge whether blood flow is present. From these combined results, an appropriate grey or color pixel is encoded into the display memory and shown on the screen. Each component within the color flow Doppler imaging system is described in Appendix B.
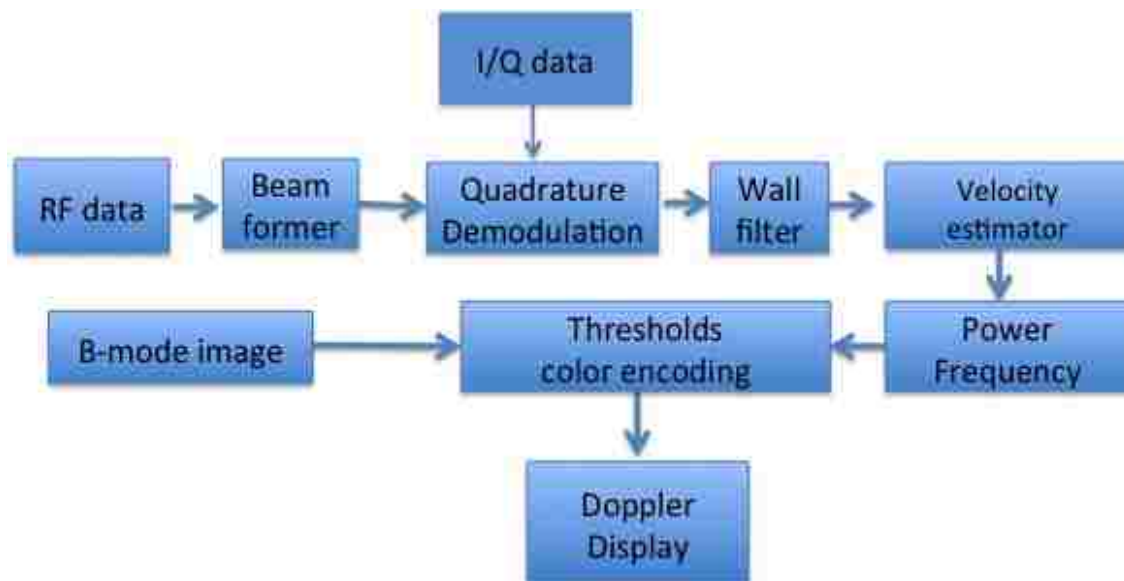
3.2.2. New color Doppler imaging - Stone Specialized Modifications

Since the acoustical properties of kidney stones are different from those of blood flow, components that have been especially designed to detect blood flow should be modified to specialize in kidney stone detection. In this section, the components of traditional color flow Doppler are analyzed and modifications for improved stone detection are presented.

a) Wall-filter

The wall-filter used by the VUE is a 2nd order (quadratic based) regression filter, because this filter works best for the short ensemble lengths detected by the

VUE (under 16 pulses within the ensemble). The basic reasoning behind the regression filter is that the low-frequency (typically, lower than 1 kHz) clutter signal within the Doppler ensemble could be approximated by a low order polynomial, which can be estimated by employing the least-squares regression analysis [82]. Figure 3.2 shows the Doppler power response of the regression filter with different orders. The RF data used in the calculation is obtained from an *in vitro* phantom experiment. The power response is calculated by the equation:

$$PR_{dB} = 10log_{10}(\frac{P_i}{P_0}) \tag{3.1}$$

Where i = 1,2,3…7; P_0 is the averaged Doppler power of Doppler signals filtered by 0th order regression filter; and P_i is the averaged Doppler power of Doppler signals filtered by i^{th} order regression filter. Each P_i is averaged over 40 frames. In theory, the higher the order of the regression filter, the more the frequency components are cut. Figure 3.2 demonstrates that, as the filter order increases, the Doppler power response decreases. Even for the case with a 7th order regression filter, the Doppler power response is only -6 dB with a signal to noise ratio that is still bigger than 2 (results not shown). The TA signals should be broadband signals rather than signals with a certain frequency. In order to keep as much twinkling information as possible, we should use the regression filter with the order as low as possible, making a 1st or 2nd order regression filter the best choice.

b) Thresholds and color priority encoding

In the velocity estimator, the average Doppler power, velocity, and frequency shift are estimated. The thresholds that determine whether to display grey-scale or color for certain pixels are very important. Therefore, modifications to the thresholds are critical for specialized stone detection. As usual, the thresholds differ from machine to machine, but there are some common themes.
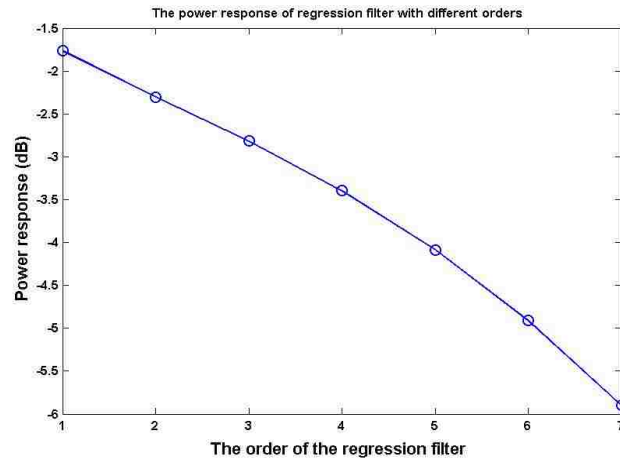
Figure 3.2 The power response of the regression filter with different orders.

i) Velocity threshold

If the velocity calculated from autocorrelation is too slow, the Doppler spectrum is more likely to be dominated by clutter signals leaked through the wall-filter rather than blood flow signals. If the calculated velocity is lower than a certain velocity threshold, gray-scale information will be displayed on the screen. Figure 3.3 shows the images of the TA, blood flow, and the color map used in a color flow imaging system. In Figure 3.3 A, the TA is highlighted by the yellow and light blue color. The color map demonstrates that those colors represent the high velocities. In Figure 3.3 B and C, there are blood flows in opposite directions. The colors representing blood flow are darker than those representing the TA, which means that the machine detects faster motion in the TA area than in the blood flow. This leads to the conclusion that there is no need to modify the velocity threshold to select for stone detection over blood flow.

ii) Maximum echo intensity threshold (brightness threshold)

The echo intensity threshold is named here as the 'brightness threshold'. If the amplitude of gray-scale echoes (B-mode signals) is very strong, the possibility of this signal being related to clutter is much larger than the probability of being the signal being related to blood flow. Therefore, grey-scale information will be encoded on that sample volume.

The stone is a good reflector, thus we need to set the brightness threshold to withdraw signals that give weak echoes. In other words, when one sample volume shows a big Doppler power, the brightness threshold will check whether the strength of the echoes from the sample area is also strong. If it is stronger than a certain threshold, there is a big possibility that this sample volume is located on the stone, thus color information will be encoded on the sample volume.
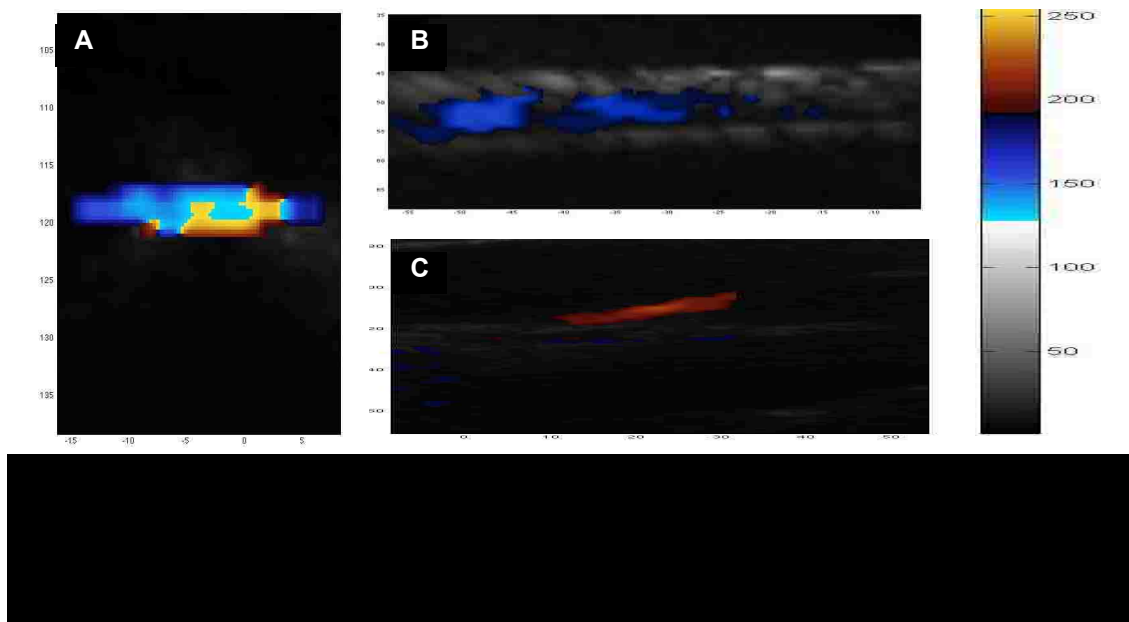
iii) The Doppler bandwidth threshold

The basic idea of this threshold is that the bandwidth of the Doppler signal from blood flow should be relatively narrow while the bandwidth of the background noise should be very broad. If the estimated variance of the Doppler power

spectrum exceeds a certain value, the velocity signal is assumed to be invalid. The bandwidth of the Doppler signal from the TA is contrary to that from blood flow. Therefore, it is appropriate to invalidate this filter to let all signals pass through.

In summary, to select for stone detection over blood flow, the modified color Doppler imaging algorithm should contain: a regression wall-filter with a low order; a Doppler power magnitude threshold to reject signals with low Doppler power; and a brightness threshold to reject signals with weak grey-scale echoes. The other parts in the normal color Doppler imaging system do not change to select for stone detection.

3.2.3. Modification and Optimization of Technical Parameters

The properties of the transmitting pulses depend on the settings of machine (*i.e.*, transmitting power, pulse repetition frequency (PRF), pulse length, Doppler ensemble length, incident angle, transmittance type, etc.) On the receiving side, TGC is usually involved and may affect the TA. A quantitative comparison of the effects of the technical parameters listed above on the TA was performed based on the analysis of the RF data.   In this section, we used plane wave, flash mode to send the pulse, setting the incident angle as zero degrees for ease of processing. The results from modifying these parameters are presented in the experimental section.

a) The pulse length

Normally, when using a longer pulse, the spatial resolution decreases, the bandwidth of the transmitting pulse decreases, and the total transmitting energy increases. Varying the pulse length may affect the TA. This hypothesis was tested on an *in vitro* gel phantom with implanted human kidneys.

b) The ensemble length

The ensemble length is critical for the detection of blood flow as blood flow is a continuously changing phenomenon. Each color Doppler pulse is too short to provide an acceptable averaging value. However, the longer the ensemble is, the higher the sensitivity of slow velocity detection, but the slower the frame rate. For the TA, as shown in figure 3.3, the estimated velocity is high, which means that the ensemble length does not need to be long. Different ensemble lengths were tested in *in vitro* gel phantoms.

c) The PRF

The Nyquist frequency theory states that the sampling frequency should be at least twice the highest frequency in the signal to avoid aliasing. Based on this theory, the maximum Doppler frequency shift that can be detected using color Doppler ultrasound is half of the PRF. Therefore, the maximum detectable velocity without any aliasing can be calculated as:

$$V_{max} = f_s c / (4 f_t \cos \theta) \qquad (3.2)$$

Where f_s is the PRF; c is the sound velocity; f_t is the transmission frequency; and θ is the angle between blood flow and the acoustic transmittance angle. The higher the PRF is, the wider the range of the estimated velocity, which can be seen in the image.

d) The transmitting Doppler power

As discussed in Chapter 2, the TA signal has amplitudes of the wall-filtered Doppler signals that behave randomly, which means the power would change nonlinearly following the change in amplitude. The effects of changing the transmitting power on the TA will be tested on an *in vitro* phantom. In the VUE, the transmitting Doppler powers can be adjusted by adjusting the Transmit Power Controller (TPC). Its range is 1 to ~35 volts, which is set using the High Voltage slider object on the VUE GUI window. In the following sections, we will

use the change in the High Voltage supply (the peak voltage applied on the transmitters, unit Volts) to indicate the change in the transmitting Doppler power.

e) The Time Gain Compensation (TGC)

TGC is generally used on the receiving side to enhance weak signals. For color Doppler ultrasound, TGC is always involved since the color Doppler signals are usually not strong. Whether the TGC affects the TA more than an amplifier and how the TGC helps emphasize the TA were investigated in an *in vitro* phantom..

3.2.4 New Stone Detection Algorithms

Based on what we have learned on the mechanism and signal properties of the TA, new stone detection methods have been developed.
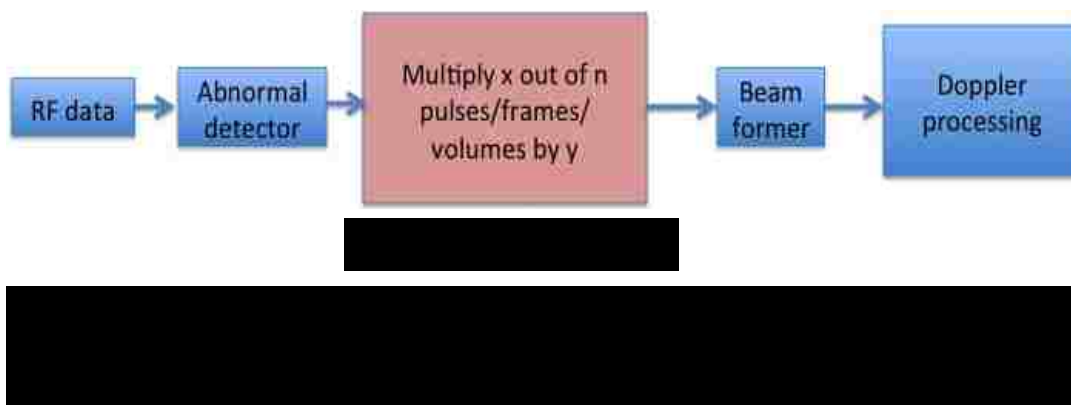
a) AMP algorithm

During the investigation into the mechanism of the TA, we observed that among multiple wall-filtered Doppler pulses, one or several of them is/are abnormal from the others. The results were reported in section 2.3.2. What if we enhance this abnormality? Figure 3.4 shows the flowchart of the modification. Since the amplification feature of the modification, this feature is named as the AMP algorithm.

Compared to the normal color flow Doppler imaging system, one new unit or step is introduced between RF collection and the beam-former. During the step, the abnormal event is estimated and the order of the abnormal pulse(s) is recorded. The x number of pulses/frames/volumes are multiplied by a coefficient y. Usually, x equals 1 and y equals 1.01 to 1.10, depending on the signal strength. Simulations on RF data obtained from porcine experiments *in vivo* and human
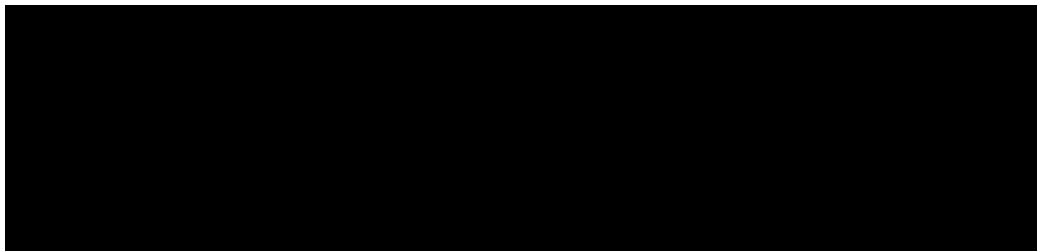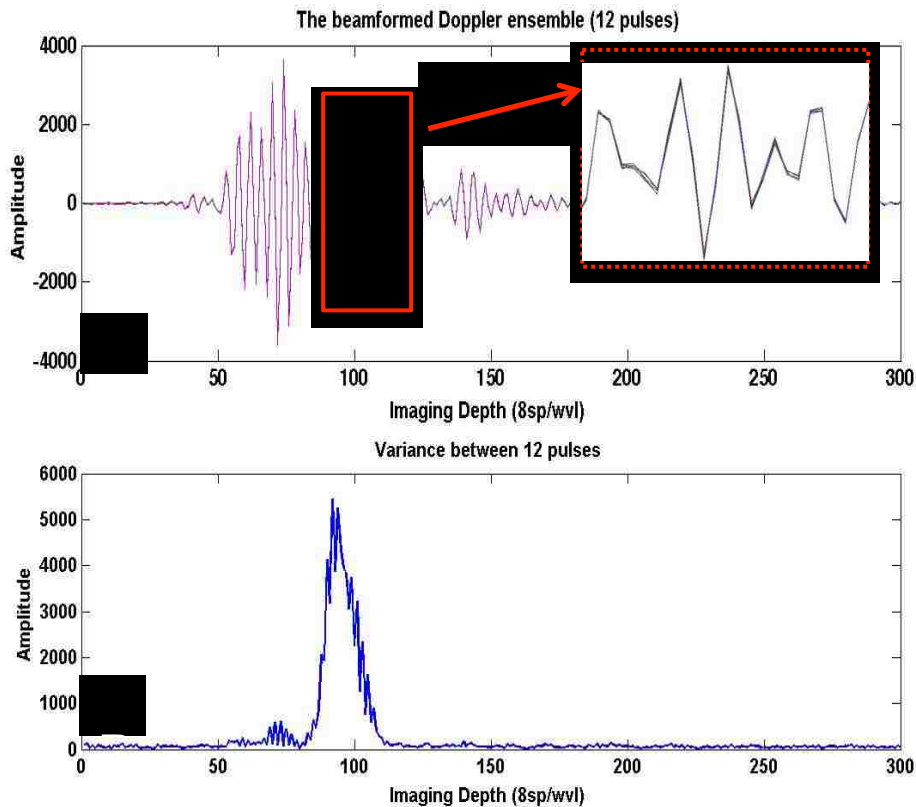
kidney stones *in vitro* have been completed. Results are shown in the experiment and results section.

b) Variance algorithm

During the investigation into the TA, it was observed that the signals that correspond to the TA usually appear noisier than the other parts of the signals being reflected from the stones (figure 3.5). This kind of noise usually corresponds to a big variance within the Doppler pulses. The variance is used to describe how far several numbers are spread out from each other. It can be
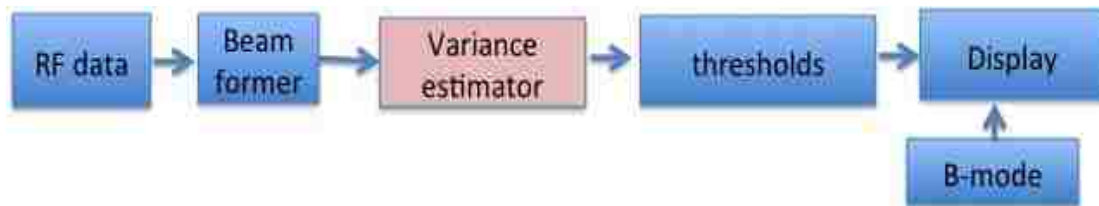
calculated as follows: $Var(X) = \sum_{i=1}^{n}(x_i - \mu)^2$, where X is the dataset that will be analyzed; x_i is the ith number in X; and μ is the expected value of X.

The flowchart of the variance mode is shown in figure 3.6. After going through the beam-former, the Doppler signals are sent to the variance estimator to calculate the variance between the Doppler pulses. The variance information is stored in a color frame memory. After that, the variance information and grey-scale information are combined to determine whether the sample volume is on the stone or not. Several thresholds are employed to determine whether the sample volume is encoding variance information or grey-scale information.

3.3 Experiments and Results

3.3.1 Technical parameter tests

a) Different pulse lengths

Five human kidney stones (6-10 mm in length and 4-8 mm in width) were scanned in the polyacrylamide gel phantom. Doppler pulses were sent in flash mode with a 0 degree incident angle. The PRF was 3 kHz and the peak voltage applied to the transmitters was 35 V. Normal color Doppler imaging was

employed and a Doppler ensemble length of 14 pulses was used. Different pulse lengths were applied in the scanning with the Doppler pulse length ranging from 1 to 10 cycles. The RF data were collected where it was found that the TA was not stable (not shown on all frames) in the two locations per stone that were imaged. The VUE could save 20 frames per scan when collecting the RF data, so for each location and each pulse length, 40 frames were saved. In total, the RF data from 2400 frames were analyzed and the Doppler power from the scan line that showed the TA was calculated on each frame. Then, the mean Doppler power for each location per pulse length was averaged from the 40 frames. The mean and standard deviation of the Doppler power of each pulse length was calculated from the Doppler powers of a pre-defined pulse length from all three stones. The pulse duration at 3 dB of the Doppler power curve was also estimated for each pulse length recognizing that longer pulses would introduce more energy into the system. In order to make the results comparable, the Doppler power was normalized under different pulse lengths.

Normalized peak Doppler power for different pulse length

The Doppler power peak duration under different pulse length
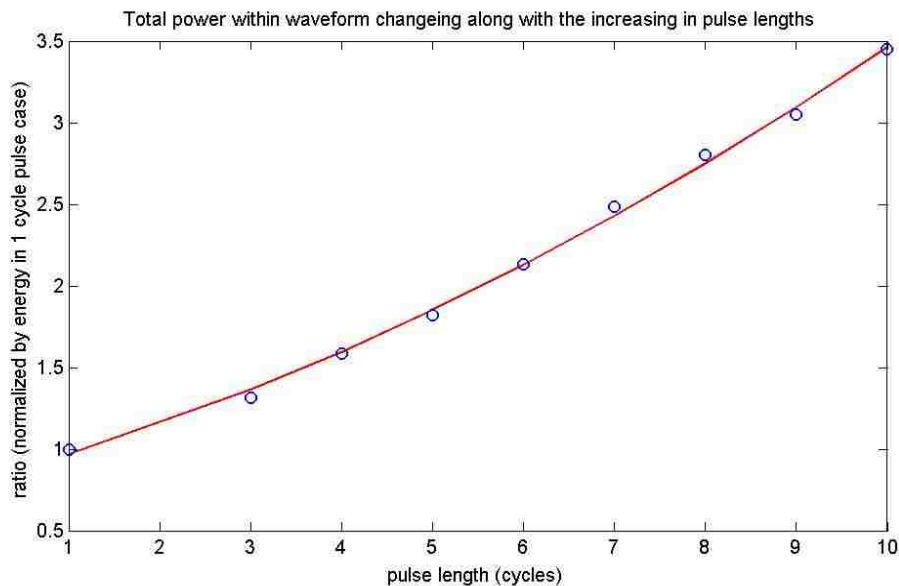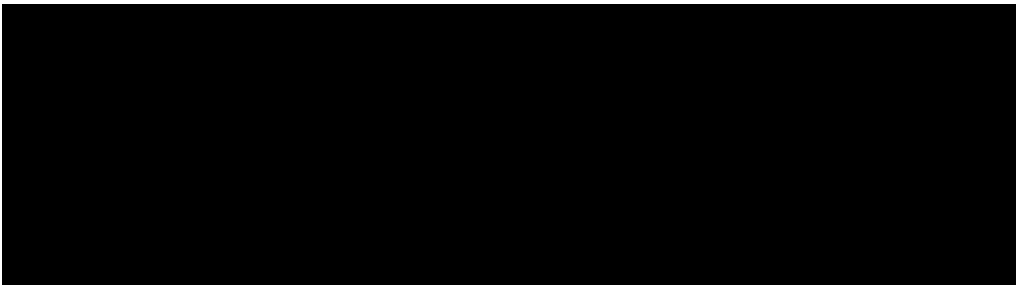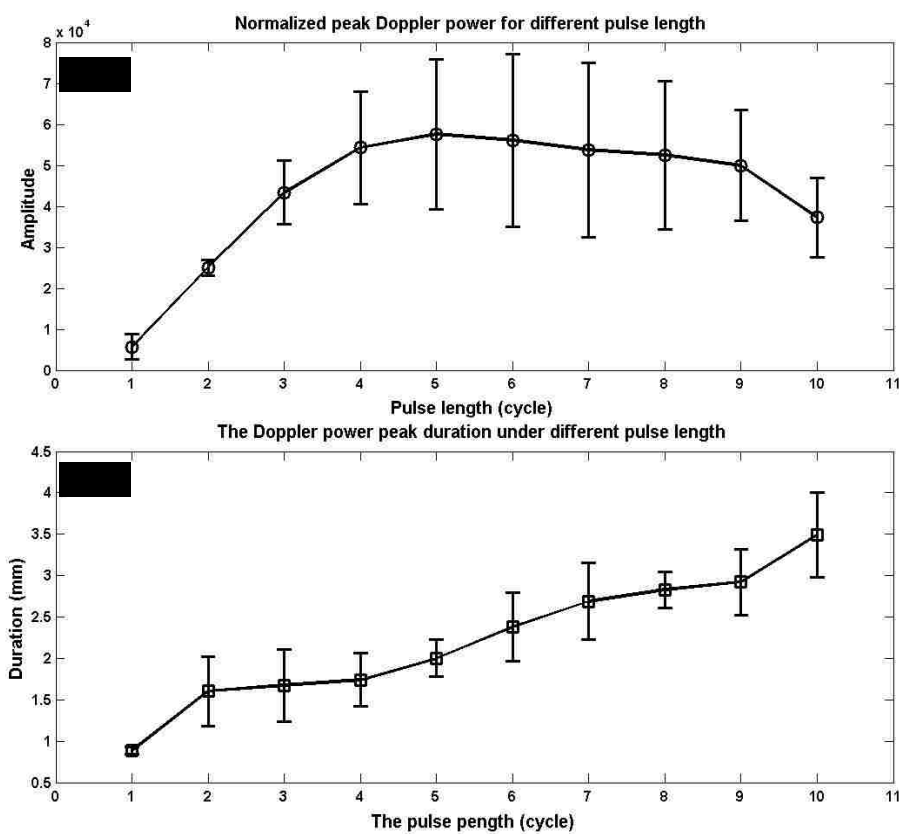
A glass plate experiment was applied to estimate the total incident power of the transmitting pulses. In the experiment, a glass plate (15cm X 7.5cm X 1.68cm) was placed vertically with respect to the transducer. The transducer (L7-4) was fixed on a ring clamp. A tank of water was degassed so that the oxygen

saturation was lower than 20%. The length of pulse was changed in the sequence from 1 to 10 and then, from 10 to 1 by changing the Matlab® script. For each case, the RF data were recorded and the intensity (energy) was calculated for each pulse length by summing the square of the amplitude for each point on the waveform. The energy was normalized by dividing the energy of each pulse length by the energy in 1 cycle. The ratios (shown in figure 3.7) were recorded and used to normalize the Doppler power from stones. The normalized Doppler power from the stone imaging and the pulse duration of the Doppler power curve in fast time are shown in figure 3.8.
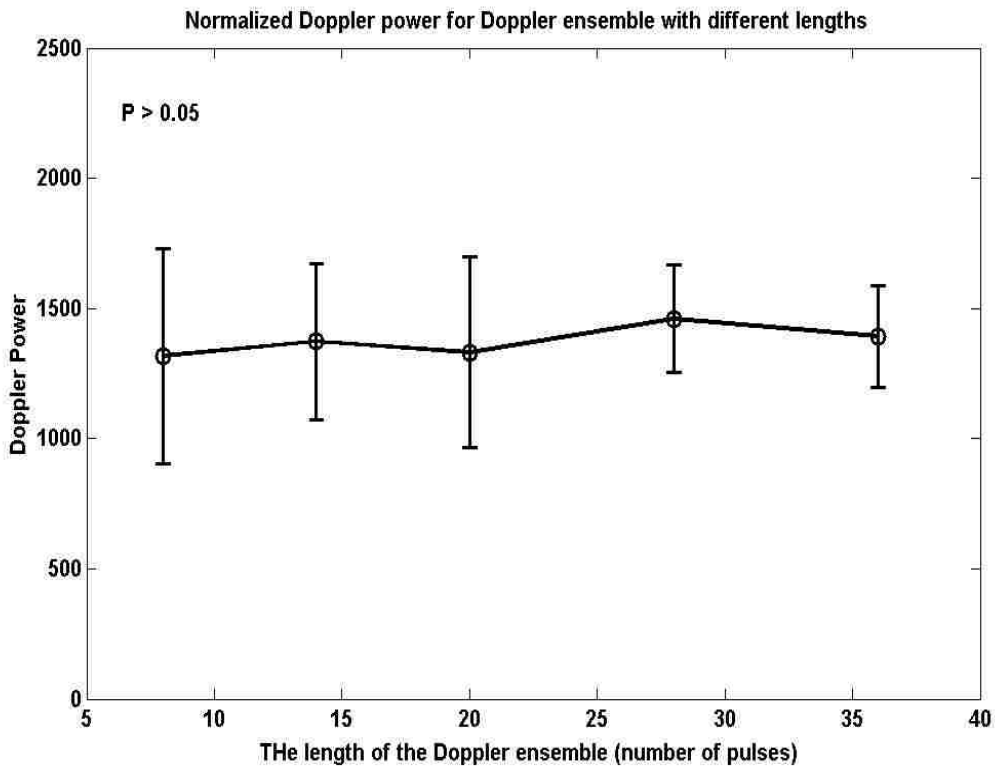
In figure 3.8 A the normalized Doppler power increased as the pulse length increased from 1 to 5 cycles. Then there was a minor drop in the magnitude of

66

the Doppler power when the pulse length changed from 5 to 10 cycles. The default setting of the pulse length in the VUE is 3 cycles for color Doppler imaging. In figure 3.8 A, the longer pulse, within which the number of cycles was bigger than 3, could induce higher Doppler power. However, the pulse should not be too long since there is a Doppler power drop after 5 cycles. Figure 3.8 B shows changes in the pulse duration at 3 dB of the Doppler power under different pulse lengths. The square marker shows the mean value of the pulse duration under different pulse lengths from 240 frames. As the pulse length increased from 1 to 10 cycles, the pulse duration incresed. The pulse duration from the 10 cycle transmitting pulse is 2.5 times as big as that when the 1 cycle transmitting pulse was applied.

b) Different ensemble lengths

In this section, the effects of different Doppler ensemble lengths on the TA were investigated. Six human kidney stones (6-12 mm in length and 4-8 mm in width) were scanned in the polyacrylamide gel phantom. The setup was the same as described previously with the pulse length set to the default 3 cycles. The ensemble lengths of: 8, 14, 20, 28, and 36 were applied. One scan line, which had the TA for all Doppler ensemble length cases, was chosen and the Doppler power for the scan line was calculated under each Doppler length case for each frame. The maximum peak values of the Doppler power were normalized for the different lengths of Doppler ensembles. The mean value and corresponding standard deviation were calculated for 40 frames under each Doppler ensemble length. A statistical analysis was applied on these 5 groups of Doppler power by using a one-way analysis of variance, which is widely used in analyzing the statistical significance of means within different samples that contain mutually independent observations. The hypothesis was rejected on the 0.05 level. Figure 3.9 shows that there is no statistically significant difference between Doppler lengths ($p>0.05$).

c) The PRF

In this section, the influences of different PRFs on the TA were investigated. Six human kidney stones (6-12 mm in length and 4-8 mm in width) were scanned with all stones glued on needles and fixed in the stone holder. The experimental setup was the same as shown in figure 2.23. The machine settings were the same as described previously with the PRFs tested being 1 to 10 kHz with a 1 kHz step. Three frames were randomly chosen out of 20 frames per stone for the investigation. The maximum Doppler power of the twinkling and N% that was defined in Chapter 2 to describe how well the stone was lt by color were estimated for all PRF cases. The color pixel was chosen based on the comparison of the Doppler power of certain pixels, with the noise level as determined by the mean Doppler power of the image. If the Doppler power was 3 dB stronger than the noise level, the color pixel was counted. One-way analysis of variance was used for the statistical analysis. The hypothesis was rejected at the 0.05 level. The results are shown in figures 3.10 and 3.11.
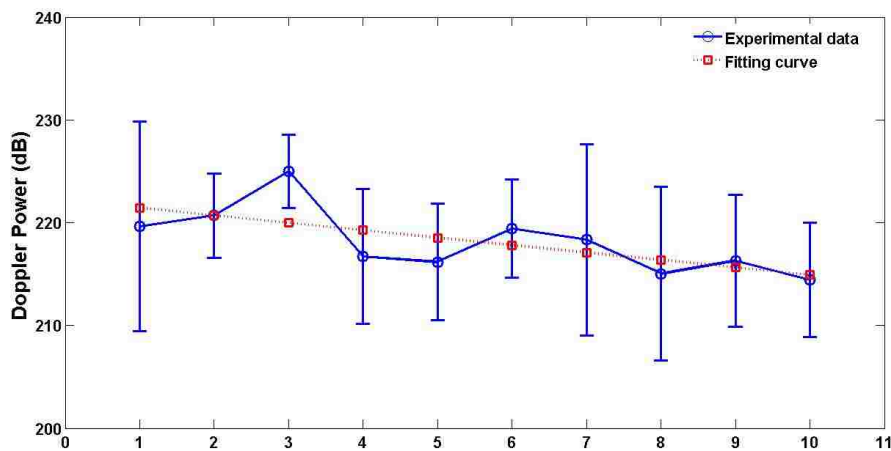
In figure 3.10, the fitted curve is almost a straight line and shows the peak Doppler power decreasing with increasing PRF. The noise level for all PRFs is 191.42 ± 0.06 (dB). The difference between the Doppler power under 1 kHz and 10 kHz is approximately 7 dB, which shows that the signal to noise ratio became higher with the decrease in PRF. However, the statistical analysis shows that there is no statistically significant difference between mean peak Doppler powers among all PRFs.
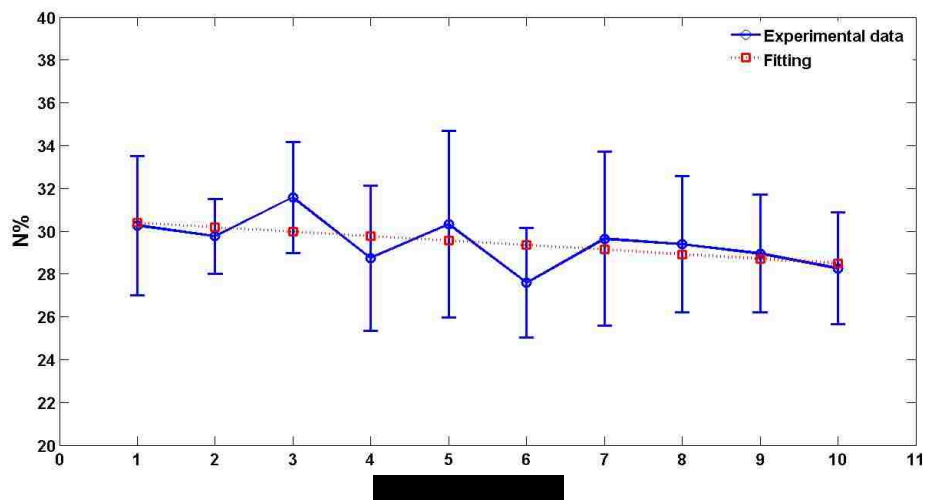
In figure 3.11, the area that was highlighted by color decreases linearly as the PRF increases, as shown by the red dashed line with square markers. The biggest difference was the difference in N% of 1 kHz and 10 kHz, which was 1.8%. The p-value of the mean N% was << 0.05 among all PRF cases. The results show that at least one mean of N% is statistically different from the others. The maximum frequency shifts were also calculated for the twinkling areas for different PRFs. Based on these data, the velocities that correspond to the twinkling spots were estimated. In figure 3.12, the estimated maximum velocity from the experimental data agrees with those calculated from the Doppler theory.

The estimated maximum velocity increases linearly with increasing PRF and are very close to the theoretical results.
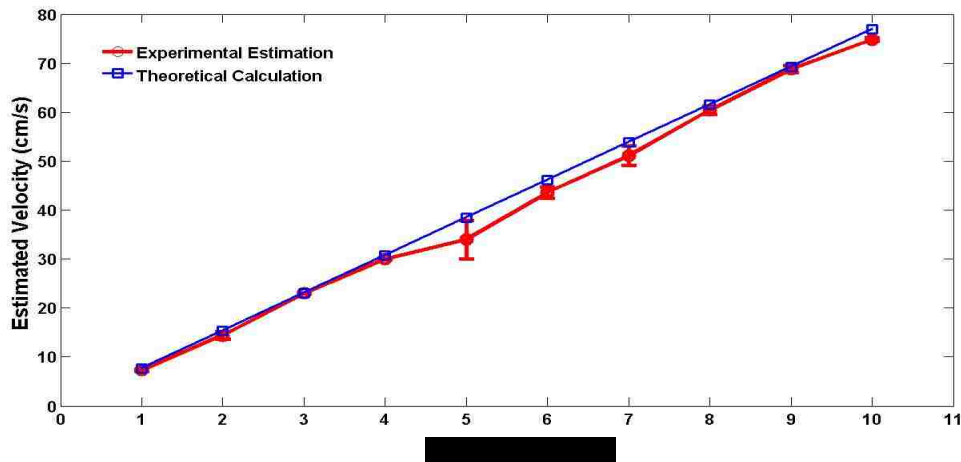
d) Transmitting Doppler Power

The experimental setup, objects, and parameters are the same as those used in PRF tests except the PRF was fixed at 3 kHz and the transmitting powers varied. Six transmitting Doppler powers, which were generated by applying peak voltages (1.6 V, 10 V, 20 V, 30 V, 35 V, 36 V) on the transmitters, were tested in the experiments. Three frames were randomly chosen out of 20 frames per stone for the investigation. The maximum Doppler power of the twinkling and N% were estimated for all transmitting powers. The results are shown in figures 3.13 and 3.14. For convenience, the change in the transmitting Doppler power is indicated by the change in the applied peak voltages.
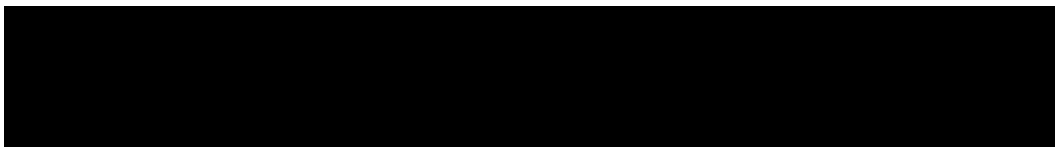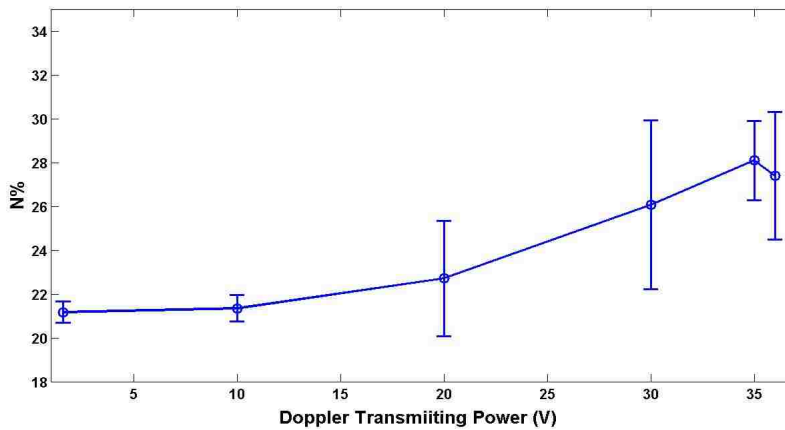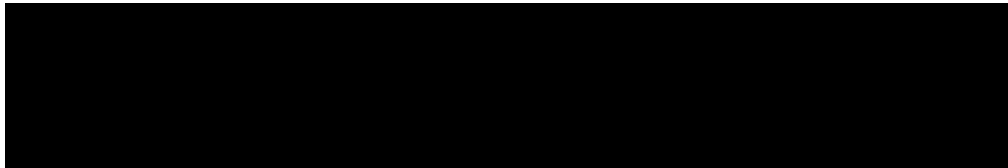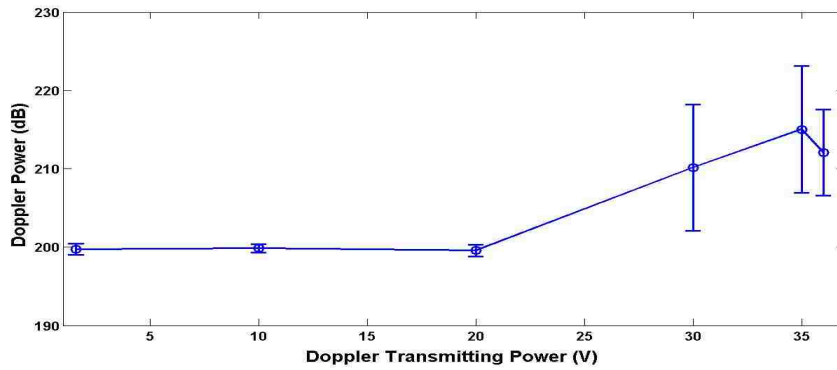
In figure 3.13, as the Doppler transmitting power increases, the peak Doppler power in the twinkling area was stable and the variance of the peak Doppler power was relatively small up to 20 V. After 20 V, there was a sharp enhancement of the peak Doppler power in the twinkling area, and the variance of the peak Doppler power was relatively large. When the peak voltage reached 36 V, the maximum transmitting power of the VUE for the color Doppler mode,

there was a small decrease in the peak Doppler power compared to the peak powers below 35 V. The p-value of the mean of the peak Doppler power under different transmitting powers was >>0.05. There was no statistical significance among the mean of the peak Doppler powers for all transmitting powers.

In figure 3.14, the N% increases as the transmitting power increases. At the very beginning, from 1.6 V to 10 V, the change in N% is very small (0.18%) compared to that of other ranges, such as 10 V to 20 V (1.37%), 20 V to 30 V (3.4%) and 30 V to 35 V (2.0%). Generally, the change in the N% agreed with the results from he last section in that the stronger the transmitting power, the larger the N%. Again, there is no statistical significance within the means of the N% among all transmitting Doppler powers.

e) TGC

For the VUE, the TGC waveform is used with the receive specifications. Eight control values that represent the gain at increasing depth in the acquisition period are used to construct a TGC curve. The amplificatory range of the TGC is 60dB. Several TGC levels, such as 0 dB, 12 dB, 24 dB, 36 dB, 48 dB, and 60 dB, were chosen for the tests. The other values remained the same as were used in all previous experiments and the experimental setup was the same as was used in the PRF tests. The peak Doppler power and the N% were estimated for each TGC case and compared for all TGCs. The results are shown in figures 3.15 and 3.16.

In figure 3.15, the tendency for a change in the peak Doppler power of the twinkling area with increasing TGC is shown using a blue solid line and its fit curve is shown in a red dotted line, which is $y = -0.0010x^3 + 0.0892x^2 - 0.6365x + 215.1291$. The peak Doppler power increases with increasing TGC. From 0 dB to 12 dB, the enhancement is around 3 dB, which is smaller than the 12 dB increase in the TGC; from 12 dB to 48 dB, the increase in the Doppler power ascends linearly with the increase in TGC.
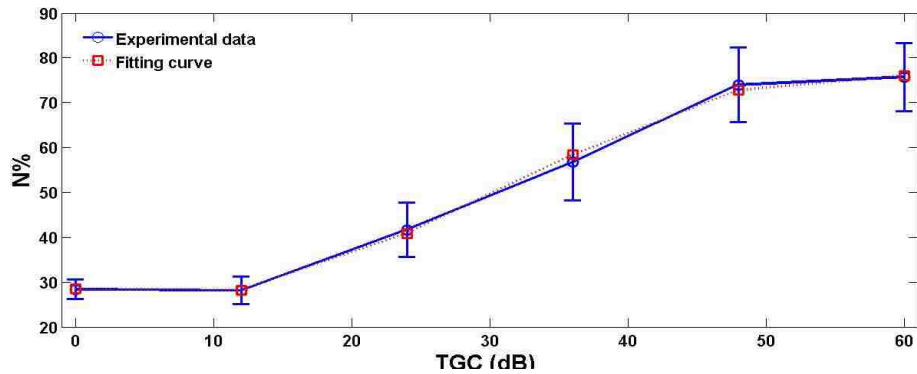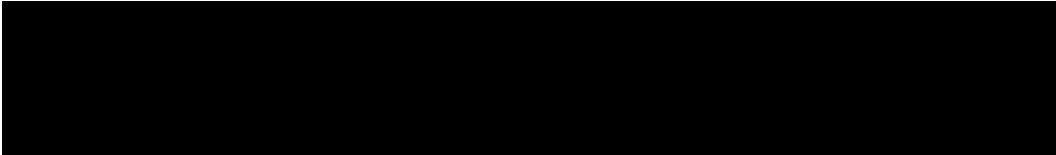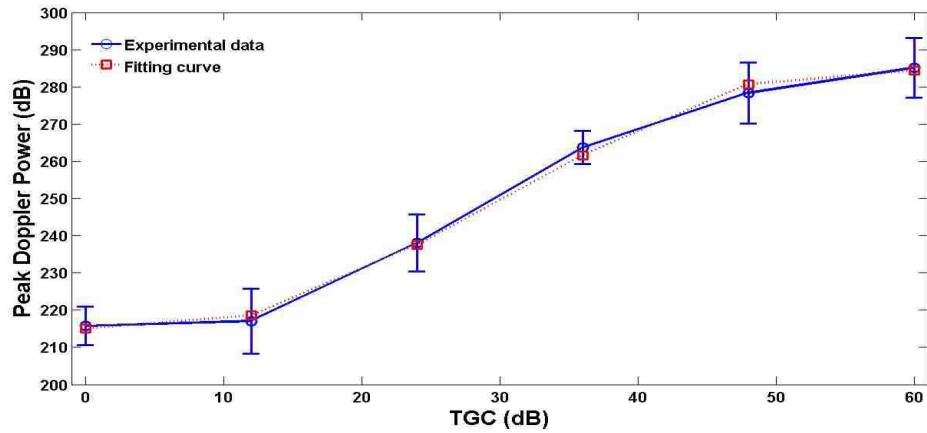
In addition, there is a 18.93 dB, 24.11 dB and 19.04 dB enhancement of the Doppler power as the TGC increases from 12 dB to 24 dB, 24 dB to 36 dB and 36 dB to 48 dB, respectively. From 48 dB to 60 dB, the grading of the Doppler power is 3.7 dB, which is much smaller than the 12 dB enhancements in the TGC. The p-value of the mean peak Doppler power is >> 0.05, thus there is no

statistical significance among the mean peak Doppler powers among all TGCs. For the big picture, the total enhancement of the Doppler power from 0 dB to 60 dB is 69 dB, which is 9 dB stronger than that of the TGC. The variances in the peak Doppler power under different TGCs are similar.

In figure 3.16, the tendency of the change in N%, the color occupied area, with increases in the TGC are shown using blue solid lines with its fitting curve shown as a red dotted line, which is $y = -0.008x^3 + 0.0729x^2 - 0.7881x + 28.47$. The N% increases with the increase in the TGC. The tendency is similar to the change of the peak Doppler power following the increase in the TGC. From 0 dB to 12 dB, the enlargement of the color area is negligible; from 12 dB to 48 dB, the increase in the color area ascends linearly with the increase in the TGC. Comparing to the previous color area in the sequence, there is 12.64%, 17.55% and 14.43% enlargement from a TGC increase of 12 dB to 24 dB, 24 dB to 36 dB and 36 dB to 48 dB, respectively. From 48 dB to 60 dB, the color area is 3.3% larger.

So far, the effects of several technical parameters were tested quantitatively based on the RF data analysis. The results show that the pulse length, Doppler ensemble length and the PRF has weaker effects on the TA than that of the transmitting Doppler power and the TGC. For the optimization of the parameters, on one hand, some tradeoff should be made to adjust the balance between the SNR and the color area on the image, i.e. the modulation of the pulse length, ensemble length and PRF; on the other hand, as long as the noise can be differentiated from the TA in the clinical practice, the transmitting power and the TGC should be set to as high as possible.

3.3.2. New Stone Detection Algorithms

a) AMP algorithm

1) *In vitro* phantom simulation

Several human kidney stones (5-10 mm in length, 3-8 mm in width) were implanted into a porcine kidney. The phantom was prepared the same as described in chapter 2. Doppler pulses were sent in flash mode with a 0 degree incident angle. The PRF was 3 kHz and the voltage supplied on the transmitters was 1.6 V. Normal color Doppler imaging was employed and the Doppler ensemble containing 14 pulses was used. The TGC was set as default. Images from AMP mode and classic TA were compared.
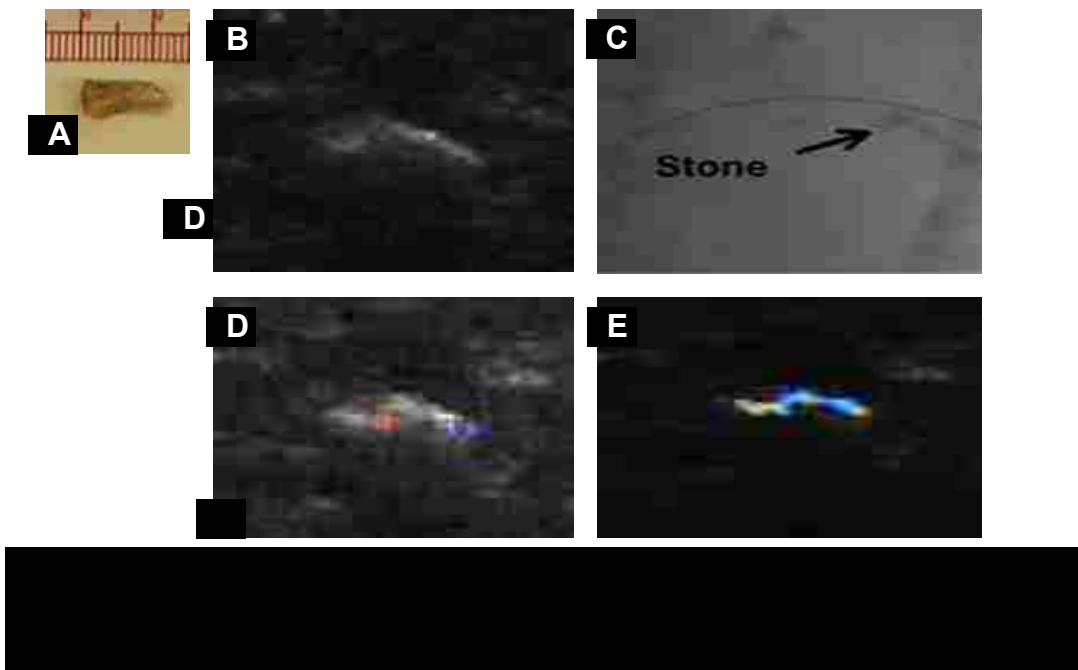
Figure 3.17A shows the photo of the human stone used in the experiment. B is the B-mode image of the stone in porcine kidney and C is the fluoroscopic image of the same stone in porcine kidney. D is the normal color Doppler image of the stone and E is the image generated using the AMP algorithm in the processing data mode of the VUE. Either on the B-mode ultrasound or the fluoroscopic images, the stone was not shown well. Applying the classic TA, there were some twinkling spots showing on the stone surface; however, they only showed the possible location of the stone. Using the new AMP stone detection algorithm, the

stone is emphasized by bright color. Not only the location of the stone but also the size of the stone were highlighted very well.

2) *In vivo* porcine data simulation

Several human kidney stones (5-10 mm in length, 4-8 mm in width) were implanted into a porcine kidney. The transducer C4-2 (ATL/Philips, f_c = 3MHz) was used in the *in vivo* experiment. The B-mode and normal color Doppler imaging methods were applied and the fluoroscopic imaging was obtained using C-arm fluoroscopy (OEC 9800 GE healthcare). The RF data were collected and processed by the AMP algorithm. The newly generated RF data were sent back to the VUE simulator to get simulation results.
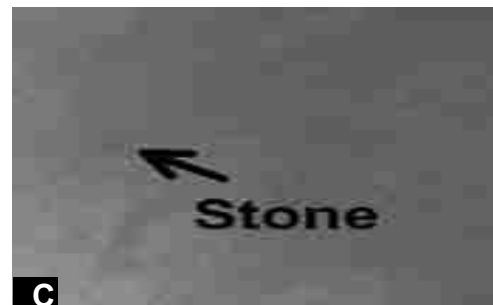
Figure 3.18 A shows the photo of the stone used in the experiment, figures B to D show the B-mode, fluoroscopic and normal color Doppler images, respectively. Figure E shows the image obtained using AMP algorithm. From the B-mode and fluoroscopic images, the stone is hardly seen. For the image obtained from the classic TA, there is a huge color spread artifact on the edges of the stone, which makes it relatively hard to identify the location of the stone. On the image obtained using the AMP mode, the stone is lighted by color precisely. Both the location and the size are emphasized.

b) Variance algorithm

The experimental designs are the same as those used in the AMP algorithm. Figure 3.19 A shows the photo of the human stone used in the experiment. Figure 3.19 B is the B-mode image of the stone in the porcine kidney and 3.19 C is the fluoroscopic image of the same stone in the porcine kidney. Figure 3.19 D is the image of the stone using the new TA algorithm and 3.19 E is the image generated using the variance algorithm. The fluoroscopic image does not show the stone well. From the B-mode image, we observed several bright areas in the image; however, it was hard to tell which one was the stone. The new TA was capable of lighting a bigger area of the stone than the classic TA. There was still some noise that was difficult to eliminate by adjusting the Doppler power and the echo intensity thresholds. Figure 3.19 E shows the image generated by the variance mode. It showed better images of the stone as well as its location and size. Unlike the classic TA, the variance mode did not produce a confusing spot that required judgment to identify the stone location.

Figure 3.20 shows the results from the *in vivo* data. It was the same stone as was used in figure 3.18. The images of fluoroscopy and classic TA are the same as those used in figure 3.18. Figure 3.20 C demonstrated that the variance method could light the stone very well. There was a small volume of color pixels shown at the bottom of the image, which was caused by noise.

The comparison among different imaging modalities *in vitro* and *in vivo* is shown below. The one-way analysis of variance method was used for the statistical analysis between the different imaging algorithms. RF data and 20 images from 6 human kidney stones *in vitro* and 3 human kidney stones *in vivo* were used in the analysis. The parameter N% was used for the comparison to verify the advantage of the new imaging algorithms.
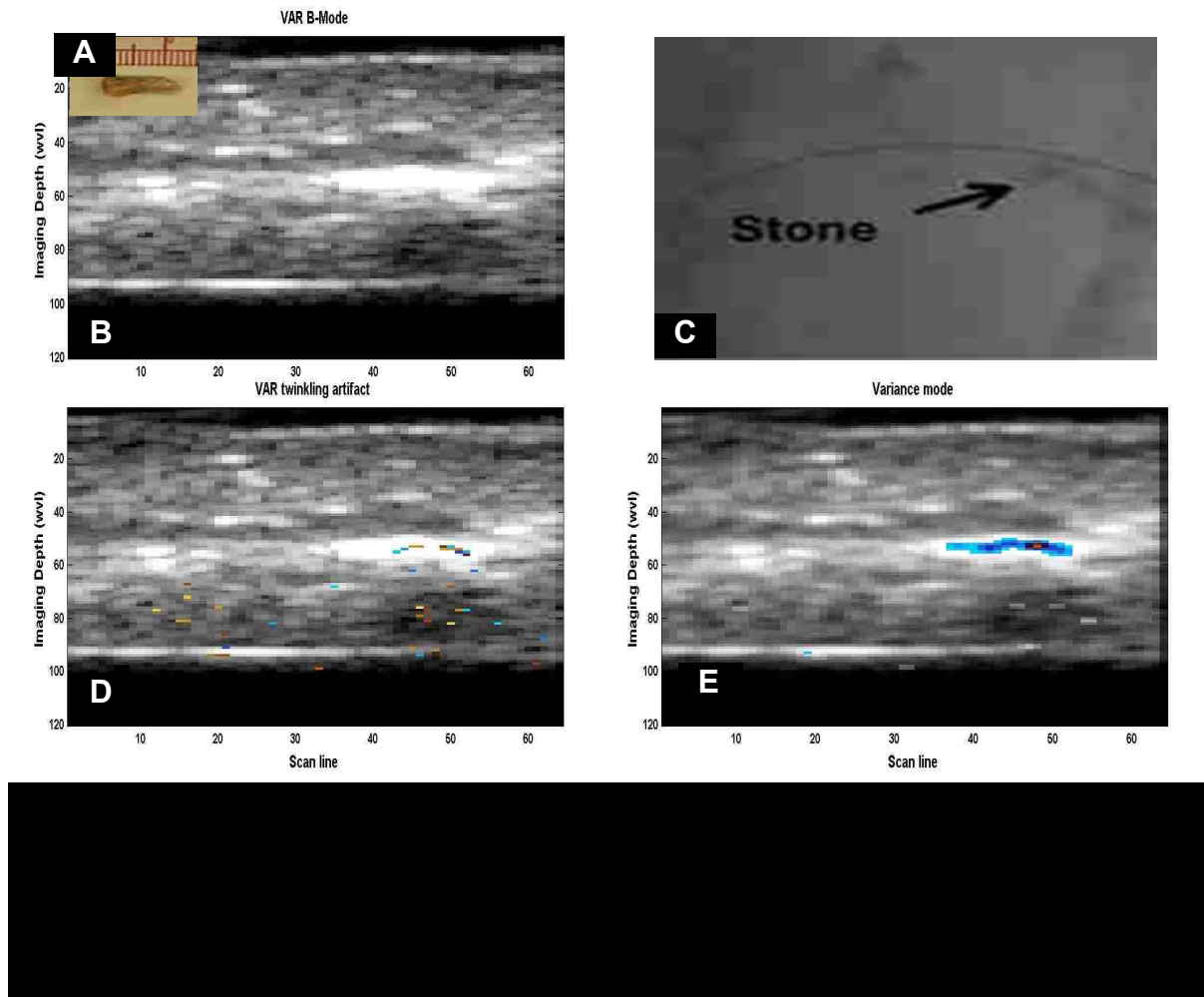
On the left of figure 3.21, for the *in vitro* case, the mean color area was 10.2%, 15%, 40.7% and 59.3% of the stone area for the classic TA, new TA, the variance algorithm, and AMP algorithm, respectively. The new algorithms not only provided a much better contrast than the classic TA, they were also more stable than the classic TA because of the smaller variance in N%. The p-value of

the N% among those imaging algorithms was p<0.000001, which means there was statistical significance in the N% among those techniques. The abilities of different detection algorithms are different.
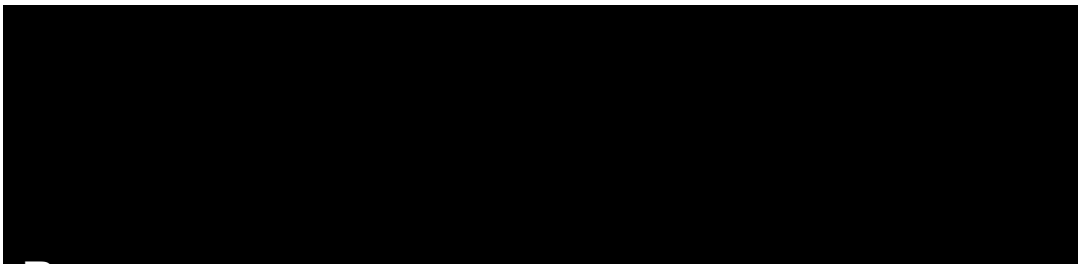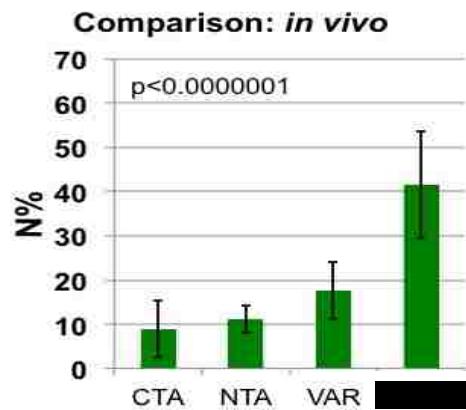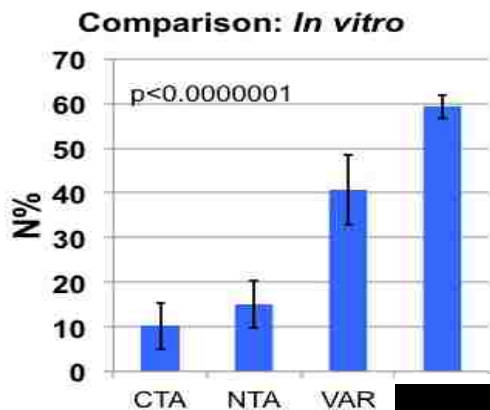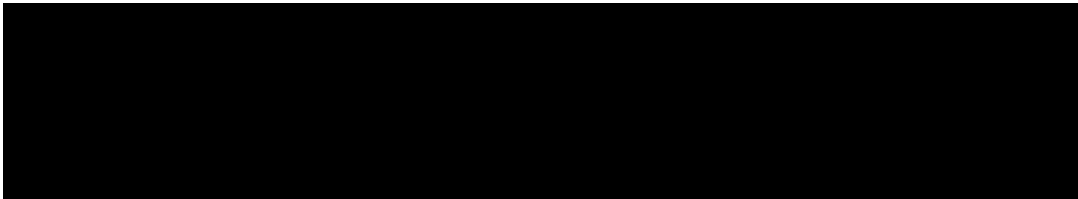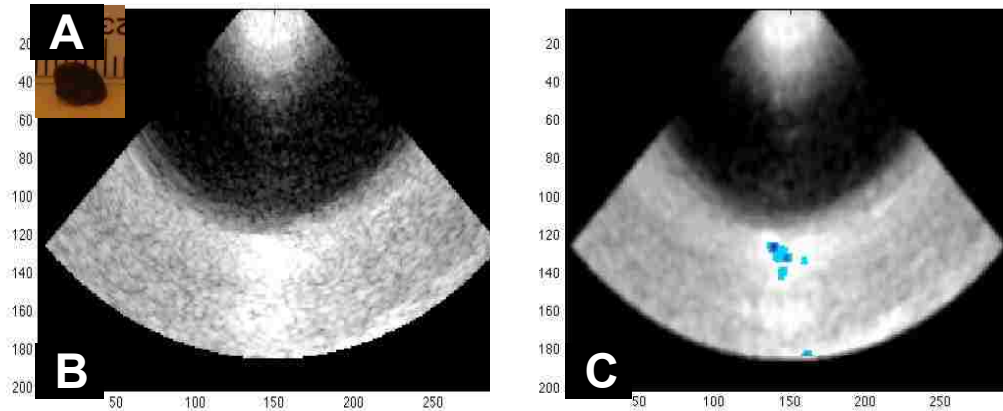
For the *in vivo* case (the right figure of Fig. 3.21), the variance algorithm and the AMP algorithm still provide higher contrast than the other algorithms; the mean of the N% is 17.7% and 45.3%, respectively. The new TA lightens 11.2% of the stone area, which is a little higher than 8.9% area that was lightened by the classic TA. However, the comparison of the variance of the N% shows that the new TA is more stable than the classic TA. The p-value is also smaller than 0.0000001 for the mean of the N% among these imaging techniques, which is significant.

3.4 Discussion

Kidney stone detection differs from blood flow detection because of the different acoustic properties. The classic TA is based on the normal color Doppler algorithm that is optimized for blood flow imaging. Although existing literatures [6-10, 51-52] has reported that the classic TA could provide high accuracy (> 80%) for kidney stone detection, it is still not a stone-specialized imaging method. According to the basic color Doppler theory and our investigation into the mechanism and signal properties of the TA, there are many improvements or modifications that could be done to make the classic TA more stable and accurate.

Figure 3.22 shows the route map of this chapter. The strategy for the improvement and modification was introduced from two parts: 1) color Doppler signal processing: because of the difference within the acoustic properties between the stone and blood flow, modifications to the wall-filter, Doppler power magnitude, and brightness thresholds were proposed; 2) technical parameter modification and optimization: the effects of pulse length (PL), the ensemble length (EL), transmitting power, PRF, and TGC on the TA are investigated. Based on the results of the modification and the optimization together with what we learned on the mechanism and the signal properties of the TA, three new stone detection modes: the new TA, variance, and AMP were created and tested.

A comparison on the capabilities of stone detection for different detection algorithms was simulated on the *in vitro* and *in vivo* data.
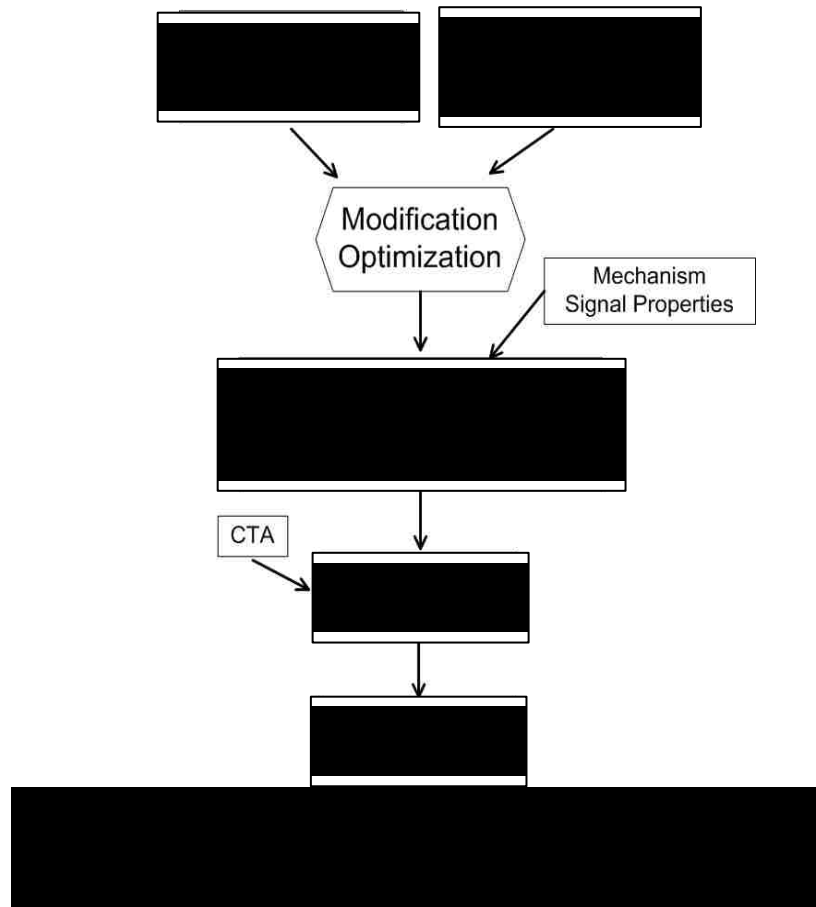
For color Doppler signal processing: the beam-former, the quadrature demodulation unit, the grey-scale image construction, and the autocorrelation algorithm have a limited ability to distinguish signals, for example whether come from the stone (Appendix B). The wall-filter and the color encoding priority (thresholds) are two main units that affect the display of the TA. The regression filter is widely used as the wall-filter in the color flow imaging system; the other two types of filters, the finite impulse response (FIR) filter and the infinite impulse response (IIR) filter are not suitable choices for the wall-filter as the FIR filter needs a large data sample that cannot be afforded by the color flow imaging

system, and IIR filters have such a poor transient time that they could introduce significant bias in the mean frequency estimations. We tested the effects on the Doppler power when performing different orders of the regression filter. Our results (figure 3.2) indicate that the strength of the peak value of the Doppler power decreased as the order of the regression filter increases. When the number of sample points is fixed, the high-frequency signal is better approximated using higher order regression filters; thus the, remaining total energy is smaller. While this agreed with our observations, there is still Doppler power left after performing even a 7th order regression filter. This finding suggests that the TA signal is not the signal with a certain frequency but rather it performs like broadband noise. Therefore, the order of the regression filter needs to be set as low as possible to allow more twinkling artifact signals to pass through.

The color encoding priority and the thresholds are critical for color Doppler imaging. As we mentioned previously, these thresholds determine whether the pixel shows color information. Several common thresholds that most machines use were introduced in section 3.2.2 b. In order to make them suitable for stone detection, the following modifications are made: 1) the Doppler power magnitude threshold was modified so that only when the magnitude of the Doppler power was higher than a certain value, the corresponding color information was displayed; 2) the maximum echo intensity threshold was modified so that the color information would only be displayed if the echoes from the stone were higher than that from the surrounding tissue or blood flow; and 3) the Doppler bandwidth threshold was not necessary for stone detection as the signal of the TA had a broad bandwidth.

For technical parameter modification and optimization: There are several parameters that may affect the TA, such as the pulse length, the ensemble length, the transmitting power, the PRF the TGC, *etc*. The influences of these

parameters on the TA were tested quantitatively and the modification suggestions were provided. The results showed that:

a) The mean peak value of the Doppler power increased with increasing pulse lengths from 1 cycle to 5 cycles before a large drop in magnitude as the pulse lengths increased from 5 cycles to 10 cycles. Comparing to the magnitude of the Doppler power, the magnitude of noise within the experiment was negligible. Therefore, the SNR was comparable using the magnitude of the Doppler power between cases with different pulse lengths. The higher the magnitude of the Doppler power, the better the SNR. On the other hand, the wider the pulse duration, the larger the area that twinkles. Therefore, a balance is needed in the Doppler pulse setting, as there is a tradeoff between SNR and large twinkle areas. Furthermore, the longer the pulse length, the more energy that was introduced into the image, which would need to be measured to check for safety issues.

b) The longer the ensemble length, the more sensitive the machine was to slow velocities. From figure 3.9, the mean peak amplitude of the Doppler power was similar among cases of different ensemble lengths such that there was no statistical difference. These results suggest that the ensemble length was not critical for showing the TA; therefore, we can make the ensemble length as short as possible to increase the frame rate.

c) Because the PRF is related to the image depth, an unsuitable adjustment of the PRF could cause aliasing on the display. In clinical practice, the PRF adjustment is used to increase the detectable velocity scale (Eqn. 3.2). In this study, the effects of PRF on the TA were investigated quantitatively based on the collected RF data. There was no statistical significance showing that the PRF could affect the peak Doppler power magnitude. However, the biggest difference, which happened between 1 kHz and 10 kHz, was 7 dB. The fitting curve suggests that the lower the PRF, the higher the peak Doppler power. Although the PRF has the potential to improve the signal to noise ratio (SNR), the

statistical analysis on the N% showed that there was no statistical significance among N% under different PRFs. It suggested that there was no need to optimize the PRF. In addition, the maximum frequency shift of the TA was estimated for each PRF case, where it was shown that the estimated maximum frequency shift from the experimental TA spots was very close to the theoretical estimation. This result suggests that the PRF can be set as high as possible for separating blood flow from twinkling since the frequency shift from blood flow is limited. This suggestion is contrary to the suggestion on how to adjust the PRF for better SNR.

d) Increasing the transmitting Doppler power increases both the pressure in the acoustic field and the magnitude of the Doppler power. The measurement of the pressure field under different transmitting powers was shown in the Appendix E. Our results showed that the peak Doppler power or the N% does not increase linearly with the increase in the transmitting power. The TA was observed on the screen when the transmitting power was beyond 20 V (P^+~2 MPa, P^-~1 MPa at 4 cm) and the tendency is similar for the N%. These results show that the TA can only be detected or initialized beyond a certain transmitting power level. In addition, at the 20 V transmitting power, the color area is bigger than the area at 10 V, even though the peak Doppler power has the same magnitude at 20 V and 10 V. This result suggests that when the incident power is just beyond a certain level, twinkling will be initialized for a larger area rather than enhancing the peak Doppler power within the color area. Another interesting concept is that the variance of the peak Doppler power is much smaller before the applied peak voltage reaches 20 V than when the peak voltage exceeds 20 V. This result shows that the peak Doppler power varies more violently when the TA exists. When the applied peak voltage increases from 35 V to 36 V, the Doppler power drops and so does the N%. This is explained by updates to our VUE hardware where the maximum power level was set to be 35-36 V, and which may cause some unstable effects when the maximum power level is reached. So far, the

whole investigation shows that the transmitting power does affect the Doppler power and N% and it plays an important role in the initialization and enhancement of the TA.

e) Increasing TGC increases the number of color pixels that can be seen on the screen. The results show that the TGC works appropriately for amplifications between12 dB to 48 dB. The peak Doppler power and the color area increase linearly with increases in the TGC. For the range from 48 dB to 60 dB, the increase in Doppler power and the N% are both mild. The possible explanation is that the received signal was saturated after the amplifier. A similar tendency was observed with the amplification range from 0 dB to 12 dB, which suggests that the TGC may not work well for showing the TA at these levels. Another interesting observation is that the variances of the peak Doppler power and N% for different TGCs are similar to each other. Since the variance represents the measurement of how far away the Doppler power estimations are spread out from the mean value, the results show that the TGC is capable of enhancing the amplitude of the signals but has limited influence on the variability within the signals.

Besides the new TA algorithm, two new stone detection algorithms were developed. Figures 3.17 and 3.18 show the results and comparisons among multiple imaging modalities for human kidney stones *in vitro* and *in vivo*. B-mode ultrasound did not separate the stone from surrounding tissue well most likely due to the hard compression of strong echoes in the imaging field. Fluoroscopy, as the most commonly employed technique for kidney stone detection during the lithotripsy, did not show the stone well either. One possible reason is that the stones we used in the experiment are radiolucent. The biggest problem with the TA in the normal color Doppler mode is the instability. The TA in figure 3.17 D can be interpreted as noise. In figure 3.18 D the real TA is hidden behind a big color artifact along the wave front. Using the AMP algorithm, not only the location of the stone, but also the size of the stones are lit up. The surrounding tissue is

85

still present with the grey-scale information. We don`t know exactly why this algorithm works so well. A possible explanation is that, increasing the abnormal pulse from 0.1% to 10% in amplitude for all scan lines introduces more fluctuation within the slow-time axis such that more energy leaks from the wall-filter into the Doppler residual. Since pixels on the stone are usually shown with high amplitude reflections, the Doppler residual from the stone may contain more energy than the tissue. The only problem would be that it is more complicated to migrate to the VUE since the AMP mode needs to work on the RF data level and the approximated amplify ratio is hard to predict unless it can be adjusted *in vivo*; however, these problems are solvable. One method would be to work with the IQ data generated by the VUE. The advantage of dealing with the IQ data is that we can take advantage of the processing algorithms provided by the VUE while the disadvantage is that we cannot employ some of our algorithms, *i.e.*, the adaptive beamforming algorithm. Another solution would be to access the p-data, [86] which is used to store the RF data in the VUE, and rewrite the whole processing algorithm to work from the p-data. This solution could give us more freedom on employing the algorithms; however, the efficiency of our current beamforming and processing algorithms will be a concern for clinical practices. More optimization on the algorithms should be done in the future.

The variance algorithm is a simple mode to apply and easy for the VUE migration. From figures 3.19 and 2.20, the variance mode lights the stone better than both the B-mode and the new TA method we developed. The stone creates dramatic variance between the Doppler pulses; the variance we talk about here is different from the variance in the color Doppler imaging system that is used to detect the turbulence within the flow. The variance is statistically defined as the measurement of the dispersion of the values around the mean. We can treat it as a simple wall-filter that filters Doppler signals by subtracting the mean value. Therefore, the comparison between the variance mode and the new TA is the comparison between the effects of different filters.

Then we compared the abilities of different imaging algorithms for stone detection. There is statistical significance among the abilities of different imaging algorithms for stone detection, not only shown on the *in vitro* data but also shown in the *in vivo* studies. The AMP algorithm can light up the largest area of the stone, with the variance mode close behind. As far as the other two techniques, the new TA method performed better than the classic TA (10.2% VS 15%, *in vitro* and 8.9% VS 11.2% in *vivo*), and most importantly, the stability of the new TA is also better than that of the classic TA, especially in the *in vivo* case (std, 2.9% VS 6.5%). These results indicate that all the new algorithms can improve stone visualization, though some of them improve it to a larger extent than others. In all cases, however, the area occupied by color is smaller in the *in vivo* case than the *in vitro* cases. The variance mode, for example, it is 40% of the stone *in vitro* which decreased to 17% *in vivo.* This is most likely explained by the attenuation of the body wall in the *in vivo* case, but may also be due to noise from breathing and tissue motion.

3.5 Conclusion

In this chapter, three new stone-specialized imaging algorithms were developed based on the color Doppler imaging theory and the mechanism and signal properties of the TA. Several technical parameters that may affect the TA were tested and the influences from each parameter were quantified and analyzed. The results of the comparison among the new algorithms and the classic TA show that, under the same conditions, the new algorithms can not only light up the stone better, but also are more reliable techniques for stone detection.

Chapter 4

Ultrasonic expulsion for kidney stones

The work presented in this chapter is not my major project. My contributions are mainly on the phantom studies and experimental data processing and analysis.

4.1 Introduction

Extracorporeal shock wave lithotripsy (ESWL) is the most common treatment used for kidney stone disease today. The stone free rates for lithotripsy are 40-90%, depending on the machine used in the treatment. Despite the evolution of technology-driven surgical approaches, the success in surgical management of lower pole stones is principally dependent on two processes: stone fragmentation and residual fragment clearance. The clinical need to establish complete stone clearance is highlighted by Chen and Streem [43] who prospectively followed 206 patients with isolated lower pole calculi treated with ESWL. This study concluded that post-ESWL, the probabilities of a symptomatic episode or requiring intervention at 5 years were 0.24 and 0.52, respectively.

The residual stone fragment is a big problem in the treatment of urolithiasis. Currently, the German urological society recommends inversion (bending the patient over) and percussion (rapping on the patients back) therapy in the hope of helping stone fragments pass naturally. However, the data on the effectiveness of these approaches are inconclusive. [22-24] Other researches have investigated different ways of surgically implanting catheters to remove pieces by irrigation. [21] There are even early reports and recommendations of follow-up SWLs to "stir-up" the pieces to help them pass. [45] This additional SWL practice fell out of favor as the side effects of SWL were recognized and thus was no longer justified.

During the investigation on the lithotripsy, we usually observe the 'jump' of stones resulting from the acoustic radiation force and related acoustic streaming.

Acoustic radiation force is commonly used to move objects such as bubbles [46], drops [47] and cells [48]. Streaming associated with radiation force has been used to diagnose fluid-filled cysts [47] and bleeding from clotted blood [48].

If stones or stone fragments could be moved by using acoustic radiation force and associated streaming from the lower pole to the renal pelvis for the treatment, the post-surgical stone-free rates will be improved and the number of patients having to undergo a second lithotripsy – a second exposure to the maximum dose – would be reduced.

In our preliminary study, we successfully moved a U30 artificial stone in a kidney phantom by using a high-intensity focused ultrasound (HIFU) transducer, as shown in figure 4.1. The artificial stone was implanted into a liquid-filled void kidney-mimicking phantom. A HIFU transducer (fc: 1.1 MHz) was held by hand on the bottom of the phantom. The radiation force lifted the stone and the user then moved or angled the source and pushed the stone to one side or another.
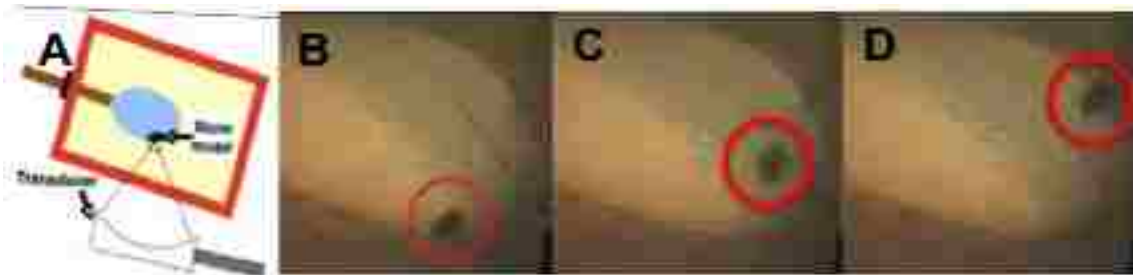
To date, no research has been performed investigating the use of ultrasound radiation force as a mechanism to improve stone clearance and post-surgical stone free rates. We describe the development, *in vitro* and *in vivo* testing of a prototype device that uses non-invasive ultrasound imaging to guide the application of focused ultrasound to move stones within the renal collecting

system. The goal of this new device is to guide lower pole fragments out of a dependent caliceal position to a more superior position to facilitate spontaneous clearance of stone fragments.

4.2 Methods

Acoustic radiation force results from the transfer of acoustic wave momentum to an absorbing object and is one example of a universal phenomenon associated with all forms of wave motion [83]. From our preliminary study, we learned that there is sufficient force to non-invasively reposition kidney stones and stone fragments in the collecting system of the lower pole when the stone is aligned in the focal area of the acoustic beam. Therefore, with the proper alignment of a focused beam upon a stone, it can be guided to a position that promotes spontaneous clearance or, for larger stones, increases the efficacy of stone removal therapies.
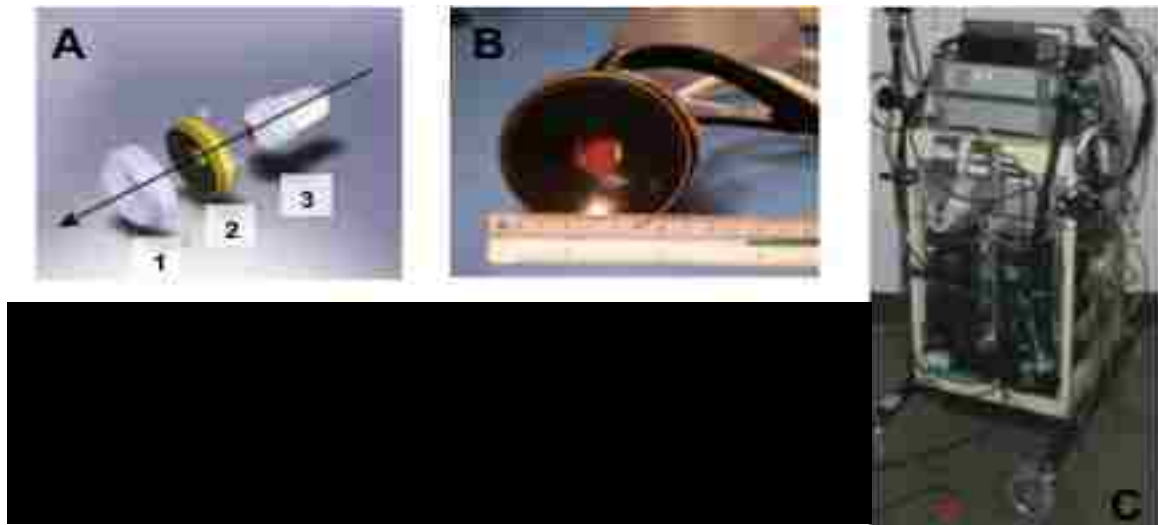
4.2.1 System Development

A new hand-held probe for an ultrasound-guided stone repositioning system, as shown in figure 4.2, was developed. The probe of the new system contains two ultrasound transducers: a commercial imaging probe (HDI P4-2, Philips Healthcare, Andover, MA) and a focused ultrasound probe. An HDI 5000 (Philips

Healthcare, Andover, MA) generated ultrasound images that were used to visualize and target the stones. The focused probe consists of an 8-element annular array with a nominal frequency of 2.0 MHz. The diameter of the active area was 63 mm and the diameter of the inner imaging aperture was 20 mm. Array elements were driven by separate amplifiers and by adjusting phase delays; the focal depth was programmable within a range of 4.5–8.5 cm on axis.

The numerical simulation of the focused acoustic beam is shown in figure 4.3, which shows the energy distribution in the focal zone and the spatial resolution that the stone-repositioning system can provide. Ultrasound was coupled to the tissue phantom by a water-filled standoff.
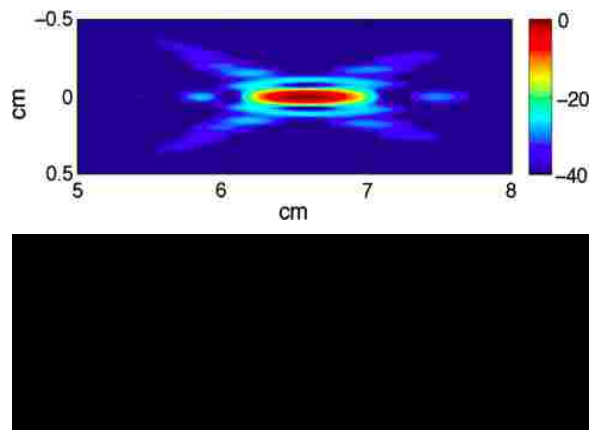
4.2.2 *In Vitro* Tests

A kidney phantom was created using polyacrylamide gel, the same gel as the stone gel phantom we used in chapter 2. While the gel polymerized, a void to simulate a collecting system and lower pole was created using the cast of an 18F silicone Foley catheter. Artificial stones, metal-plated glass beads from 2.5 to 4.0 mm in diameter, and human urinary calculi, from 3 to 8 mm in diameter, were placed dependently in the simulated collecting system. The kidney phantom with an artificial stone inside is shown in figure 4.4.

Human urinary calculi consisted of calcium oxalate and calcium hydrogen phosphate dihydrate (also known as brushite) and were >90% in purity. These stones were rehydrated for more than 24 h before experiment.

Once placed in the simulated lower pole, stones were located and visualized by ultrasound imaging. Coaxial arrangement of the imaging and focused probes

permitted positioning of the device to locate the stone within the imaging plane and within the programed focal volume of the annular array. Focused ultrasound was then delivered at instantaneous acoustic powers of 5–40 W, duty cycle of

50%, and duration of 2–5 s. Stone motion in the kidney phantom was concurrently monitored by fluoroscopy and video photography, from which velocity, displacement, and trajectory were recorded.

4.2.3 *In Vivo* Tests

All animal studies were approved by the University of Washington IACUC. Six common domestic female pigs (50-60 kg) underwent endoscopic and/or open surgery after induction of general anesthesia. In six pigs, artificial stones (radio-opaque glass/metal beads 3 and 5 mm in diameter) and human kidney stones (cystine, calcium oxalate monohydrate, or calcium phosphate, 1-8 mm) were endoscopically placed into the lower or midpole calyx via retrograde ureteroscopy or antegrade percutaneous access using a nitinol basket. Stone position was visually confirmed endoscopically and fluoroscopically. Focused ultrasound energy was used to displace these stones/beads out of the calyx.

The kidneys were harvested immediately after ultrasound exposure. Briefly, the tissue was carefully sectioned so that central cross-sections of the lesions could be analyzed. The trimmed regions of interest were embedded in optimum cutting temperature (O.C.T., Sakura Finetek, USA). Sequential sections of 8 micrometer thicknesses were stained with Hematoxylin and Eosin (H&E) for morphological analysis. All slides were evaluated within 24 hours of staining. Normal untreated tissue was used as a control. All reagents are obtained from Sigma (St Louis, MO).   Any signs of injury to the renal parenchyma were assessed by observers blinded to the exposure conditions.

The device used in *in vivo* tests is the same as that used in the *in vitro* tests. A laptop which controls the focal depth also collected the image from the ultrasound imaging system (HDI-5000, Philips/ATL, Bothell, WA), and the selected focusing depth was overlaid on the image. This allowed the operator to visually align the stone at the focus. A footswitch turned the focused ultrasound on for about 50 ms and off for about 50 ms while the switch was closed. Total exposure in a burst of pulses was 1-4 s, and no more than 10 bursts were used to move one stone. The acoustic beam is shaped as an hourglass with the greatest energy concentration and highest pressures in the narrow focus region. The region over which the pressures are within half of the peak pressure is only 1 cm long and about 1 mm wide. Time-averaged acoustic intensities measured in water and derated to the 6.5 cm penetration depth in tissue were 200 W/cm^2.

4.3 Results

4.3.1 Results of *In Vitro* Tests:
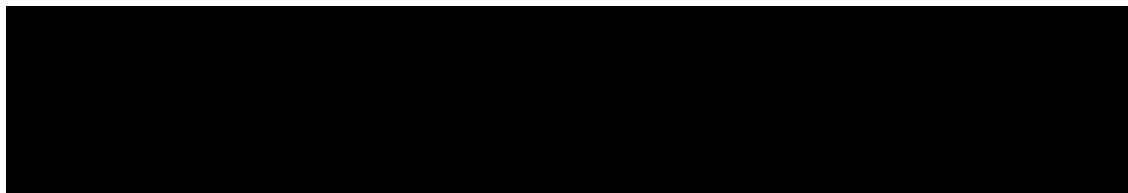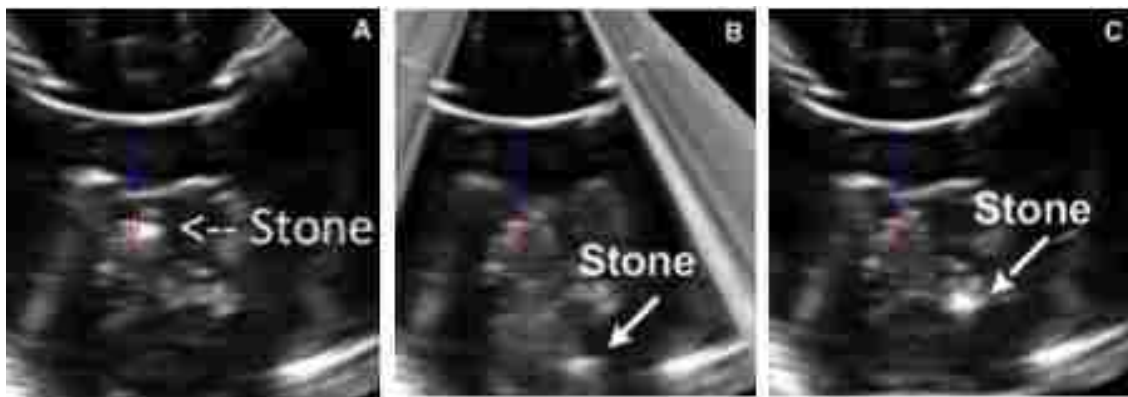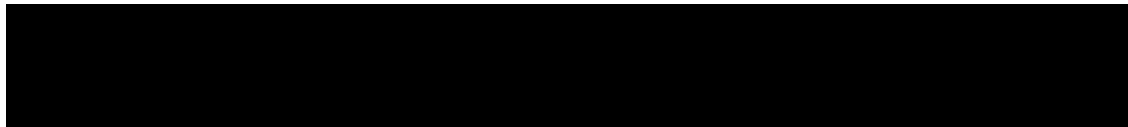
In the kidney phantom, delivery of focused ultrasound resulted in stone motion from the lower pole into the collecting system. Stone motion was seen immediately after application of the focused ultrasound and the stone velocity was on the order of 1 cm/s. Figure 4.5 shows fluoroscopic images of an artificial stone's initial position in the lower pole, trajectory in response to focused ultrasound, and final position within the collecting system. Stone motion and repositioning were observed for both artificial and human urinary stones and were independent of stone size. Operators could generally control the direction of stone displacement and we found that the best angle of focused ultrasound exposure was in line with the simulated infundibulum. However, this angle could

be difficult to determine extracorporeally.

All powers used moved the stones with essentially the same rate, but at least 10W was required to lift the largest stone, 8 mm, all the way to the collecting system. As many as six stones placed in the collecting system at one time were all repositioned to the lower pole. Although energy was directed toward the collection of small stones and could lift slightly many stones at once, only one stone was repositioned to the collecting system with each pulse. Additionally, stone motion was not observed at all angles of focused ultrasound delivery. Angles of focus that were parallel to the axis of the simulated infundibulum resulted in larger displacement.

Figure 4.6 shows ultrasound images analogous to the fluoroscopy images in Fig. 4.5, and demonstrates how the integration of ultrasound imaging and focused ultrasound can be used to detect and target residual stones, reposition them in the collecting system, and provide the user with real time visual feedback. Hyper-echogenic vertical bands on the edges of Fig. 4.6B resulted from delivery of focused ultrasound and illustrate how ultrasound imaging can be synchronized to maintain visualization of the stone. Figure 4.7 shows video photography monitoring analogous to fluoroscopy and ultrasound.
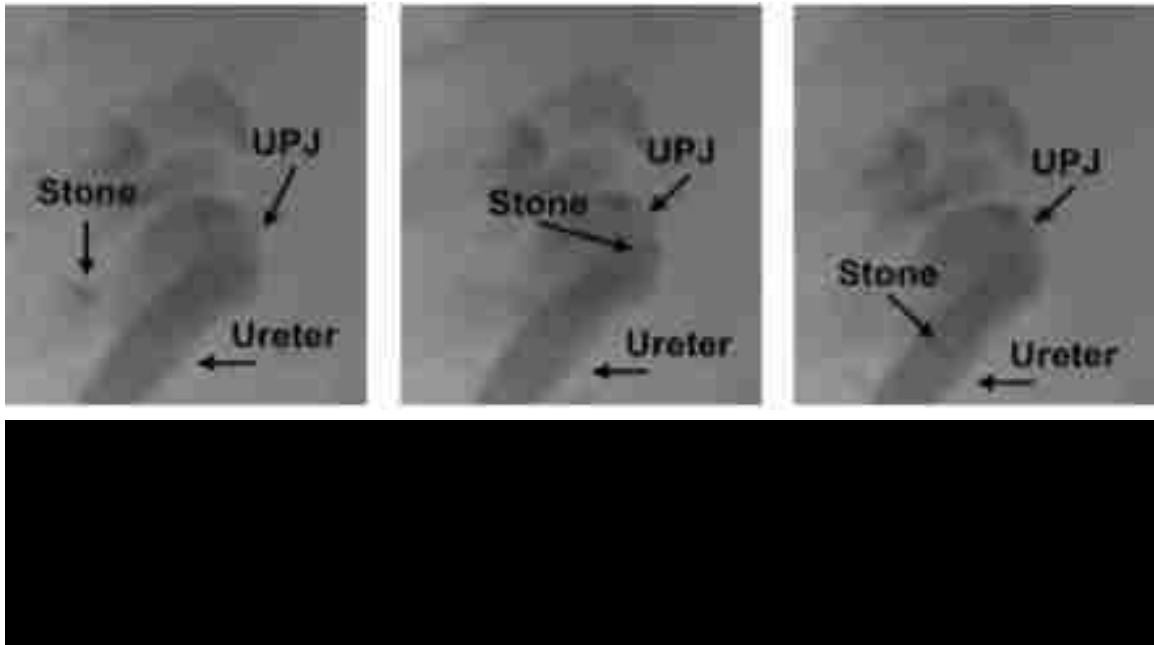
4.3.2 Results of *In Vivo* Tests:

Stone motion was observed with both ultrasound and fluoroscopy.   Figure 4.8 shows a representative image of ultrasonic propulsion of a stone. In this example, a single second ultrasound burst pushed the 5 mm bead from the lower pole to the UPJ and ultimately down an indwelling ureteral access sheath. The bead moved several centimeters in 1.3 s (Figure 4.8).   Stones or beads were moved to the renal pelvis and ureteropelvic junction (UPJ) in all six pigs. No more than ten minutes per stone relocation event were required, and total exposures to focused ultrasound were shorter than two minutes.   Most of the effort involved visualizing the stone at an appropriate angle to push it through the infundibulum toward the renal pelvis and UPJ. Figure 4.9 shows another example of a stone that was repositioned in the porcine kidney. The stone was moved past a bead implanted in a pig kidney within 1s. This example shows that the pushing target can be well controlled by aligning the delivered ultrasound pulses with the target. Stone motion was not observed at all angles of focused ultrasound delivery. We observed that if stones were pushed towards the papilla, then the stone ricocheted in a direction along the interface. Larger fluid spaces created via

hydrodistension of the intrarenal collecting system made propulsion easier. Some stones were resistant to repositioning despite graduated increases in the power output. Angles of focus that were parallel to the axis of the infundibulum resulted in larger displacement of the stone. There was no difference in the ability to move stones of varying compositions.

The mechanical (cavitation) damage and thermal damage were estimated. No injury was observed in any sections as shown in figure 4.10.
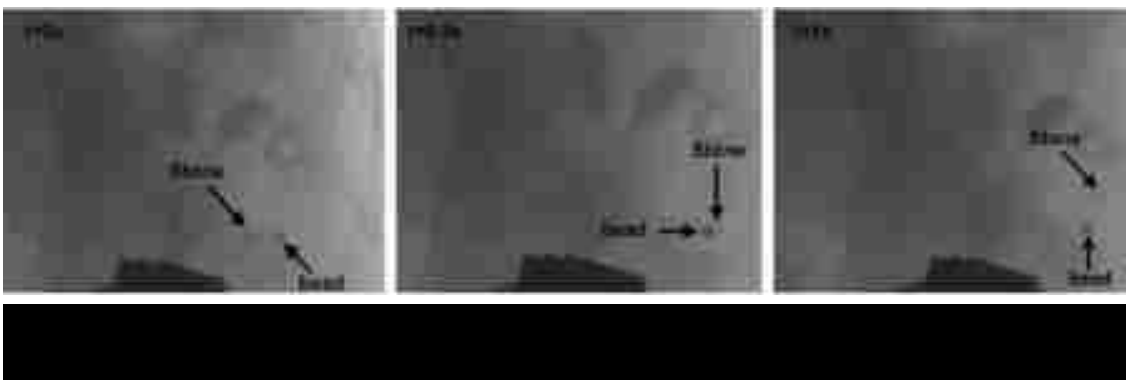
4.4 Discussion

Residual stone fragments have been shown to be a potential cause of significant morbidity resulting in symptomatic episodes and/or need for further intervention. [43, 84] Unfortunately, residual stone fragments are common and a randomized trial showed low stone-free rates (SFRs) following both ureteroscopic lithotripsy (URS) (50%) and SWL (35%) for lower pole calculi smaller than 1 cm. [1] Granted, technology has advanced since this study and smaller flexible ureteroscopes that allow greater deflection capabilities, along with smaller nitinol baskets, theoretically would impact the URS SFR if repeated. Although percutaneous nephrolithotomy (PNL) [85] provides a higher SFR for lower pole calculi, many believe this to be an overly invasive option, especially for stones of 1 cm or less. We have described a safe and effective device and method to expel small stones or fragments from the kidney in a completely non-invasive manner. This

technology is portable and could potentially be used either in the clinic or operative setting. The efficacy of the system has been tested for both *in vitro* and *in vivo* cases.

In the *in vitro* tests, as expected, larger stones were the most difficult to reposition and perhaps this observation is due to higher stone mass as well as difficult maneuvering past a narrow infundibular channel. This technology is not dependent on stone composition as a variety of common human calculi subtypes were able to be repositioned. Although this was an *in vitro* study to evaluate feasibility, the low potential of *in vivo* tissue injury can be assessed by comparing acoustic intensities to the limits determined by the FDA for diagnostic ultrasound imaging: $I_{SPPA} \leq 190$ W/cm^2 to prevent cavitational injury and $I_{SPTA} \leq 720$ mW/cm^2 to prevent thermal injury [86]. Focal intensities can be estimated as total acoustic power delivered by the transducer per cross-sectional area of the focal beam width. A total power of 10 W, enough to lift the largest stone in this study, relates to focal intensity of $10/\pi 0.3^2$, or approximately 30 W/cm^2. This is the spatial-averaged pulse-average intensity, I_{SAPA}, which must be multiplied by 1.6 [87] to attain the spatial-peak pulse-averaged intensity, I_{SPPA}, of 45 W/cm^2 which is lower than the FDA limit. The spatial-peak time-averaged intensity, I_{SPTA}, is I_{SPPA} multiplied by the temporal duty factor, 50%, or 23 W/cm^2, which is higher than the FDA limit. However, because exposure times to reposition stones were 2–5 s, as opposed to 10 min for diagnostic ultrasound, the risk of thermal injury is low. As another point of comparison, intensities 2–3 orders of magnitude higher, I_{SPTA} of 1,500–15,000 W/cm^2, such as those used for high intensity focused ultrasound (HIFU), are necessary to induce tissue necrosis during similar exposure times. [88] Figure 4.11 shows the intensity scale for the ultrasound intensities commonly used in diagnostic, stone repositioning, and HIFU.

In the *in vivo* tests, stones or beads were moved to the renal pelvis and ureteropelvic junction (UPJ) in all six pigs successfully in a short time (less than 2 minutes). Pushing angle is still important. Propulsion of stones did not occur at all

angles and aligning the ultrasound energy in the direction of the infundibulum appears to be most effective. We also proved that we could precisely control the repositioning target by adjusting the transducer. An injury analysis has been done for the kidney after the ultrasound exposure with typical intensities used for stone repositioning. There is no visible evidence of the thermal or mechanical injury from the treatment.
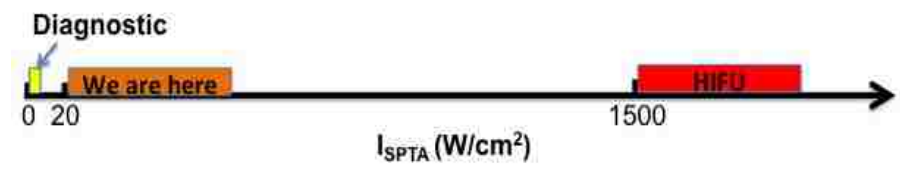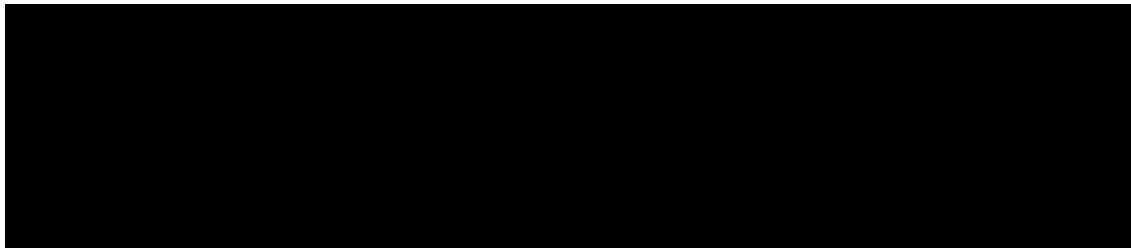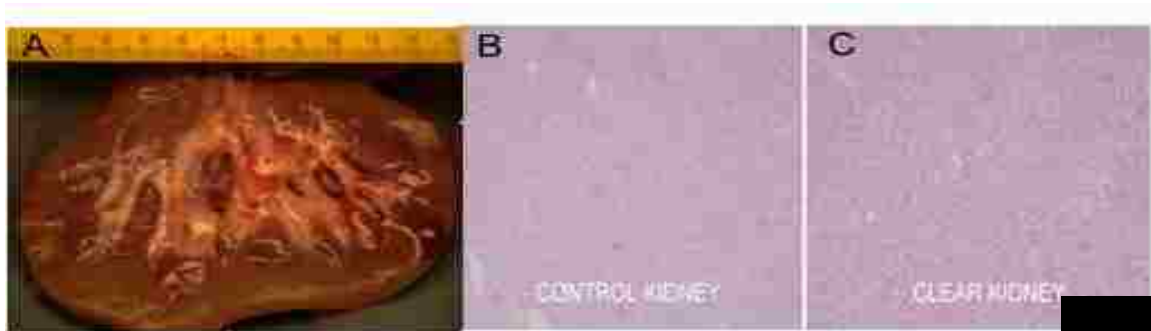
Advantages of this new technology include handheld portability, reusability, and no required sterilization. As ultrasound exposure has no known harmful side

effects and is a painless exposure, the device could be potentially used in awake, non-anesthetized patients in a clinic or emergency room setting.

Potential applications for this device also include adjunctive use with primary medical expulsive therapy and the management of obstructing ureteropelvic junction stones by pushing the stone back into a non-obstructing location. The device may also be used in patients with known infectious stones where it has been well established that complete stone clearance is essential to prevent further stone formation as well as reduce the likelihood of recurrent infection. Lastly, this ultrasound- based device may also be used in the management of renal calculi in the pediatric and pregnant populations where there is greater concern over the effects of ionizing radiation [89] common to ureteroscopic, SWL, and percutaneous stone management. The ability to move stones might even offer benefit to diagnostic ultrasound imaging of stones by for example distinguishing between a single large stone and a cluster of multiple stones. Such a distinction may be an important branch point in the clinical decision making algorithm.

Chapter 5

Summary and Future Directions

5.1 Summary

Kidney stone disease affects 1 in 10 Americans with more than 3 million diagnoses and treatments each year and costs of approximately $2.1B. [1-2] In kidney stone diagnosis, while X-ray computerized tomography (CT) is the most commonly used technology, patient exposure to the ionizing radiation used in CT scans may increase the risk of cancer. Recently, the Food and Drug Administration (FDA) recognized this risk and has moved to reduce exposure to X-rays. In kidney stone treatment, extracorporeal shock-wave lithotripsy (ESWL), which uses ultrasound to break the stone, is widely used; however, while small stone fragments in the renal pelvis usually pass naturally, those located in the lower pole are more likely to remain and can act as the nucleus for another stone to form. Stones will recur in 50% of patients within 5 years. In order to solve these problems in kidney stone diagnosis and treatment, novel ultrasonic technologies have been developed.

While the TA has been shown to highlight kidney stones during ultrasound color Doppler imaging, the instability in the TA has prevented it from being adopted clinically. To solve this problem and accelerate the application of the TA into clinical stone detection, the underlying mechanism of the TA was investigated and new imaging algorithms were developed as part of this dissertation. Based on per-channel RF data analysis of *in vitro* human kidney stones collected from the VUE, the mechanism of the TA was investigated. The analysis began by minimizing the signal processing ambiguity of the TA by using self-developed algorithms. The acoustic and machine effects were separated by sending synthesized RF signals directly into the VUE where it was determined that the machine did not cause the TA. The acoustical effects of the TA were investigated by applying high static pressure (up to 8.5 MPa) on human kidney stones, where

it was determined that the TA was caused by microbubbles trapped in crevices, while modeling simulations showed that stone ringing did not contribute to the TA. However, there is some concern that these crevice microbubbles are not present *in vivo* – that they were introduced onto the old stone by the drying and rewetting process. Therefore, fresh human kidney stones that had only limited air contact were exposed to overpressure, where the results again showed that crevice bubbles caused the TA on the stones.

New imaging algorithms for improved stone detection, including new TA, variance, and AMP algorithms were developed based on the crevice bubble mechanism and the resultant signal properties of the TA. The three imaging algorithms were quantitatively compared by N% based on the RF data analysis to the classic TA, which showed that the new algorithms were more stable and sensitive than the classic color Doppler TA. In addition, the influence of the PRF, pulse length, ensemble length, TGC, and transmitting power on the TA were tested and quantified. Besides the improvement in kidney stone detection, kidney stone treatment was also improved via a novel ultrasonic technology that could expel small kidney stones or stone fragments from the kidney. The results from this work are beneficial not only for doctors who are apt to use ultrasound for kidney stone diagnosis and clearance, but also for patients to avoid ionizing-radiation exposure from CT scans while reducing stone recurrence rates by eliminating lower pole residuals.

5.2 Future Directions

While this dissertation discussed the mechanism of the TA and developed new imaging algorithms based on the mechanistic results, there is still room to improve ultrasound kidney stone imaging for even better kidney stone detection. Since crevice bubbles play an important role in the TA, all possible existing bubble detection methods could be leveraged for kidney stone detection. However, it should be noted that the detection method must be capable of finding

stochastic signals rather than simply nonlinear signals, since the crevice bubbles behave randomly when driven by periodic acoustic waves. Meanwhile, some modifications could be done on the transmittance of the ultrasound waves. For instance, a waveform with a strong amplitude could be sent to stimulate bubble growth before the Doppler ensemble. These two modifications would be good supplements to our three current imaging algorithms.

On the other hand, more sophisticated signal and imaging processing algorithms could be involved. For example, the edge detection method could help confirm the stone location; the harmonic imaging method could reduce the speckle artifact on the image; and the velocity estimator could be used to detect the high estimated velocity close to the velocity scale limits. Last but not the least, the optimization of the processing algorithm, like the processing speed, is very important for the clinical practice *in vivo*.

Thus far, we have received Internal review board (IRB) approval to conduct a clinical trial for our three imaging algorithms allowing us to collect more *in vivo* stone data. This will allow us to improve and optimize our imaging algorithms based on the results of the clinical trial. We hope that these new imaging methods will easily pass through the FDA and be transferred to clinical practice.

References

[1]. M.S. Pearle, E.A. Calhoun, G. C. Curhan. (2005). "Urologic diseases in America project: urolothiasis." J of Urol, **173**(13): 848-857

[2]. C.D. Scales Jr., A.C. Smith, J.M. Hanley, et al. (2012) "Prevalence of Kidney Stones in the United States", European Urology **62**: 160-165.

[3]. L. Landro, (2010). "Radiation risks prompt push to curb CT scan." J of Wallstreet.

[4]. K.A.B. Fowler, J. A. Locken, J.H. Duchesne, et al (2002). "US for detecting renal calculi with nonenhanced CT as a reference standard." Radiology, (222): 109-113.

[5]. S. Ulusan, Z. Koc., N. Tokmak. (2007). "Accuracy of sonography for detecting renal stone: Comparison with CT." J Clin Ultrasound, (35): 256-261.

[6]. A. Rahmouni, R. Bargoin, A Herment, et al (1996). "Color Doppler Twinkling artifact in hyperechoic regions." Radiology (199): 269-271.

[7]. S.K. Aytac, O. Hasan (1999). "Effect of Color Doppler System on the Twinkling sign associated with urinary tract calculi." J Clin Ultrasound **27**(8): 433-439.

[8]. J.Y. Lee, S. H. Kim, J. Y. Cho, et al (2001). "Color and Power Doppler Twinkling Artifacts from Urinary Stones: Clinical Observations and Phantom Stidies." AJR **176**: 1441-1445.

[9]. A. Turrin, P. Minola., F. Costa, et al (2007). "Diagnostic value of colour Doppler twinkling artifact in sites negative for stones on B mode real sonography." Urol Res(35): 313-317.

[10]. M. Mitterberger, F. Aigner, L. Pallwein, et. al. (2009). "Sonographic detection of renal and ureteral stones. Value of the twinkling sign." International Braz J Urol **35**(5): 256-261.

[11]. J.R. Dillman, M. Kappil., W.J. Weadock, et al (2011). "Sonographic Twinkling Artifact for Renal Calculus Detection: Correlation with CT." Radiology 259(3): 911-917

[12]. R.R. Winkel, A. Kalhauge. and K. Fredfeldt. (2012). "The Usefulness of Ultrosound Colour-Doppler Twinkling Artifact for Detecting Urolithiasis Compared with Low Dose Nonenhanced Computerized Tomography." Ultrasound in Med.&Biol 38(7): 1-8.

[13]. S.B. Strem, A. Yost., E. Mascha (1996). "Clinical implications of clinically insignificant stone fragments after extracorporeal shock wave lithotripsy." J of Urol **155**: 1186-1190.

[14]. J.E. Lingeman, Y. I. Siegel., B. Steele, A.W. *et al.* (1994). "Management of lower pole nephrolothiasis: A clinical analysis." J of Urol **151**: 663-667.

[15]. N.P. Gupta, D. V. Singh, A.K. Hemal, *et al* (2000). "Infundibulopelvic anatomy and clearance of inderior caliceal calculi with shock wave lithotripsy." J of Urol **163**: 24-27.

[16]. F.J. Sampaio, A.H.M. Aragao. (1992). "Inferior pole collecting system anatomy: Its probable role in extracorporeal shock wave lithotripsy." J of Urol **147**: 322-324.

[17]. R. B. Sabnis, K. Naik, S.H. Patel, *et al* (1997). "Extracorporeal shock wave lithotripsy for lower calyceal stones: Can clearance be predicted?" J of Urol **80**: 853-857.

[18]. A. M. Elbahnasy, A. L. Shalhav., D. M. Hoenig, *et al* (1998). "Lower caliceal stone clearance after shock wave lithotripsy or ureteroscopy: The impact of lower pole radiographic anatomy." J of Urol **159**: 676-682.

[19]. K. T. Pace, M. J. Weir, N. Tariq, *et al.* (2000). "Individual patient variation and inter-rater reliability of lower calyceal infundibular width on routine intravenous pyelography." J of Urol (suppl) **163**: 341.

[20]. E.R. Nicely, M. I. Maggio, E. J. Kuhn (1992). "The use of a cystoscopically placed cobra catheter for direct irrigation of lower pole caliceal stones during extracorporeal shock wave lithotripsy ." J of Urol **148**: 1036.

[21]. J. B. Graham, J. B. Nelson. (1994). "Percutaneous caliceal irrigation during extracorporeal shock wave lithotripsy for lower pole renal calculi." J of Urol **148**: 2227.

[22]. N Brownlee, M. Foster, D. P. Griffith, *et al* (1990). "Controlled inversion therapy: An adjunct to the elimination of gravity-dependent fragments following extracorporeal shock wave lithotripsy." J of Urol **143**: 1096-1098.

[23]. N. R. Netto, J. Claro, P.L. Cortado, *et al* (1991). "Adjunct controlled inversion therapy following extracorporeal shock wave lithotripsy for lower caliceal stones." J of Urol **146**: 953-954.

[24]. R.J.D. Honey, J. Luymes., M. J. Weir, *et al* (2000). "Mechanical percussion inversion can result in relocation of lower pole stone fragments after shock wave lithotripsy." Urology **55**: 204-206.

[25]. E. Cicerello, F. Merlo, G. Gambaro, *et al* (1994). "Effects of alkaline citrate therapy on clearance of residual renal stone fragments after extracorporeal shock wave lithotripsy in sterile calcium and infection nephrolothiasis patients." J of Urol **151**: 5.

[26]. J. K. Fine, C. Pak., G. M. Preminger (1995). "Effect of medical management and residual fragments on recurrent stone formation following shock wave lithotripsy." J of Urol **153**: 27-33.

[27]. P. N. Rao (2004). "Imaging for kidney stones." World J Urol **22**: 323-327.

[28]. J. Vieweg, C Teh, K. Freed, *et al* (1998). "Unenhanced helical computerized tomography for evaluation of nephrolithiasis." J of Urol **160**(3): 679-684.

[29]. O.F. Miller, S. K. Rineer., S.R. Reichard, *et al* (1998). "Propective comparison of unenhanced spiral computerd tomography and intravenous urogram in the evaluation of acute flank pain." Urology **52**: 982-987.

[30]. D. Assimos, C. G. Chaussy, R.Clayman, *et al* (2003). "Predicting the future. In: Stone Disease: first international concultation on stone disease." Health Publications. Paris.: 375-404.

[31]. K.S. Tseng and B.R. Matlaga, (2008). "A case of a lower pole renal caculus managed with percutaneous nephrolothotomy." Nat Clin Pract Urol **10**: 1038.

[32]. M.A.Jewett, C. Bombardier, D. Caron, *et al*. (1992). "Potential for inter-observer and intra-observer variability in x-ray review to establish stone-free rates after lithotripsy." J of Urol **147**: 559-562.

[33]. C. Kimme-Smith, R. R. Perella., L.P. Kaveggia, *et al* (1991). "Detection of renal stones with real-time sonography: Effects of transducers and scanning parameters." AJR **157**: 975-980.

[34]. W.D. Middleton, W. J. Dodds, T.L. Lawson, *et al* (1988). "Renal calculi: sensitivity for detection with US." Radiology **167**: 239-244.

[35]. S.P. Weinstein, C. Seghal, E.F. Conant, *et al*. (2002). "Microcalcifications in breast tissue phantoms visualized with acoustic resonance coupled with power Doppler US: initial observations " Radiology **224**(1): 265-269.

[36]. N. Chelfouh, N. Grenier, D. Higueret *et. al*. (1998). "Characterization of Urinary Calculi: In Vitro Study of "Twinkling Artifact" Revealed by Color-Flow Sonography." AJR 171: 1055-1060.

[37]. V. G. Lelyuk, S. E. Lelyuk, M. V. Karpochev, *et al*. (2003). "Doppler "twinkling"-artifact in experiments and practice." Echography **4**(1): 74-83.

[38]. L. Rubaltelli, Y. Khadivi., R. Stramare, *et al*. (2000). "Power Doppler signals produced by static structures: a frequent cause of interpreta-tion errors in the study of slow flows." Radiol. Med (Torino). **99**(3): 161-164.

[39]. A. Kamaya, T. Tuthill., J.M. Rubin (2003). "Twinkling artifact on color Doppler sonography: dependence on machine parameters and underlying cause " Am. J. Roentgenol **180**(1): 215-222.

[40]. L.S. Glowacki, M. L. Beecroft., R.J. Cook, *et al* (1992). "The natural history of asymptomatic urolothiasis." J of Urol **147**(2): 319-321.

[41]. J.D. Raman, M. S. Pearle. (2008). "Management for lower pole renal calculi." Current Opinion in Urology **18**(2): 214-219.

[42]. A. Shah, N. R. Owen, W. Lu, *et al* (2010). "Novel ultrasound method to reposition kidney stones." Urol Res **38**: 491-495.

[43]. R. N. Chen, S. B. Streem. (1996). "Extracorporeal shock wave lithotripsy for lower pole calculi: long-term radiographic and clinical outcome." J of Urol **156**: 1572-1575.

[44]. N. J. Parr, A. Ritchie, G. Smith, *et al* (1991). "Does further extracorporeal lithotripsy promote clearance of residual fragments?" J of Urol **68**: 565-567.

[45]. F. Krings, C. H. Tuerk., I. Steinkogler, *et al* (1992). "Extracorporeal shock wave lithotripsy retreatment ("stir-up") promotes discharge of persistent caliceal stone fragments after primary extracorporeal shock wave lithotripsy." J of Urol **148**: 1040-1042.

[46]. K. Hargreave, T. J. Matula., L.A. Crum *et al* (1998). "Noval techniques for manipulating single-bubble sonoluminescence." J. Acoust. Soc. Am **103**: 3048.

[47]. Y. Tian, R. G. Holt. And R. E. Apfel. (1993). "Deformation and location of an acoustically levitated liquid drop." J. Acoust. Soc. Am **93**: 3096.

[48]. J. Morgan, J. F. Spengler, L. Kuznetsova, *et al* (2004). "Manipulation of in vitro toxicant sensors in an ultrasounic standing wave." Toxicol in vitro **18**(1): 115-120.

[49]. K.R. Nightingale, G. E. Trahey. (2000). "A finite element model for simulating acoustic streaming in cystic breast lesions with experimental validation." <u>IEEE Trans Ultrason Ferroelectr Freq Control.</u> **47**(1): 201-214.

[50]. X. Shi, R. W. Martin, S. Vaezy, *et al* (2001). "Color Doppler detetion for acoustic streaming in a hematoma medel." <u>Ultrasound Med Biol</u> **27**(9): 1255-1264.

[51]. O. Levantal, S. Mary, D. Higueret, *et al.* (1997). "Color flow sonography of urolithiasis: in vitro study of the twinkling artifact " <u>ECR</u>: 108.

[52]. H. Trillaud, J. L. Pariente., A. Rabie, *et al* (2001). "Detection of encrusted indwelling ureteral stents using a twinkling artifact revealed on color Doppler sonography " <u>AJR</u> **176**(6): 1446-1448.

[53]. D. Maulik (2005). "Doppler ultrasound in obstetrics and gynecology." <u>Birkhäuser</u>: 70.

[54]. S. Bjarum and H. Trop (1997). "Optimal adaptive clutter filtering in color flow imaging." <u>S.C. Schneider M. Levy, B. R. McAvoy (eds) Proceedings of 1997 IEEE Ultrasounsonics Symposium, </u>: 1223-1226.

[55]. H. Trop, (1997). "Clutter rejection filters in color flow imaging: a treoretical approach." <u>IEEE Trans Ultrason Ferroelectr Freq Control.</u> **44**: 417-424.

[56]. K. Namekawa, C. Kasai, M, Tsukamoto, *et al* (1982). "Realtime bloodflow imaging system utilizing autocorrelation techniques." <u>R. A. Lerski, P. Morley (eds) Ultrasound `82 </u>203-208.

[57]. C. Kasai, K. Namekawa., A. Koyano, *et al* (1985). "Realtime two-dementional blood flow imaging using an autocorrelation technique." <u>IEEE Trans Sonics Ultrason SU.</u> **32**: 458-464.

[58]. K. S. Miller and M. M. Rochwarger (1972). "A covariance approach to spectral moment estimation." <u>IEEE Trans Inform Theory IT</u> **18**: 588-596.

[59]. A. Nowicki, J. Reid, P. C. Pedersen, *et al* (1990). "On the behavior of instantaneous freqeuncy extimator implemented on the Doppler flow imagers." <u>Ultrasound Med Biol</u> **16**: 511-518.

[60]. J. A. Jensen, (1996). "Estimation of blood velocities using ultrasound " <u>Cambridge University Press, Cambridge</u>.

[61]. J. C. Rajaonah, B. Dousse, J. J. Meister (1994). "Compensation of the bias caused by the wall filter on the mean Doppler frequency." <u>IEEE Trans Ultrason Ferroelectr Freq Control.</u> **41**: 812-819.

[62]. R. J. Collaris, A. P. G. Hoeks. (1994). "Postprecessing of velosity distributions in real-time ultrasonic color velocity imaging." <u>Ultrason Imaging</u> **16**: 249-264.

[63]. J. M. Rubin, R. O. Bude., P. L. Carson, *et al* (1994). "Power Doppler US: a potentially useful alternative to mean frequency-based color Doppler US." <u>Radiology</u> **190**: 853-856.

[64]. O. Bonnefous, P. Pesque., X. Bernard (1986). "A new velocity estimator for colour flow mapping." <u>Proceedings of the 1986 Ultrasonics symposium</u>: 855-860.

[65]. A. F. Prokop, S. Vaezy., M. L. Noble, *et al* (2003). "Polyacrylamide gel as an acoustic coupling medium for focused ultrasound therapy." <u>Ultrasound Med Biol</u> **29**(9): 1351-1358.

[66]. D. H. Evans, W. N. McDicken. (2000). "Doppler Ultrasound: Physics, instrumentation and signal processing (2nd edition)." <u>WILEY</u>: 229-260.

[67]. W. Lauterborn, T. Kurz. (2012). "Physics of bubble oscillations." Rep. Prog. Phys. 73: 88.

[68]. O. A. Sapozhnikov, V. A. Kholkhlova., M. R. Bailey, *et al* (2002). "Effect of overpressure and pulse repetition frequency on cavitation in shock wave lithotripsy." <u>J. Acoust. Soc. Am</u> **112**(1183-1195).

[69]. M. R. Bailey, L. N. Couret., O. A. Sapozhnikov, *et al*, (2000). "Use of overpressure to assess the role of bubbles in focused ultrasound lesion shape in vitro." <u>Ultrasound Med Biol</u> **27**: 696-708.

[70]. R. E. Apfel, (1970). "The role of impurities in cavitation-threshold determination." J. Acoust. Soc. Am 48: 1179-1186.

[71]. L. A. Crum (1982). "Nucleation and stabilization of microbubbles in liquids." Appl. Sci. Res. 38: 101-115.

[72]. I.Y Solodov, B. A. Korshak. (2001). "Instability, Chaos, and "Memory" in Acoustic-Wave-Crack interaction." Phy. Rev.Lett 88: 3.

[73]. A.Klepka, W. J. Staszewski., R.B. Jenal, *et al* (2012). "Nonlinear acoustics for fatigue crack detection - experimental investigations of vibro-acoustic wave Modulations." Structural Health Monitoring pp.11: 16.

[74]. PG. de Gennes, F. Brochard-Wyart, D. Quere (2002). "Capillary and Wetting Phenomena - Drops, Bubb,es, Pearls, Waves." Alex Reisinger. Springer.

[75]. M. Ashokkumar, M. Hodnett, B. Zeqiri, *et al* (2007). "Acoustic Emission Spectra from 515 kHz Cavitation in Aqueous Solutions Containing Surface-Active Solutes." J. Am. Chem. Soc. 129(8): 2250-2258.

[76]. A. E. Alegria, Y. Lion, T. Kondo, P. Riesz (1989). "Sonolysis of aqueous surfactant solutions: probing the interfacial region of cavitation bubbles by spin trapping." J. Phys. Chem 93(12): 4908-4913.

[77]. G. A. Gooding, D. Saloner., W. Eisert, *et al*, (1991). "Color Doppler artifact from metallic carotid clamp." J. Ultrasound Med **10**(12): 691-694.

[78]. K. Darge, (2005). "Be aware and beaware of the 'twinkling sign'" Pediatr Radiol **35**: 351-352.

[79]. O.A. Sapozhnikov, M. R. Bailey. (2012). "Radiation force of an arbitrary acoustic beam on an elastic sphere in a fluid." J. Acoust. Soc. Am (Submitted in May 2012.)

[80]. O. A. Sapozhnikov, L.A. Trusov, A. I. Gromov, *et al*. (2006) "Radiation force imparted on a kindey stone by a Doppler-mode diagnostic pulse", J. Acoust. Soc. Am.120(5), 3109

[81]. O.A. Sapozhnikov, N.R. Owen, M.R. Bailey, *et al.* (2007), "Use of scattering of ultrasound pulses and shock waves on kidney stones for imaging lithotripsy," Proceeding of the 14th international congress on sound and vibration (ICSV14, CAIRNS, AUSTRALIA, 2007), Bioacoutics. pp 1-8 (on CD).

[82]. A. P. G. Hoeks, J. J. W. Van der Vorst, A. Dabekaussen, *et al*, (1991). "An efficient algorithm to remove low frequency Doppler signals in digital Doppler system." Ultrason Imaging **13**: 135-144.

[83]. G. R. Torr, (1984). "The acoustic radiation force." J. Acoust. Soc. Am **52**(5): 402-408.

[84]. S. B. Streem, A. Yost, E. Mascha, (1996). "Clinical implications of clinically insignificant store fragments after extracorporeal shock wave lithotripsy." J Urol **155**: 1186-1190.

[85]. F.L. Levy, Adams.-Huet., CVC. Pak (1995). "Ambulatory evaluation of nephrolithiasis: An update of a 1980 protocal." Am J Med **98**: 51.

[86]. U.S. Food and Drug Administration, (2008). "Information for Manufacturers Seeking Marketing Clearance for Diagnostic Ultrasound Systems and Transducers."

[87]. H. T. O'Neil, (1949). "Theory of focusing radiators." <u>J. Acoust. Soc. Am</u> **21**: 516-526.

[88]. M. R. Bailey, V. A. Kokhlova, O. A. Sapozhnikov, *et al*, (2003). "Physical mechanisms of the therapeutic eVect of ultrasound (a review)." <u>Acoust Phys</u> **49**(4): 369-388.

[89]. A. P. Kadi, T. Loupas, (1995). "On the perfermance of regression and step-initialized IIR clutter filters for colour Doppler systems in diagnostic medical ultrasound " <u>IEEE Trans Ultrason Ferroelectr Freq Control.</u> **42**: 927-937.

[90]. R. Smith-Bindman, J. Lipson., R. Marcus, *et al* (2009). "Radiation dose associated with common computed tomography examinations and the associated lifetime attributable risk of cancer." <u>Arch Intern Med</u> **169**(22): 2078-2086.

[91]. R. Daigle (Apr. 2011) "Sequence Programming Manual." Verasonics. 51-52

[92]. http://mathworld.wolfram.com/HilbertTransform.html

[93]. J. A. Jensen (1993c). "Stationary echo canceling in velocity estimation by time-domain cross-correlation." <u>IEEE Trans Med Imaging</u> **12**: 471-477.

[94]. L. Thomas, A. Hall. (1994). "An improved wall filter for flow imaging of low velocity flow." <u>IEEE Ultrasonics Symposium</u>: 1701-1704.

[95]. A. Heimdal, H. Trop. (1997). "Ultrasound Doppler measurements of low velocity blood flow: limitations due to clutter signals from vibrating mauscles." <u>IEEE Trans Ultrason Ferroelectr Freq Control.</u> **44**: 873-881.

[96]. C. S. Williams, (1986). "Designing Digital Filters." <u>Prentice-Hall Englewood Cliffs, NJ</u>: 18-23.

[97]. M. A. Shariari, J. H. Dripps, W. N. McDicken (1993). "Deadbeat IIR based MTI filtering for color flow imaging systems." <u>Proceedings of the 1993 IEEE Ultrasonics Symposium</u> **2**: 1059-1063.

[98]. R. B. Peterson, (1993). "A comparison of IIR initialization techniques for improved color Doppler wall filter performance." <u>MSEE Dissertation </u>university of washington.

[99]. http://mathworld.wolfram.com/LeastSquaresFittingPolynomial.html

[100]. I. Y.Solodov (1998), "Ultrasonics of non-linear contacts: propagation, reflection and NDE-applications." Ultrasonics, 36: 383-390

Appendix A

Radio-Frequency (RF) Data Acquisition

The experimental setup for data acquisition is shown in figure A.1. A human kidney stone was fixed in the acrylamide gel phantom (or porcine kidney phantom). The transducer (ATL, L7-4) was fixed by ring clamp on top of the phantom. The transducer and phantom were coupled by degassed water. A rubber absorber was put at the bottom of the phantom container to reduce the reflection from the bottom. The transducer connected directly to the VUE. Unbeamformed RF data of Doppler ensembles can be obtained from corresponding Matlab datasets - RcvData. The structure of saving stack is [M * N * F], where M is the sample points for each scan line; N is the number of channels and F is the number of frames. The RF data per scan line per frame is shown in figure A.2. There are two parts within the RF data set. The first part, which is cycled with yellow box, is the RF data of B-mode imaging while the second part, cycled by red square, is the RF data of Doppler ensemble. We can see there are multiple pulses within the Doppler ensemble. The default setting of the VUE is 14 Doppler pulses within each Doppler ensemble.
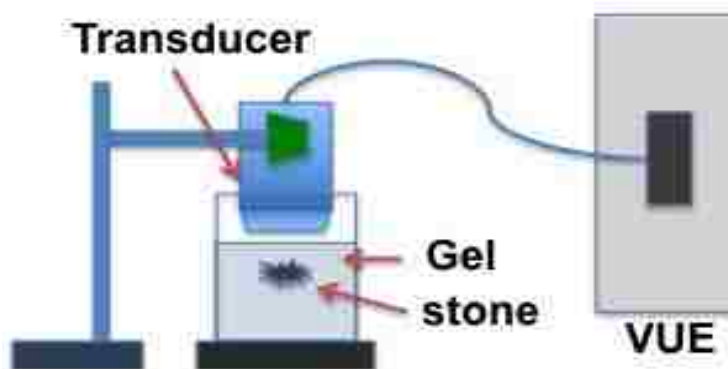
The VUE uses 64 channels for Doppler signals transmission and 64 channels for Doppler signals receiving. For the receiving channels, signals received by channels 1 to 32 are saved in 33 to 64 columns in the save stack while signals received by channels 33 to 64 are saved in 1:32 columns in the save stack. A switch to put the data into the right order needs to be done before the RF data analysis. There is a matrix called 'Receive' that provided by the VUE, which recorded the start and the end of each receiving pulse within the Doppler ensemble.
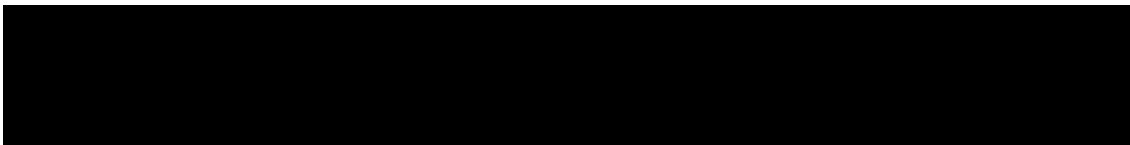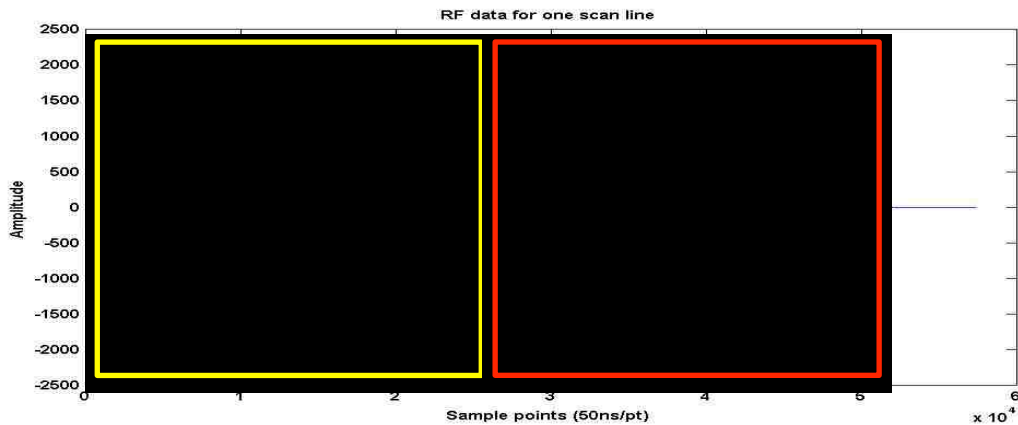
The transducer used in all experiment is the ATL linear probe L7-4 because he linear probe is simple to work with and the easiest one to use to develop our own data processing algorithms. The center frequency of the transducer is 5 MHz. The sampling frequency is 20 MHz for sampling the received data (4 sample points per wavelength). The incident angle of Doppler pulses is zero degrees and the pulse repetition frequency (PRF) is 3 KHz. For all experiments, the time-gain-compensation (TGC) is set to the minimum level we can reach (it says the minimum level is zero in the manual [91]). The goal of turning down the TGC is to

avoid signal saturation in order to separate the effect of the TGC. The Doppler threshold is set to the level that background noise is just eliminated. The color-written priority is set to the highest level we can reach since we do not want to miss any TA on the image.

Since the memory stack VUE provides for unbeamformed RF data, such as the unbeamformed Doppler pulse within the Doppler ensemble, it is 12 bits. Which means that the maximum amplitude for the signal is ± 2048. There is also a clipping circuit that is used to limit the maximum input of the Analog/Digital converter (ADC) prior to the anti-aliasing filter of the ADC. There are four setting levels of clipping. We did the calibration for the default setting level '1'. If the signal is saturated, the amplitude of the clipped signal should be close to 2000. Otherwise, we treat it as no signal saturation in the channel. For the hardware ahead of the ADC, there is the transducer and the FPGA (Field-programmable gate arrays). For the transducer itself, we assume that it does not affect the Doppler ensembles; for the FPGA, it is a logic programmable chip that supports thousands of gates. We don't think it can affect the Doppler ensemble either.

Appendix B

The Signal Path of the Color Doppler Ultrasound Imaging

a) The grey-scale image display

Since the object we want to image is different from the common needs of the grey-scale ultrasound image, a new compression algorithm is needed. For kidney stone detection, the location and the size of the stone is important, which determined that instead of carrying the details only, the new algorithm should also function towards separating strong echoes. However, the B-mode imaging improvement for stone detection is not our priority. We did not make much effort on this part.

b) Beam-former and quadrature

The beam-former part for the linear transducer is described in Appendix C. Based on our experience, there is no extra phase or amplitude effect introduced within the processing.

The method VUE used for RF data quadrature demodulation is as follows: the sample rate is reduced by the front end processing from 4 samples per wavelength to one non-aligned quadrature pair per wavelength. (This is equivalent to throwing away every 3rd and 4th sample from the 4 samples per wavelength). The machine does the quadrature and decimation together. The main reason for the VUE to use this quadrature demodulation is the computing load, which is not our concern so far. The beam-former and quadrature processes have limited effects on the TA.

c) Wall-filter

The wall-filter used by VUE is a 2nd order (quadratic basis) regression filter, because the regression filter works the best for short ensemble lengths (under 16 pulses within the ensemble). The basic idea of the regression filter is that the low-frequency (typically, lower than 1 kHz) clutter signal within the Doppler

ensemble could be approximated by a low order polynomial. The low-order polynomial can be estimated by employing least-squares regression analysis [66].

d) Autocorrelation Algorithm

Once the Doppler signal is filtered to reject the low-frequency components due to the tissue motion, it is sent to a velocity estimator where the mean frequency, Doppler power, velocity, Doppler bandwidth are calculated. Currently, the most popular method for velocity and Doppler power estimation is the autocorrelation algorithm [57-58, 66]. So, the estimation of the averaged Doppler power, velocity and frequency shift has been done with this algorithm. The mean angular frequency, $\bar{\omega}$, of the Doppler power spectrum, $P(\omega)$, can be defined as:

$$\bar{\omega} = \frac{\int_{-\infty}^{\infty} \omega P(\omega) d\omega}{\int_{-\infty}^{\infty} P(\omega) d\omega} \tag{B.1}$$

The autocorrelation function $R(\tau)$ is related to the Doppler power spectrum $p(\omega)$ by the Wiener-Khinchin theorem:

$$R(\tau) = \int_{-\infty}^{\infty} P(\omega) e^{i\omega\tau} d\omega. \tag{B.2}$$

The first derivative of $R(\tau)$ with respect to τ is:

$$\dot{R}(\tau) = j \int_{-\infty}^{\infty} \omega P(\omega) e^{i\omega\tau} d\omega \tag{B.3}$$

Combining the equation (B.1), (B.2) and (B.3), the mean angular frequency, $\bar{\omega}$, can be written as:

$$\bar{\omega} = -j \frac{\dot{R}(0)}{R(0)} \tag{B.4}$$

where $\dot{R}(0)$ is the first derivative of the autocorrelation function for zero lag and $R(0)$ is the autocorrelation function for zero lag.

So, the average power of signal, $\bar{P}$, can be derived from equation (B.4) for zero lag:

$$\bar{P} = R(0) \tag{B.5}$$

Assuming the autocorrelation function is [57]:

$$R(\tau) = A(\tau) e^{j\varphi(\tau)} \tag{B.6}$$

where $A(\tau)$ is the real even function and $\varphi(\tau)$ is the real odd function of τ, the mean angular frequency, $\bar{\omega}$, can be written as:

$$\bar{\omega} = \dot{\varphi}(0) \approx \frac{\varphi(T)}{T} = \frac{1}{T}\arg R(T) \qquad (B.7)$$

where T is the time between Doppler pulses.

Miller *et al.* [56] estimated the expression of $R(T)$ and $R(0)$ in 1972. If the complex process Z is given by:

$$Z(i) = I(i) + jQ(i) \qquad (B.8)$$

where I and Q are the in-phase and quadrature of magnitudes of the Doppler signal, the mean angular frequency, $\bar{\omega}$, and the average power of signal, $\bar{P}$, can be written in the following ways [66]:

$$\bar{\omega} = \frac{1}{T}tan^{-1}\left\{\frac{\sum_{i=1}^{N}Q(i)I(i-1)-I(i)Q(i-1)}{\sum_{i=1}^{N}I(i)I(i-1)+Q(i)Q(i-1)}\right\} \qquad (B.9)$$

$$\bar{P} = \frac{1}{N}\sum_{i=1}^{N}I^2(i) + Q^2(i) \qquad (B.10)$$

where N equals the number of Doppler pulses within the Doppler ensemble minus 1. The estimation from autocorrelation is ideally unbiased [57-60].

e) Thresholds and color priority encoding

In the velocity estimator, the average Doppler power, velocity and frequency shift are estimated. However, among those estimations, some of them correspond to the presence of blood flow and some of them are related to artifacts. The thresholds that determine the possibility of displaying grey-scale information for the tissue and color information for the presence of blood flow are very important. If we want to make stone-specializing image methods, the modification of thresholds is critical. As usual, the thresholds are different from machine to machine, but there are some themes in common.

i) The Doppler signal magnitude threshold.

In the setting, if the estimated average Doppler signal power is less than the threshold level, the machine will not display color information on the image.

ii) Velocity threshold

If the velocity calculated from autocorrelation is too slow, the Doppler spectrum is more likely to be dominated by clutter signals leaked through the wall-filter rather than blood flow signals. If the calculated velocity is lower than a certain velocity threshold, gray-scale information will be displayed on the screen.

iii) Echo intensity threshold (brightness threshold)

If the amplitude of the gray-scale echoes (B-mode signals) is very strong, the possibility of this signal being related to clutter is much bigger than that related to blood flow. The grey-scale information will be encoded on that sample volume.

vi) The Doppler bandwidth threshold

The basic idea of this threshold is that the bandwidth of the Doppler signal from blood flow should be relatively narrow while the bandwidth of the background noise will be very broad. If the estimated variance of the Doppler power spectrum exceeds a certain value, the velocity signal is assumed to be invalid.

Appendix C

Homemade Doppler Processing Algorithms

In appendix B, we briefly introduced our homemade color Doppler processing algorithm from beamforming to the image display. It is used to substitute the color Doppler processing algorithm for the purpose to study the mechanism and signal properties of the TA. For the modified stone-specialized imaging technique, it is reported in detail in chapter 3.
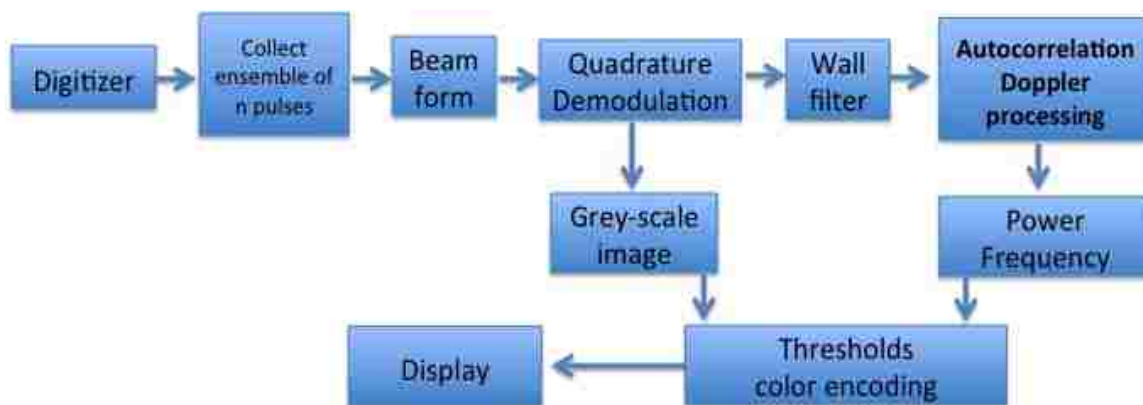

Figure C.1 shows the general layout of the color Doppler processing algorithm we developed. Briefly, the RF data are collected from the digitizer. They get beamformed in the beam-former and then they are quadrature demodulated by using Hilbert transform; the I- in-phase and Q - quadrature data are obtained. The IQ data are filtered by a wall-filter for the rejection of clutter components. The Doppler power, mean frequency, and velocity then are acquired using autocorrelation. The grey information that was calculated by using unbeamformed RF data and the color information are combined to build the Doppler image. Color or grey information is chosen for each pixel according to the thresholds and color encoding.

There are five main components in our Doppler processing algorithm. 1)

beamforming; 2) quadrature; 3) wall-filter; 4) autocorrelation and the processing of Doppler power, velocity, and mean frequency; 5) threshold setting and color written priority; and 6) image display. I will describe what we did on each step.

1) Beamforming:

The critical point of the beamforming is to calculate the time delay for each channel (element). Figure C.2 shows received echoes from an object.


Receive echoes from objects
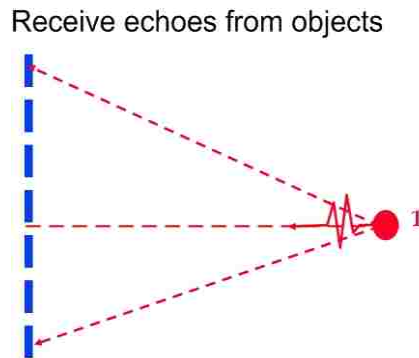
Fig. C.2. Received echoes from object

Figure C.2 shows that the reflected echoes will arrive at the surface of the element at different times. The echo in the middle traveled faster than echoes from the side (assume there is homogenous medium around). Figure C.3 gives more insight into the time delay which happened between channels. If we want to rebuild the image, we need to compensate the time delay in the first place (like shown in figure C.4) and then, those post-beamforming signals will be summed for rebuilding the image.
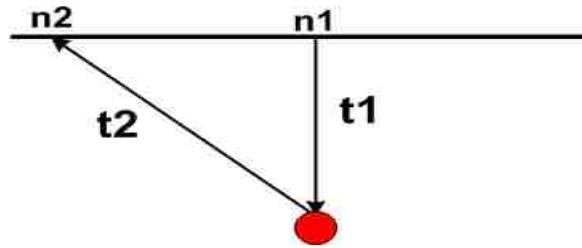

elements

elements
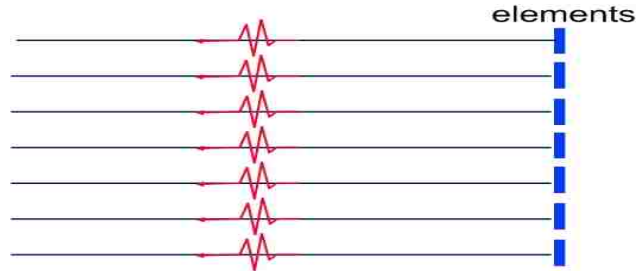
Fig. C.4. Time delay compensation

The time compensation is calculated in the following way. A flash plane wave is sent from the transducer. As shown in figure C.5, we assume it costs time t1 for the pulse sent from channel n1 to hit the object and it will cost the same time for the echo to go back to the surface of the element of channel n1. In the meantime, the scattered echo will be received by other channels too. We assume it will cost echo time t2 to arrive at the surface of the element of channel n2. We can calculate the time delay by calculating the difference between t1 and t2. t2 can be calculated by applying equation (C.1).

Fig. C.5. Time delay compensation calculation

$$t_2 = \sqrt{\left[(n_2 - n_1)d\right]^2 + (ct_1)^2} \, / \, c \qquad (C.1)$$

Where n1 and n2 are the number of the channels; d is the element spacing; and c is the velocity of sound in tissue.

Based on the calculation of time delay, we can track which data in channel RF data should contribute to certain pixels by using equation (C.2).

$$N = 8(t_1 + t_2)c \, / \, wvl \qquad (C.2)$$

Where wvl is the wavelength of the sending pulse and N is the sequence number of the sample points. Right now, we use a sample frequency that is 4 sample points per wavelength for sampling, which is why we multiply by 8 here (signal forward and backward). Sometimes, the calculated N is not an integer, we apply linear interpolation for adjacent sample points to get the value. When we use the L7-4 transducer with a sampling frequency at 4 sample points per wavelength, the time difference between sample points is 50 ns.

After obtaining the time delay for each channel, the signals with the time delay compensation are summed together. During the procedure, all pixels are weighted 1, equally, and the sensitivity (how many channels used in the beamforming for a certain pixel) is set to 1, which means that data from all channels are taken into account.

In our beamforming algorithm, there is one problem that occurs when reaching the end of the imaging depth, there will be not enough data to choose for beamforing. It means that when the pixel that is going to get beamformed is close enough to the end of image, t2 + t1 could be bigger than the image depth. In this case, the beamformed data will not be accurate. However, during our processing, it is not a big issue since our objects are usually in the middle of the image.

2) Quadrature:

A quadrature signal is a two-dimensional signal that contains two main parts: the real part and the imaginary part, or the in-phase part and quadrature phase part. It is necessary to describe the processing and implementation that happens in a digital communication system.

For the quadrature demodulation, I applied the Hilbert transform. The reason for applying the Hilbert transform is because it is a precise transform method, and at the same time, the computer load is not the main concern in our cases. The Hilbert transform $\hat{f}(t)$ of a function f(t) is defined for all t by equation (C.3) [92]:

$$\hat{f}(t) = \frac{1}{\pi} P \int_{-\infty}^{\infty} \frac{f(\tau)}{t-\tau} d\tau \qquad (C.3)$$

The Hilbert transform returns the analytical signal from a real data sequence. The imaginary part is the 90° phase shift of the original real sequence. The Hilbert transformed sequence has the same amplitude and frequency as the original real data sequence.

After the quadrature demodulation, the complex data sequence that contains I, in-phase and Q, quadrature data will be obtained. This data set is the IQ data.

3) Wall-filter

The purpose of the wall-filter or clutter filter is to block the high-amplitude but low-frequency signal echoes from stationary or near-stationary targets [66]. Typically, the clutter signal is with a frequency lower than 1 kHz and the amplitude 40-60 dB higher than the scattered signal from blood flow [93-95]. There are many kinds of wall-filters that have been reported, such as finite impulse response filters (echo cancellers) [96], infinite impulse response filters [97-98], regression filters [82,89] and so on. The FIR filter is basically an echo canceller filter with a wide transition bandwidth. The reason why FIR is not applied in the Doppler processing is that the wide bandwidth of the transition will exclude the low frequency of blood flow. For the IIR filter, it performs better than the FIR filter in Doppler processing. However, the drawback of using IIR is that it needs a good initialization. In Doppler processing, it is unlikely to get a good initialization for every measurement. We apply the regression filter in our algorithm since the limited sample points we have and the regression filter does not reduce the number of output sample points for further frequency estimation [66].

The basic idea of regression filter is that the low-frequency clutter signal within the Doppler ensemble could be approximated by a low order polynomial. The low-order polynomial can be estimated by employing a least-squares regression analysis [66]. The algorithm [99] we used for the least-square regression is shown below, briefly:

The kth degree polynomial:

$$y = a_0 + a_1 x + \cdots + a_k x^k \tag{C.4}$$

The residual is given by:

$$R^2 = \sum_{i=1}^{n}[y_i - (a_0 + a_1 x + \cdots + a_k x^k)]^2 \tag{C.5}$$

The matrix for a least squares fit:

$$\begin{bmatrix} 1 & x_1 & \cdots & x_1^k \\ 1 & x_2 & \cdots & x_2^k \\ \vdots & \vdots & \ddots & \vdots \\ 1 & x_n & \cdots & x_n^k \end{bmatrix}\begin{bmatrix} a_0 \\ a_1 \\ \vdots \\ a_k \end{bmatrix} = \begin{bmatrix} y_1 \\ y_2 \\ \vdots \\ y_n \end{bmatrix} \tag{C.6}$$

Equation (6) can be written as:

$$y = Xa \tag{C.7}$$

Multiplying matrix transpose X^T on both sides of equation (A3.7):

$$X^T y = X^T X a \tag{C.8}$$

If the matrix is well formed, the solution vector can be derived:

$$a = (X^T X)^{-1}(X^T y) \tag{C.9}$$

Then, we can use equation 9 to estimate the vectors and then derive the residuals. The residuals are the wall-filtered signal.

4) Autocorrelation

After being filtered, the components with low frequency and high-pressure got us a wall-filtered signal, or Doppler residuals. The Doppler residuals are sent for Doppler processing meaning that the mean frequency, Doppler power, and velocity will be calculated. Currently, the most widely used algorithm for Doppler processing is the autocorrelation algorithm [57].

The autocorrelation function $R(\tau)$ is related to the Doppler power spectrum $p(\omega)$ by the Eiener-Khinchin theorem: $R(\tau) = \int_{-\infty}^{\infty} P(\omega)e^{i\omega\tau}d\omega$. The average power of the signal, $\bar{W}$ can be calculated by the autocorrelation at the time delay $\tau = 0$:

$$\bar{W} = R(0) \tag{C.10}$$

The mean angular frequency $\bar{\omega}$ can be calculated from the autocorrelation at the time delay T:

$$\bar{\omega} = \frac{1}{T} arg\, R(T) \qquad\qquad\qquad\qquad \text{(C.11)}$$

where T is the time between subsequence Doppler pulses.

In our algorithm, the same autocorrelation is used as discussed above. The signal Z can be represented as $Z = I + iQ$, where the I and Q are the quadrature demodulated IQ data.

Assume there are pl pulses within each Doppler ensemble. The autocorrelation for 0 delay and T delay are:

$$R(0) = \sum_{i=1}^{pl} Z(i)Z^*(i) \qquad\qquad\qquad \text{(C.12)}$$

$$R(T) = \sum_{i=1}^{pl-1} Z(i-1)Z^*(i) \qquad\qquad \text{(C.13)}$$

R(0) is the averaged Doppler power.

The mean frequency can be calculated by using equation (C.11) and the velocity can be derived as following:

$$\bar{v} = \frac{\bar{\omega}}{\omega_0} \frac{c}{2cos\theta} \qquad\qquad\qquad\qquad \text{(C.14)}$$

Where $\bar{\omega}$ is the mean angular frequency; ω_0 is the angular frequency of carrier signal; c is the velocity of sound; and θ is the angle between the sound beam and the blood flow vector.

5) Threshold settings and color encoding priority

For normal color Doppler processing, there are four thresholds used in the algorithm: the Doppler power threshold, velocity threshold, brightness threshold, and Doppler bandwidth threshold. Based on the suitable adjustment of these four thresholds, the TA can be shown with better contrast. These thresholds do not determine the origin of the TA; they just determine whether or not we can see it on the display. The stone-specialized thresholds designs are discussed in chapter 3.

6) Image display

The B-mode image is rebuilt from the log compression of the amplitude of the unfiltered Doppler signal and displayed with a grey-scale color map. Whether the screen displays grey information or color information will be decided by the settings of thresholds and color written priority. In our algorithms, the B-mode grey-scale image was constructed by using the Doppler pulses. The only difference between the Doppler pulse and the B-mode pulse used in the VUE is the pulse length. It is a 3-cycle pulse used for Doppler and a 1-cycle pulse used for B-mode. When we obtained the B-mode image, the intensity of each pixel on the image was log-compressed and scaled for 1-127; the color map for the color pixels can be set in a similar way but scaled to 128-255. Then two color maps were combined. The color map used in the image display is shown in figure C.6.
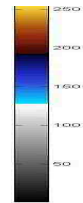
Signal Saturation Estimation:
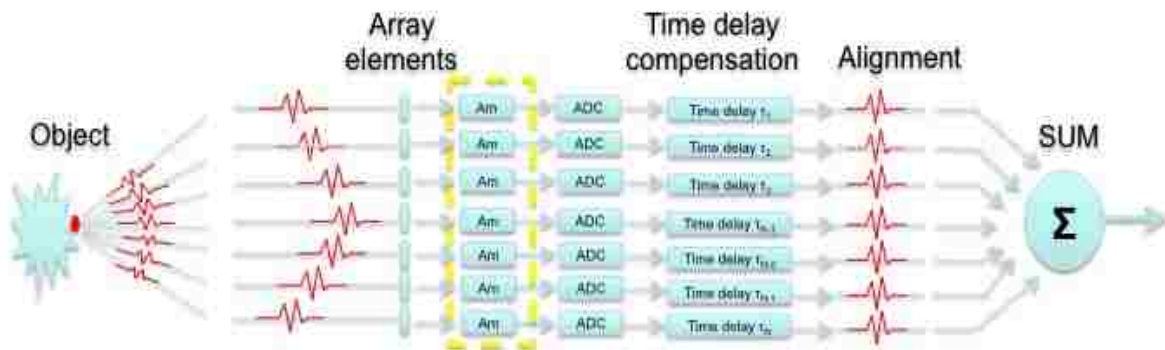
The difference from figure C.7 to figure 2.8 is that the location of the amplifiers and the analog-to-digital converters (ADC) that are shown in the signal path. The saturation concern happens on the ADC part. There are two possibilities why the signal saturation happens. On one hand, the signal itself is so strong that the

input voltage is equal or greater than the supply voltage (15 V for the TGC using in the VUE) where the output voltage of the amplifier will not be under control by the manufacturing process; on the other hand, the signals are too strong to saturate the 12-bit ADC.

The hypotheses were tested as follows. For the TGC circuit saturation, the break-board which allows us to separate input channels was employed. The sinuous wave was sent into the VUE by using the function generator (AFG 3022B, Tektronix, OR). The amplitude of the sending signal can be adjusted on the function generator. The TGC was set to the minimal level; the amplitude of the per-channel RF data was monitored on the screen. Since the ADC is a 12-bit device, the maximum positive amplitude of the receiving signal is 2048. The relationship between the voltages applied on the sending signals and the amplitude of the receiving signals were established. The result shows that when the receiving signal reaches the limits (~ 2048) the voltage applied on the sending signals was ~1.2 – 1.5 V, which is much smaller than the supply voltage of the TGC (15 V). This results suggest that there should be no signal saturation happening if the amplitude of receiving signals were within the limits.

If the signal saturation on the ADC part affects the TA, we should observe that there is at least the amplitude of the aligned channel data that hit the ceiling of the amplitude limitation when there is the TA. This was tested in the twinkling and strong reflection section. In figure 2.10, the amplitude of the aligned channel data was all far below the amplitude limitation. This result suggests that there is no signal saturation happening when there was the TA.

So, the signal saturation is not the critical reason for the origin of the TA.

Appendix D

Backscattering of a Pulsed Plane Wave from an Elastic Sphere
Many thanks to Dr. Oleg A. Sapozhnikov for creating this modeling tool for my study.

Consider an elastic sphere of radius a with its center having a coordinate z=d. A plane wave propagating along the z-axis is scattered at this sphere.
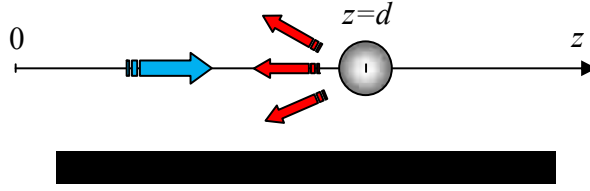
The incident wave at the origin z=0 has the waveform $p_0(t)$. The scattered wave at the same point z=0 (i.e. the backscattered signal) has some waveform $p(t)$. Because the scattering is a linear process, the backscattered signal can be written as a convolution integral:

$$p(t) = \int_0^\infty H(t')p_0(t - t')dt' \qquad \text{(D.1)}$$

Where the H(t) describes the scattered signal when the incident pulse $p_0(t)$ is very short that can be described by the delta-function $\delta(t)$. Note that according to causality H(t) = 0 before the first reflection comes back, i.e.

$$H(t) = 0 \; for \; t < \frac{2(d-a)}{c} \qquad \text{(D.2)}$$

Where d is the distance from the origin to the sphere center, a is the sphere radius, and c is speed of sound. And H(t) can be found is numerically for specific parameters of the elastic sphere and for the specific distance to the sphere.

Consider a sinusoidal incident wave $p_0(t) = S_0(\omega)e^{-i\omega t}$. For such a wave Eq. (D.1) gives a scattered signal $p(t) = S(\omega)e^{-i\omega t}$ with the following amplitude:

$$S(\omega) = S_0(\omega) \int_0^\infty H(t')e^{i\omega t'}dt' = S_0(\omega) \int_{-\infty}^\infty H(t')e^{i\omega t'}dt' \qquad \text{(D.3)}$$

Here the low limit was changed from 0 to $-\infty$ because of Eq. D.2. Therefore, the impulse response H(t) is related by a Fourier transform with the sinusoidal wave reflection coefficient:

$$S(\omega) = R(\omega)S_0(\omega) \qquad\qquad\qquad (D.4)$$

$$R(\omega) = \int_{-\infty}^{\infty} H(t)e^{i\omega t}dt \qquad\qquad\qquad (D.5)$$

Eq. D.5 can be inverted:

$$H(t) = \frac{1}{2\pi}\int_{-\infty}^{\infty} R(\omega)e^{-i\omega t}d\omega \qquad\qquad\qquad (D.6)$$

Therefore, the problem of finding H(t) is reduced to the problem of finding $R(\omega) = S(\omega)/S_0(\omega)$. Far from the stone the corresponding solution can be written analytically. If a plane wave $p_i = Ae^{-i(\omega t - kz)}$ is incident to the sphere, then the scattered wave is:

$$p_s = A\sum_{n=0}^{\infty} C_n \times i^n(2n+1)P_n(cos\theta)h_n^{(1)}(kr) \qquad\qquad (D.7)$$

Here, $k = \omega/c$ is the wavenumber, θ is the spherical angle (i.e. angle between the scattering direction and z-axis), $P_n(...)$ are Legendre polynomials, $h_n^{(1)}(...)$ are spherical Hankel functions. The constants C_n depend on the elastic parameters of the sphere material and those of liquid, on sphere radius, and on wave frequency. The constants C_n have fairly cumbersome expressions (that use Bessel functions and their derivatives).

Backscattered signal corresponds to $\theta = \pi$, which gives $P_n(cos\theta) = (-1)^n$. Also, far from the scatterer in the far field, the Hankel functions by their asymptotes: $h_n^{(1)}(kr) \to (-i)^{n+1}\frac{e^{ikr}}{kr}$. As a result we obtain the backscattering factor:

$$R(\omega) = \frac{e^{-2ikd}}{ikd}\sum_{n=0}^{\infty} C_n(-1)^n(2n+1) \qquad\qquad (D.8)$$

Here ω and $C_n=C_n(\omega)$ are known functions of frequency ω.

In numerical modeling the functions (e.g. the waveform and spectrum) are discretized. So, the impulse response is in fact periodized with some period T. This period should be big enough, so than "ringing" in the sphere by the end of the cycle is over (or almost over). For instance, 1ms or higher.

The following parameters were taken in the modeling:

a =2 mm (radius of the elastic sphere)

d =30 mm (distance from the probe to the sphere center)

h_t =50 ns (time-step for the impulse response sampling)

T =3.27675 ms (time window to define the impulse response, with such a window number of sampling points is T/ h_t =65536=2^{16})
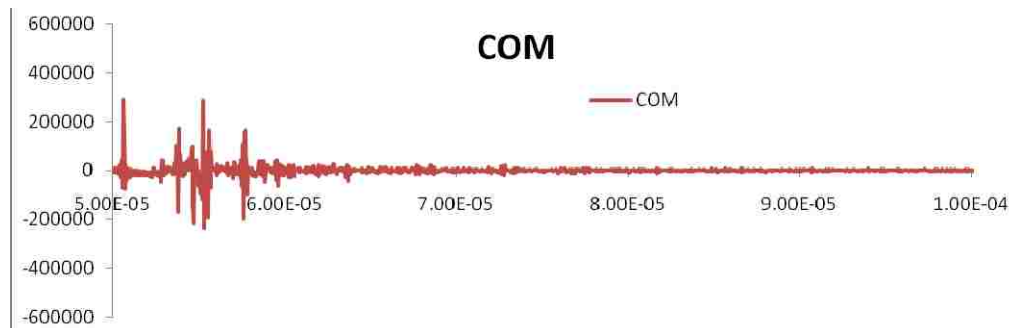
ρ_{water}=1000 kg/m^3 (density of water)

c_{water} =1500 m/s (sound velocity of water)

ρ_{COM} = 2038 kg/m^3 (density of COM stone)

c_l = 4535 m/s (longitudinal velocity)

c_t = 2132 m/s (shear velocity)

d_{pitch}=0.3 mm (the distance within two elements next to each other)

As shown in figure D.2, the first reflection comes at t= 50.67 us, as it should be for the travelled distance 76 mm (from the source to the sphere nearest edge and back). The responses within the time window 50 us < t < 100 us are shown. It is seen that for kidney stones the second reflection is even higher than the first one. This is due to shear waves.

The procedure to do the modeling related to the twinkling artifact by using the impulse response is as follows:

1) Take the imaging pulse waveform (from the thick glass plate, 20MHz in sampling frequency). The result is called u_m, m = 0,1,…, M-1;

2) The ensemble contains more than 1 pulse, say K pulses. The period between pulses within the Doppler ensemble is T. The amount of sample points can be calculated by M_T = T/h, where h is the sample step that is 50ns in all cases. T can be calculated by 1/PRF. Since we cut the first reflection portion from the original reflection pulses captured by VUE, the rest of the incident pulses were filled with noise intercepted from the original signals (I will explain why I did this rather than filling the rest of the signal with 0).

3) Building the ensemble of K pulses by periodic continuation of u_m;

$$Un = \begin{cases} u_n, n = 0,1,2, \dots, M_T - 1 \\ u_{n-M_T}, n = M_T, M_T + 1, M_T + 2, \dots, 2M_T - 1 \\ \dots \\ u_{n-(K-1)M_T}, n = (K-1)M_T, (K-1)M_T + 1, (K-1)M_T + 2, \dots, KM_T - 1 \end{cases}$$

As the results, we had a digitized ensemble U_n for n = 0,1,…,N-1, where N = KM_T.

4) Estimating the scattered ensemble by calculating the convolution of the impulse response (H_l, l = 0,1, …, L=2^{16} = 65536) and incident pulses:

$$P_n = \sum_{l=0}^{\min (L,n)} H_1 U_{n-l} \qquad\qquad (D.9)$$

5) The scattered ensemble (scattered results) was sent for Doppler processing. The regression filter with the second order is applied. The first two pulses are withdrawn for the Doppler power calculation.

Appendix E

Pressure Field Measurement for the L7-4 Transducer

For the measurement procedure, the transducer was fixed on the top of the water tank and the surface of the transducer was perpendicular to the bottom of the tank. A lipstick hydrophone (HGL0085, ONDA, US. sensitivity: 48.4306 nv/pa for 5 MHz) was fixed on the positioning system. The head of the hydrophone faced up and was aligned with the transducer. The water was degassed and the oxygen content was lower than 20%. The VUE was run in the color Doppler imaging mode that is the same as what we used in the experiments. The pulse incident angle was 0 degrees. For each power level, the hydrophone moved from 2 cm to 6 cm to capture waveforms for each distance. Six power levels, 1.6 V (min), 10 V, 20 V, 30 V, 35 V, 36 V (max) were involved in the measurements. Figure E.1A shows the plots for peak positive pressure and figure E.1B shows the peak negative pressure (lower) for different distances from the transducer surface under a variety of transmitting power levels.

In figure E1, the maximum peak positive pressure at 3 cm away from the transducer and the maximum peak negative pressure at 2 cm away from the transducer is shown. The peak positive pressure decreases as the distance increases further than 3 cm. The absolute value of the peak negative pressure decreases with increases in the distance. For most of our experiments, the stones were placed at a location that was 3 cm away from the transducer. Figure E.2 show the peak positive/negative pressure at 3 cm away from the transducer under different transmitting power levels, respectively.

In figure E.2, both the peak positive and peak negative pressures change linearly with increases in the transmitting power. The higher the transmitting power the higher the peak positive/negative pressure in the field. The maximum peak positive pressure is 4.35 MPa and the maximum peak negative pressure is -2.22 MPa at 3 cm.
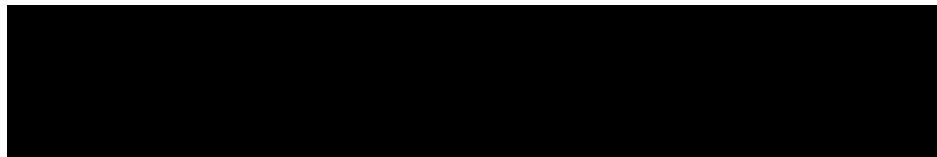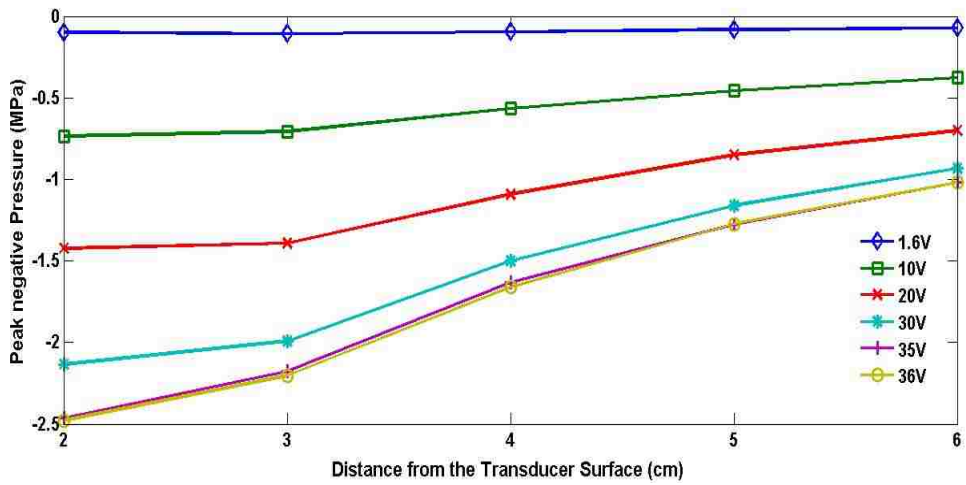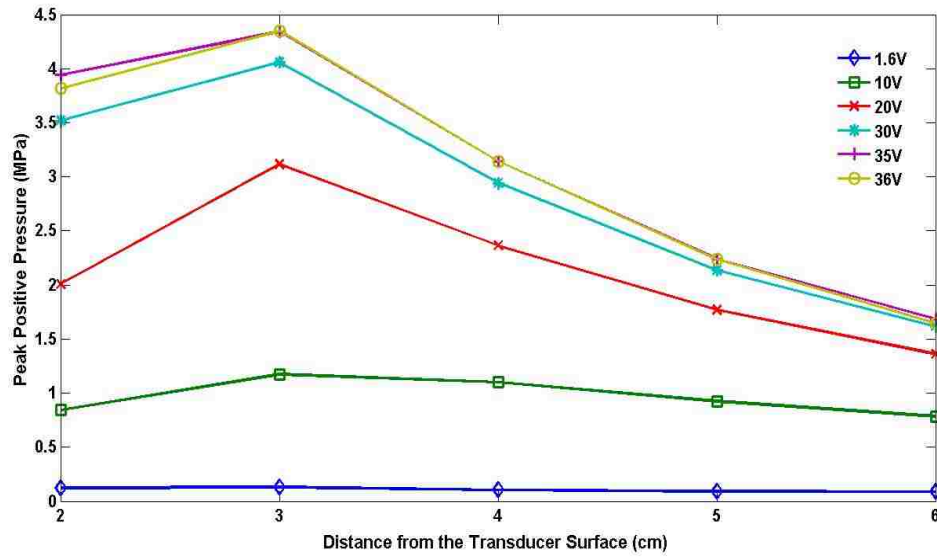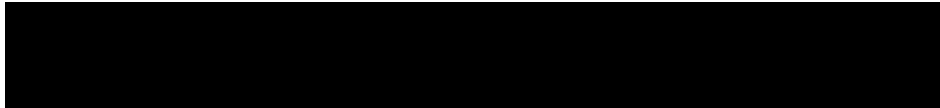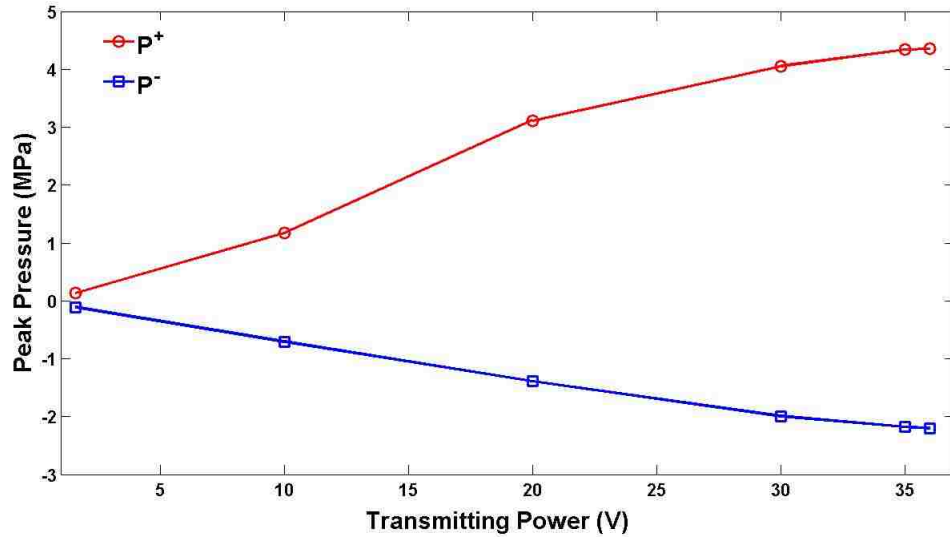
VITA

Wei was born on September 30th, 1981 in Tianjin, P. R. China. He graduated from the 1st High School of Bohai Shiyou in 2000. In 2004, Wei graduated from Huazhong University of Science & Technology, Wuhan, Hubei Province, P. R. China with a BS in Opto-electronics Engineering. In 2007, Wei earned a MS in the Department of Biomedical Engineering from the same university for a thesis project titled, *Effect of light losses of sample between two integrating spheres on optical properties estimation*. In Autumn 2007, he began his PhD studies in the Department of Bioengineering at the University of Washington and joined Drs. Crum and Bailey's lab, the Center for Industrial and Medical Ultrasound, to study diagnostic and therapeutic ultrasound. Wei graduated with a Ph.D. in bioengineering in Summer 2012.